Dual-path receiver for state reconstruction of propagating quantum microwaves

Diploma Thesis

Peter Eder

January 2012

Supervisor: Prof. Dr. Rudolf Gross

Advisor: Edwin P. Menzel

TECHNISCHE UNIVERSITÄT MÜNCHEN

This work is dedicated to my father, my grandfathers, my great-grandmother and all friends who are watching from above.

Erklärung / Declaration of Originality

Mit der Abgabe der Diplomarbeit versichere ich, dass ich die Arbeit selbständig verfasst und keine anderen als die angegebenen Quellen und Hilfsmittel benutzt habe.

By submission of this thesis I hereby certify, that this diploma thesis is my own work and no sources other than the ones given have been used.

Garching, 18. Jänner 2012	
Ort, Datum	Peter Eder

Contents

Chapter 1

Introduction

Quantum state reconstruction is a central problem in optical cavity quantum electrodynamics (cQED) [1–9] and its condensed matter analogon circuit quantum electrodynamics (circuit QED) [10–16]. Both fields explore the foundations of light-matter interaction down to the limit of single atoms (in circuit QED represented by Josephson junction based superconducting circuits) and photons. Having extraordinarily high interaction strengths [10, 17, 18], circuit QED setups allow for the straightforward generation of quantum states such as, for example, Fock [19] or squeezed states [20–22]. Due to the specific properties of superconducting circuits [11, 23], these states are in the microwave regime with typical frequencies of a few gigahertz. Following groundbreaking work on the tomography of bound intra-cavity quantum microwaves [24], various methods were proposed. In 2010 Menzel *et al.* [25] introduced the dual-path method for the state reconstruction of *propagating* quantum microwaves. Meanwhile also other approaches are being explored [21, 22, 26]. Since propagating quantum microwaves in circuit QED systems are the analog to optical light waves traveling in fibers, it seems natural to adapt a standard tomography technique such as optical homodyning to the microwave domain. In optical homodyning [27], two linear superpositions of a weak quantum signal with a classical reference signal are generated by feeding them into a beam splitter. By measuring the intensities of these superpositions, the quantum state of the original signal can be reconstructed[1]. Unfortunately, detectors with the performance required for homodyning are not available in the microwave frequency regime. Thus the signals need preamplification, preferably at low temperatures. However, commercially available high electron mobility transistor (HEMT) amplifiers add a certain amount of noise photons to the signal. As photon energies in the microwave domain are much lower than noise contributions of the amplifiers, 'optical' homodyning preceded by amplification does not work. A solution was provided by Menzel *et al.* [25] in the dual-path state reconstruction scheme in 2010. A signal is split at cryogenic temperatures and the two resulting signals are independently amplified. By detecting them at room temperature and exploiting the statistical nature of the added noise, the

---

[1]Additional details can be found in Sec. 2.2

original signal, which otherwise could not be distinguished from noise contributions, is recovered. The method in principle gives access to all quadrature moments of the signal and thus allows for full reconstruction of the Wigner function or a similar representation of the quantum state of the propagating microwave.

In the present thesis, the receiver part of the dual-path state reconstruction scheme for propagating quantum microwaves is discussed. This concerns the room temperature components of the setup introduced in [25]. Although the theoretically possible maximum detection sensitivity is determined by the noise added in cryogenic amplification, the dual-path receiver is at the heart of the method, because all additional possible losses in accuracy are within the receiver. Thus all components of the receiver have to be thoroughly tested and changes in the receiver design have to be well considered. In addition to carefully testing the single components, also the receiver has to be tested and characterized as a black box. As the dual-path receiver is a very sensitive measuring device, considerable effort in terms of measurement equipment and techniques has to be taken in order to achieve satisfying results. Another difficulty is the lack of real quantum signals for testing. Thus a signal emulator has been developed, which mimics the signals generated from a cryogenic setup by means of room temperature components. For example, the statistical properties of linear superpositions are emulated by using appropriate mixtures of coherent signals.

The main goals of this work are (i) complete description of the receiver design, (ii) characterization, (iii) software design and (iv) giving a road map to future experiments and realtime measurements. Precise characterization, especially of noise sources and possible timing problems is a key task to reveal possible pitfalls in using the receiver in future experiments. Measurement software capable of calculating in-phase- (I) and quadrature- (Q) moments has to be developed to allow for Wigner function reconstruction. Finally, a road map for the development of a 4-port receiver with hardware IQ-mixing and realtime measurement capabilities shall be given based on the findings in this work. This work is structured as follows: Chapter 2 gives insight into the theory related to this sophisticated measurement technique. Theoretical considerations will be presented in a classical and a fully quantum mechanical fashion. Chapter 3 is concerned with the composition of the dual-path receiver, giving explanations on the signal emulator, the heterodyne detector, which down converts signals to frequencies detectable with standard digitizers, and the digitizer itself. Additionally, the measurement software and future use of a field programmable gate array (FPGA) is discussed. Chapter 4 treats characterization measurements, proofs of principle and determination of resolution limits. Special emphasis is placed on a precise characterization of the receiver in different aspects like power linearity, decorrelation effects, intrinsic noise sources, jitter and phase stability. Knowing the details of the receiver characteristics, its resolution limit and dependence on factors as ensemble size and noise level is determined. We back up these results by simulation and comparison to results in [25]. Finally, chapter 5 gives a summary of the work done, the remaining tasks and future challenges.

Chapter 2

Theory

In this chapter, the theoretical foundations of this work are presented. First, a short introduction to circuit QED is given and the central topic of this work, state reconstruction of propagating quantum microwaves, is introduced. This is followed by a description of a specific approach towards state reconstruction, the dual-path method [25] and its associated measurement techniques. A concept for state tomography of propagating quantum microwaves based on the dual-path method in combination with signal quadrature measurements is given.

2.1 Circuit quantum electrodynamics (circuit QED)

In optical cavity quantum electrodynamics (cQED), the quantum mechanics governing fundamental light-matter interaction and quantum information processing scenarios are investigated. Its big success is due to the fact that it has given a lot of evidence on fundamental statements in quantum mechanics. The basic idea is to look at the interaction between standing wave light-modes and an atom inside a cavity resonator [1, 2]. Figure 2.1 shows a schematic of a typical cavity QED experiment. The cavity is defined by two semitransparent mirrors and has a resonance frequency $\omega_{\rm r}$. The atom constitutes, in the simplest case, a quantum two-level system with transition frequency ω_{10}. Both entities interact with a coupling strength g. Two main decoherence channels exist, namely the energy decay rate κ of the cavity and the sum γ of the qubit energy relaxation and dephasing rates. κ can be partially controlled by changing the level of transparency of the mirrors at the ends of the cavity. When $\kappa, \gamma << g$ (strong coupling regime) a photon in the cavity is absorbed and reemitted by the atom for many times before it is lost. Many exciting experiments have been performed in this field during the last 20 years in the optical, but also in the microwave domain [1, 2, 27].

In *circuit* QED [10, 11], similar experiments are realized by means of superconducting circuits. Here, transmission line resonators and Josephson junction based
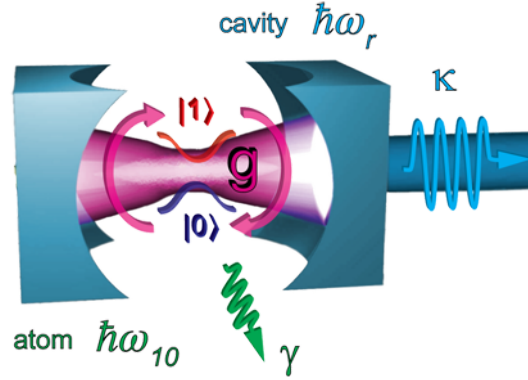
Figure 2.1: Schematic of a typical cavity QED system gazing at the interaction between a two-level system and a light mode (magenta) in an optical cavity. (Picture with kind permission of T. Niemczyk [17])

qubit circuits play the roles of cavities and two-level atoms, respectively (see Fig. 2.2, [10]). The advantages of circuit QED systems, which typically have transition frequencies of a few gigahertz, are design flexibility, *in-situ* tuneability, potential scalability, and exceptionally large coupling strengths [10, 17]. Since the transmis-
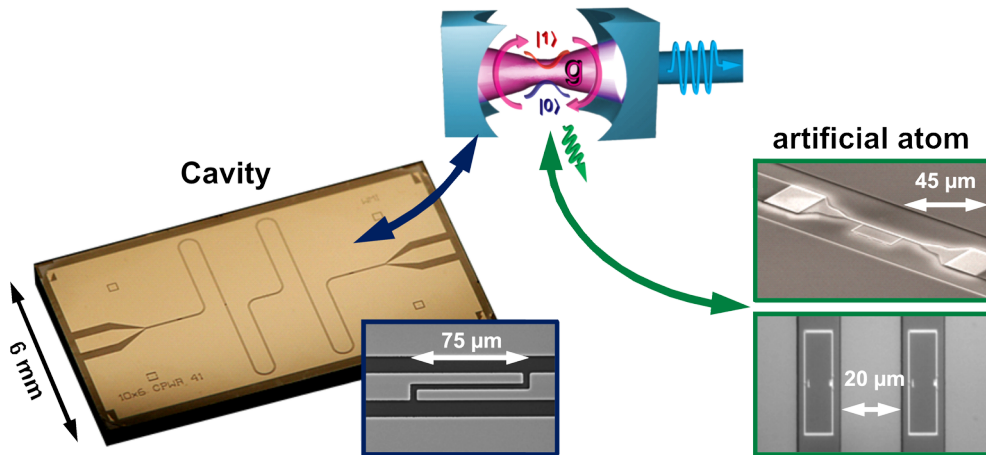

Figure 2.2: In circuit QED, cavities are replaced by transmission line resonators and artificial atoms made of superconducting circuits play the role of the two-level atom. (Picture with kind permission of T. Niemczyk [17])

sion line resonator is coupled to feed lines by means of capacitors (the circuit QED counterpart of the semi-transparent mirrors in cavity QED), non-classical light produced inside the resonator can propagate into the feed lines. The reconstruction of such propagating (or itinerant) quantum microwaves is at the center of the investigations performed during this work. Using input-output theory, a relationship between the mode $\hat{a}$ inside and the mode $\hat{b}$ propagating outside the cavity can be established (see Fig. 2.3, [1, 28, 29]):

$$\hat{b}_{out}(t) = \sqrt{\kappa}\hat{a}(t) - \hat{b}_{in}(t) \quad,$$

, where $\hat{b}_{out}, \hat{a}, \hat{b}_{in}$ are the annihilation operators of the respective modes. Here, we ignore internal losses and take κ to be the rate at which photons leak out of the cavity.
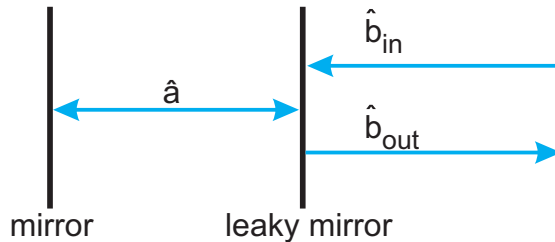

Figure 2.3: Input-output theory representation [1] of an optical cavity with a leaky mirror on one side. The cavity mode is denoted by $\hat{a}$, $\hat{b}_{\text{in}}$ and $\hat{b}_{\text{out}}$ are the in- and output modes.

It has been shown that the correlations of $\hat{b}_{out}$ are proportional to the correlations of $\hat{a}$ when $\hat{b}_{in}$ is prepared in the vacuum state [28]. Finally, it is noteworthy to mention that the source of the dual-path state reconstruction scheme for propagating quantum microwaves is not restricted to single photons leaking out of a resonator. Propagating quantum microwaves can also be generated by, for example, a Josephson parametric amplifier (JPA) [20, 30].

2.2   Optical homodyning

In the following, an overview of optical homodyning [27] and a reason for it *not* being appropriate for the quadrature measurement of quantum microwaves at millikelvin temperatures will be given.

A light mode can be described by its field quadratures [27, 31] $\hat{X}$ and $\hat{P}$, defined as:

$$\hat{X} = \frac{1}{\sqrt{2}} \left(\hat{a}^{\dagger} + \hat{a} \right) \quad \text{and} \tag{2.1}$$

$$\hat{P} = \frac{i}{\sqrt{2}} \left(\hat{a}^{\dagger} - \hat{a} \right) \quad , \tag{2.2}$$

where $\hat{a}, \hat{a}^{\dagger}$ are the ladder operators and $\hat{a} = \frac{1}{\sqrt{2}} \left(\hat{X} + i\hat{P} \right)$. In optics, $\hat{X}$ and $\hat{P}$ correspond to the in-phase and out-of-phase component of the electrical field amplitude of the spatial-temporal mode (with respect to a reference phase). In particular, they do not represent the phase space spanned by the complex vibrational amplitude $\hat{a}$ of the electromagnetic oscillator, and they have nothing to do with the position and momentum of a photon [27].

In an optical homodyne setup as shown in Fig. 2.4 a signal mode $\hat{a}$ interferes with a coherent local oscillator signal α_{LO} at a 50:50 beam splitter. The resulting linear superpositions $\hat{a}'_1 = \frac{1}{\sqrt{2}}(\hat{a} - \alpha_{\text{LO}})$ and $\hat{a}'_2 = \frac{1}{\sqrt{2}}(\hat{a} + \alpha_{\text{LO}})$ are detected in two square-law photo-detectors and the measured intensities are finally subtracted. Defining

the operator $\hat{n}_{21}$ as the difference of the intensity operators $\hat{n}_1, \hat{n}_2$ and treating α_{LO} as a classical coherent state one gets

$$\hat{n}_{21} = \hat{n}_2 - \hat{n}_1 = \alpha_{\mathrm{LO}}^* \hat{a} + \alpha_{\mathrm{LO}} \hat{a}^\dagger = \sqrt{2}|\alpha_{\mathrm{LO}}|\hat{q}_\theta \quad . \tag{2.3}$$

Thus $\hat{n}_{21}$ is proportional to the field quadrature $\hat{q}_\theta = \hat{X}\cos(\theta) + i\hat{P}\sin(\theta)$ relative to the phase difference θ of the coherent local oscillator α_{LO} and $\hat{a}$. Note that $\hat{q}_\theta$ is multiplied by a large $|\alpha_{\mathrm{LO}}|$ and therefore amplified. This amplification allows for measurement of small $\hat{q}_\theta$.
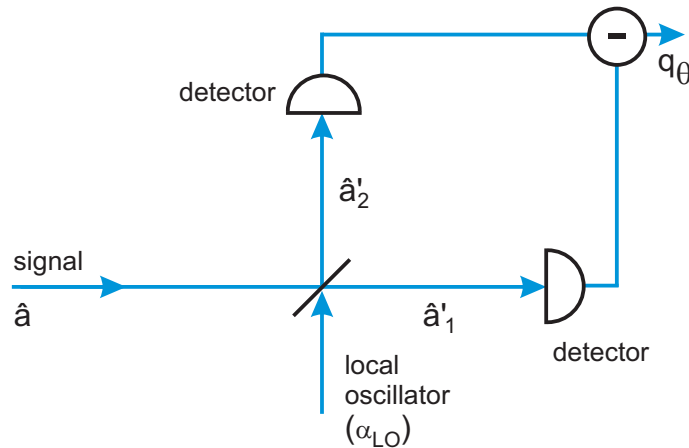

Figure 2.4: Schematic of a quadrature measurement with optical homodyning in quantum optics [27].

2.2.1 Optical homodyning for microwave setups

The following *estimations*, based on an analysis done in detail in the upcoming PhD-thesis of E. P. Menzel, will clarify if the 'optical' homodyning scheme can be used for state reconstruction of propagating quantum microwaves. First, the large number of impressive experiments makes it evident that optical homodyning works very well for frequencies of several hundreds of terahertz at room temperature [2]. In this regime photon energies are very large compared to $k_{\mathrm{B}}T$ and this intuitively makes clear that room temperature noise contributions do *not* have a significant impact in pure optical homodyning. However, detector inefficiencies have to be considered [27, 32, 33].

The situation changes drastically for the analysis of microwave photons, where the energy of a single photon is significantly smaller than the room temperature noise. Thus fluctuations in the artificial atoms, which in the microwave regime are used instead of physical ones [2], will prevent the preparation of quantum states at room-temperature. Since this work is situated in the circuit QED environment, a reasonable approach is to operate the setup at low temperatures. But, generating a non-classical signal at low temperatures and using a room-temperature setup for detection is not very promising. Noise mode contributions at the room-temperature

beam-splitter are not vacuum modes, but thermal modes. Thus, these noise modes will give high contributions and prevent the reconstruction of non-classical signals. The hypothetical next step is to place the beam splitter at cryogenic temperatures to solve the problem of noise contributions at the beam splitter. However, cable losses and detector inefficiencies are remaining problems, e.g. cable losses larger than $3\,\mathrm{dB}$ will cause the reconstruction of Fock-states $|1\rangle$ to fail [27, 32, 33]. Unfortunately, overcoming this problem by locating the whole setup at low temperatures is also not promising, because it is unclear if commercially available square law detectors can be used at these temperatures and provide the required efficiency. Therefore, the option to amplify the split signals at low temperatures and then send them to detectors at room temperature has to be considered. Applying the Caves amplifier model [34] and assuming the usage of commercially available amplifiers, which add more than one noise photon, and following the arguments on noise contributions in Ref. [27] one finds that the reconstruction of a one photon Fock-state gives a Wigner function that is completely positive [35], which of course is wrong (see Sec. 2.6.1). If reasonably high gains are assumed, this result even holds for quantum limited amplifiers, which only add half a noise photon. Due to the above arguments, an alternative approach to the reconstruction of propagating quantum microwaves is used. This so-called dual-path reconstruction scheme forms the principle motivation of this work and is introduced in detail in the next section.

It has to be mentioned that it is possible to directly measure quadrature components of a microwave signal by using phase-sensitive amplifiers such as JPAs [22]. In contrast to using JPAs, the dual-path method aims at a setup with commercially available components and tolerance to some extent of amplifier noise.

2.3   Dual-path method (classical)

Since the principles of optical homodyning cannot be directly adopted to measure quantum microwaves at millikelvin temperatures, Menzel et al. [25] proposed the dual-path method. It offers access to all signal quadrature moments and furthermore to all quadrature moments of the detector noise.

The basic idea of this method is illustrated in Fig. 2.5. A signal $\sqrt{2}S$ is split at low temperatures by means of a 50-50 microwave beam splitter. The resulting signals are independently amplified by means of two amplification chains. Thus the noise contributions χ_1, χ_2 added to the signals are statistically independent. Assuming a perfect $180°$ hybrid ring, a beam splitter model can be used to describe the output signals as $C_1 = G\left(S + V + \chi_1\right)$ and $C_2 = G\left(-S + V + \chi_2\right)$, where G is the amplification gain and V represents an ancilla state at the fourth port of the hybrid ring. It is noteworthy to mention that some knowledge about the ancilla state has to be assumed. To achieve this in experiment, V is prepared in the vacuum or a weak thermal state. Performing an ensemble of measurements, correlations of the form $\left\langle C_1^l C_2^m \right\rangle$ can be computed, where the brackets indicate ensemble averaging
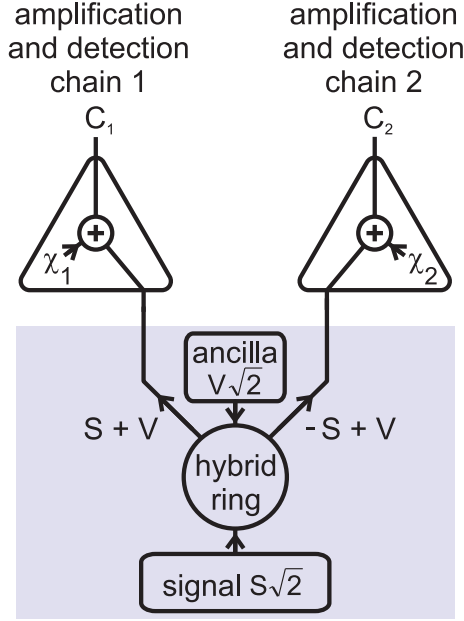
Figure 2.5: Scheme of the dual-path method.
(Picture with kind permission of E.P. Menzel [25]).

and $l, m \in \mathbb{N}$. Although the setup looks similar, this is not a Hanbury Brown-Twiss experiment, because correlations of field quadratures (voltage, see section 2.2) and not of intensities (power) are measured.

For the first signal moment, the mean values $\langle \chi_1 \rangle$ and $\langle \chi_2 \rangle$ vanish and one obtains $\langle S \rangle = \langle C_1 \rangle / G - \langle V \rangle = -\langle C_2 \rangle / G - \langle V \rangle$. All higher moments of signal and noise can be calculated by induction [25]:

$$\langle S^n \rangle = - \langle C_1^{n-1} C_2 \rangle / G^n$$
$$- \sum_{k=1}^{n-1} \sum_{j=0}^{k} \binom{n-1}{k} \binom{k}{j} \langle S^{n-k} \rangle \langle V^j \rangle \langle \chi_1^{k-j} \rangle$$
$$+ \sum_{k=0}^{n-1} \sum_{j=0}^{k} \binom{n-1}{k} \binom{k}{j} \langle S^{n-k-1} \rangle \langle V^{j+1} \rangle \langle \chi_1^{k-j} \rangle \quad , \qquad (2.4)$$

$$\langle \chi_1^n \rangle = + \langle C_1^n \rangle / G^n$$
$$- \sum_{k=1}^{n} \sum_{j=0}^{k} \binom{n}{k} \binom{k}{j} \langle \chi_1^{n-k} \rangle \langle S^{k-j} \rangle \langle V^j \rangle \quad , \qquad (2.5)$$

$$\langle \chi_2^n \rangle = + \langle C_2^n \rangle / G^n$$
$$- \sum_{k=1}^{n} \sum_{j=0}^{k} \binom{n}{k} \binom{k}{j} (-1)^{k-j} \langle \chi_2^{n-k} \rangle \langle S^{k-j} \rangle \langle V^j \rangle \quad . \qquad (2.6)$$

For the above formulas equal gain in both chains, a perfect 180° hybrid ring and mutual statistical independence of S, V, χ_1, χ_2 is assumed. As for a vacuum or thermal ancilla state $\langle V^{2j+1} \rangle = 0$, where $j \in \mathbb{N}$, explicit expressions for the signal moments

and noise moments can be given as

$$G\langle S \rangle = \langle C_1 \rangle = -\langle C_2 \rangle \quad , \tag{2.7}$$

$$G^2\langle S^2 \rangle = -\langle C_1 C_2 \rangle + G^2\langle V^2 \rangle \quad , \tag{2.8}$$

$$G^3\langle S^3 \rangle = -\langle C_1^2 C_2 \rangle - \langle C_1 \rangle \left(\langle C_1^2 \rangle + \langle C_1 C_2 \rangle - 3G^2\langle V^2 \rangle \right) \quad , \tag{2.9}$$

$$G^4\langle S^4 \rangle = -G^4\langle V^4 \rangle - 6G^2\langle V^2 \rangle\langle C_1 C_2 \rangle + 6G^4\langle V^2 \rangle^2$$
$$+ \langle C_1 C_2 \rangle^2 + \langle C_1^2 C_2^2 \rangle - \langle C_1^2 \rangle\langle C_2^2 \rangle \quad , \tag{2.10}$$

$$\langle \chi_1 \rangle \equiv 0 \quad , \tag{2.11}$$

$$G^2\langle \chi_1^2 \rangle = \langle C_1^2 \rangle + \langle C_1 C_2 \rangle - 2G^2\langle V^2 \rangle \quad , \tag{2.12}$$

$$G^3\langle \chi_1^3 \rangle = \langle C_1^3 \rangle + \langle C_1^2 C_2 \rangle - 2\langle C_1 \rangle \left(\langle C_1^2 \rangle + \langle C_1 C_2 \rangle \right) \quad , \tag{2.13}$$

$$G^4\langle \chi_1^4 \rangle = \langle C_1^4 \rangle - 12G^2\langle V^2 \rangle\langle C_1 C_2 \rangle - 12G^2\langle V^2 \rangle\langle C_1^2 \rangle$$
$$+ 6\langle C_1 C_2 \rangle\langle C_1^2 \rangle + 5\langle C_1 C_2 \rangle^2 + 12G^4\langle V^2 \rangle^2$$
$$- 4\langle C_1 \rangle\langle C_1^3 \rangle - 4\langle C_1 \rangle\langle C_1^2 C_2 \rangle + 8\langle C_1 \rangle^2\langle C_1^2 \rangle$$
$$+ 8\langle C_1 \rangle^2\langle C_1 C_2 \rangle - \langle C_1^2 C_2^2 \rangle + \langle C_1^2 \rangle\langle C_2^2 \rangle \quad . \tag{2.14}$$

Analogous equations can be found for $\langle \chi_2^n \rangle, n \in \mathbb{N}$. Because for higher moments many combinations of C_1 and C_2 are possible in the occurring products, these expressions are not unique. Typically, balanced products ($l \approx m$) seem to produce simpler expressions.

The dual-path method as described above, respectively in [25], only considers moments of directly measured voltages. In order to be able to do state reconstruction, the *quadrature* and *complex envelop operator* moments have to be considered, which are introduced in the next sections.

2.4 Measuring quadratures

As stated for light modes in Sec. 2.2, measuring quadratures is the same as measuring the in-phase (I) and the out-of-phase (Q) components of a signal[1]. In the microwave domain this is done by an IQ-Mixer, which is described in the following section. A signal $U(t)$ of the form

$$U(t) = A(t) \cos\left(\omega_{\mathrm{RF}}t - \varphi(t)\right)$$
$$= \underbrace{A(t) \cos\left(\varphi(t)\right)}_{I(t)} \cos\left(\omega_{\mathrm{RF}}t\right) + \underbrace{A(t) \sin\left(\varphi(t)\right)}_{Q)(t)} \sin\left(\omega_{\mathrm{RF}}t\right)$$
$$= I(t) \cos(\omega_{\mathrm{RF}}t) + Q(t) \sin(\omega_{\mathrm{RF}}t)$$

$$\tag{2.15}$$

---

[1]In RF-electronics the quadrature components are called I and Q, whereas they are denoted with $\hat{X}$ and $\hat{P}$ in a quantum mechanical treatment, as in Sec. 2.2.

is fully determined by its amplitude $A(t)$ and phase $\varphi(t)$. Another complete description of the signal is given by its two quadratures $I(t)$ and $Q(t)$. Using I and Q, the amplitude and phase of the original signal can be retrieved by $A(t) = \sqrt{I(t)^2 + Q(t)^2}$, $\varphi(t) = \arctan(Q(t)/I(t))$. This shows that the I, Q-representation completely describes the signal. The quadratures I and Q can be obtained by splitting the signal and mixing it with a local oscillator signal $LO_1 = B\sin(\omega_{\mathrm{LO}}t)$ in one arm and a $\pi/2$-phase shifted signal $LO_2 = B\sin(\omega_{\mathrm{LO}}t + \frac{\pi}{2}) = B\cos(\omega_{\mathrm{LO}}t)$ in the other arm. This results in two signals with components at $\omega_{\mathrm{IF}} = \omega_{\mathrm{RF}} - \omega_{\mathrm{LO}}$ and higher frequencies (sum frequencies). Getting rid of the higher frequencies by an appropriate low-pass filter, the quadratures can be obtained by measuring the output. The device performing all these tasks is called IQ-mixer [36] (see Fig. 2.6).
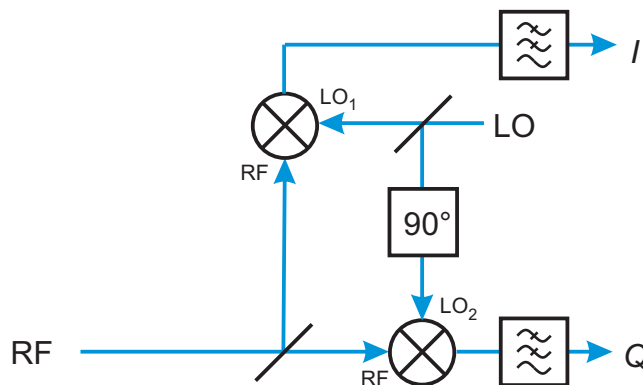

Figure 2.6: Block diagram of an IQ-mixer for decomposing a microwave signal into its in-phase and out-of-phase components I and Q.

Multiplying $U(t)$ by LO_1 and LO_2, respectively, and dropping terms including the sum frequency $(\omega_{\mathrm{LO}} + \omega_{\mathrm{RF}})$ gives:

$$I_{\mathrm{IF}}(t) \propto A(t)\cos(\omega_{\mathrm{IF}}t + \varphi(t)) \quad \text{and} \tag{2.16}$$

$$Q_{\mathrm{IF}}(t) \propto A(t)\sin(\omega_{\mathrm{IF}}t + \varphi(t)) \quad . \tag{2.17}$$

For $\omega_{\mathrm{IF}} = \omega_{\mathrm{RF}} - \omega_{\mathrm{LO}} = 0$ the quadrature components $I = A(t)\cos(\varphi(t))$ and $Q = A(t)\sin(\varphi(t))$ can be measured directly and the detection scheme is called homodyning. Whereas for $\omega_{\mathrm{IF}} \neq 0$ it is called heterodyning. For coherent signals, homodyning produces a DC-output signal $I(t) \propto A\cos(\varphi) = const$ and heterodyning gives an oscillating output $I(t) = A\cos(\omega_{\mathrm{IF}}t + \varphi)$ at the intermediate frequency ω_{IF}. As the DC-output in a homodyne detection scheme is suspect to $1/f$-noise, in the dual-path receiver, a heterodyning scheme followed by digital homodyning [16] is used. In the following *Single Channel Digital Homodyne* and *Dual Channel Digital Homodyne* are described.

Single Channel Digital Homodyne

It is possible to reconstruct IQ-information from only one channel of an IQ-mixer [16]. In practice this means that instead of using an IQ-mixer an ordinary mixer can be

used (see Fig. 2.7). The advantage of this method is that only one digitizer port
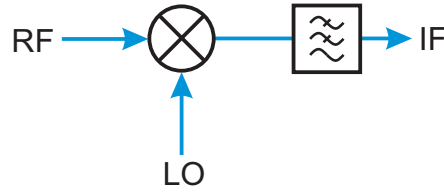

Figure 2.7: Block diagram of a mixer converting a radio frequency signal
RF into an intermediate frequency IF by mixing it with a local oscillator
LO and filtering out higher frequency components.

for detecting both, I and Q, is needed. For this reason, this method is used for all
measurements in this work. A signal which has already been converted down to an
intermediate frequency ω_{IF},

$$IF(t) = A(t)\cos(\omega_{\mathrm{IF}}t + \phi(t)) \quad , \tag{2.18}$$

can be digitally mixed down to DC in an IQ-fashion. This is done by imitating
the working principle of an IQ-mixer. The signal is multiplied by $\cos(\omega_{\mathrm{IF}}\tau)$ and by
$\sin(\omega_{\mathrm{IF}}\tau)$, respectively and the resulting signal is digitally low pass filtered. The low
pass filtering is implemented as an integration over one period of the IF-frequency.
This yields

$$I(t) = \frac{1}{2\pi/\omega_{\mathrm{IF}}} \int_{t}^{t+2\pi/\omega_{\mathrm{IF}}} \cos(\omega_{\mathrm{IF}}\tau)IF(\tau)d\tau \quad \text{and} \tag{2.19}$$

$$Q(t) = \frac{1}{2\pi/\omega_{\mathrm{IF}}} \int_{t}^{t+2\pi/\omega_{\mathrm{IF}}} \sin(\omega_{\mathrm{IF}}\tau)IF(\tau)d\tau \quad . \tag{2.20}$$

As can easily be seen this method involves a certain loss of time resolution.

Dual Channel Digital Homodyne

As mentioned before, the IQ mixer is used in heterodyne-mode in order to avoid $1/f$-
noise. Thus, the signals $I_{\mathrm{IF}}(t), Q_{\mathrm{IF}}(t)$ digitized at the output-ports of the IQ-mixer
are still oscillating at the intermediate frequency ω_{IF}. Plotting I and Q components
of a coherent signal in Cartesian coordinates, this gives a point describing a circle
within its time evolution. In order to compensate for this, one uses a frame rotating
at the IF frequency. This is done by means of a rotation matrix

$$R(t) = \begin{pmatrix} \cos(\omega_{\mathrm{IF}}t) & \sin(\omega_{\mathrm{IF}}t) \\ -\sin(\omega_{\mathrm{IF}}t) & \cos(\omega_{\mathrm{IF}}t) \end{pmatrix}. \tag{2.21}$$

Assuming that there are no imbalances in the IQ mixer, this gives

$$I(t) = A(t)\cos(\varphi(t)) \quad , \tag{2.22}$$

$$Q(t) = A(t)\sin(\varphi(t)). \tag{2.23}$$

As this method is not used for data generated in this work, details, e.g. on compen-
sating mixer imbalances, are not discussed here. They can be found in Ref. [16].

2.5   Complex envelope S (quantum mechanical)

For theoretical considerations, the IQ detector is modeled as a beam splitter and an I- and a Q-detector at its output ports (see Fig. 2.8). In order to model a matched, lossless, and reciprocal beam splitter, a device with four ports is used. At the second input port [28], a thermal or vacuum state is assumed.
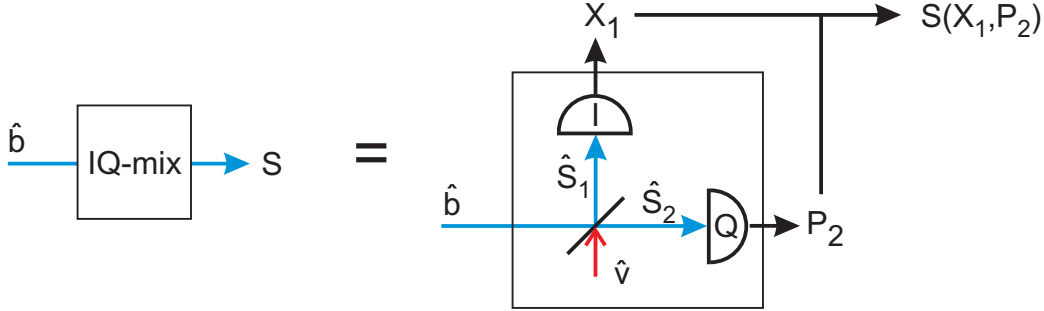

Figure 2.8: Model for an IQ-mixer. The *IQ-mix* symbol represents the model consisting of a beam splitter with a vacuum mode at its second input port and I and Q detectors connected to its outputs. The complex envelope S is built from the detector outputs.

The beam splitter superposes two input modes $\hat{b}$ and $\hat{v}^\dagger$ and the resulting signals are $\hat{S}_{1,2}(t)$:

$$\begin{pmatrix} \hat{S}_1 \\ \hat{S}_2 \end{pmatrix} := \frac{1}{\sqrt{2}} \begin{pmatrix} 1 & 1 \\ 1 & -1 \end{pmatrix} \cdot \begin{pmatrix} \hat{b} \\ \hat{v} \end{pmatrix} = \frac{1}{\sqrt{2}} \begin{pmatrix} \hat{b} + \hat{v} \\ \hat{b} - \hat{v} \end{pmatrix} \tag{2.24}$$

The I-detector at port 1 measures the quadrature component $\hat{X}_1$ of $\hat{S}_1$, the Q-detector at port 2 measures $\hat{P}_2$ of $\hat{S}_2$ (see Fig. 2.8). This gives:

$$\hat{X}_1 := \frac{\hat{S}_1 + \hat{S}_1^\dagger}{\sqrt{2}} = \frac{\hat{b} + \hat{v}^\dagger + \hat{b}^\dagger + \hat{v}}{2} \tag{2.25}$$

$$\hat{P}_2 := -i \cdot \frac{\hat{S}_2 - \hat{S}_2^\dagger}{\sqrt{2}} = -i \cdot \frac{\hat{b} - \hat{v}^\dagger - (\hat{b}^\dagger - \hat{v})}{2} \tag{2.26}$$

$$\tag{2.27}$$

Next, we define a complex envelope operator $\hat{S}$ and express it by means of $\hat{X}_1$ and $\hat{P}_2$:

$$\hat{S} := \hat{b} + \hat{v}^\dagger = \hat{X}_1 + i\hat{P}_2 \tag{2.28}$$

As measuring the in-phase and out-of-phase components of $\hat{S}$ is equivalent to determine eigenvalues of $\hat{X}_1$ and $\hat{P}_2$, we can give the expectation values of an ensemble of measurements:

$$\langle X_1(t)\rangle = \left\langle \hat{X}_1(t)\right\rangle \qquad \wedge \qquad \langle P_2(t)\rangle = \left\langle \hat{P}_2(t)\right\rangle \tag{2.29}$$

Thus the complex envelope S of $\hat{b}$ can be introduced as:

$$S(t) := X_1(t) + iP_2(t) \tag{2.30}$$

and the mean value of the measured ensemble takes the same value as the expectation value of the realizations of the operator $\hat{S}$:

$$\langle S(t)\rangle = \left\langle \hat{S}(t)\right\rangle \tag{2.31}$$

Given that $\hat{v}$ is in the vacuum state, it can be derived that the commutor [28]:

$$[\hat{S}(t), \hat{S}^\dagger(t')] = 0 \quad . \tag{2.32}$$

Following [28], it can be shown that autocorrelations of the complex envelope of a field correspond to antinormally ordered autocorrelations of the field operator, under the assumption that the $\hat{v}$ mode is prepared in the vacuum:

$$\langle (S^*)^m S^n\rangle = \left\langle (\hat{S}^\dagger)^m \hat{S}^n\right\rangle = \left\langle (\hat{b}^\dagger + \hat{v})^m (\hat{b} + \hat{v}^\dagger)^n\right\rangle$$

$$\implies \langle (S^*)^m S^n\rangle = \left\langle (\hat{S}^\dagger)^m \hat{S}^n\right\rangle = \left\langle \hat{b}^n (\hat{b}^\dagger)^m\right\rangle \tag{2.33}$$

Summarizing, it can be stated that antinormally ordered moments of arbitrary order of the complex envelope operator $\langle \hat{S}^{\dagger\,l} \hat{S}^m\rangle, \quad l, m \in \mathbb{N}$ of a microwave signal can be measured by gaining access to the IQ-components or $\hat{X}, \hat{P}$, respectively. Note that this does not yet solve the problem of measuring propagating quantum microwaves, because amplifier noise has not been taken into account. To do so the IQ-moment-detection has to be combined with the dual-path method, which is done in the next section.

2.6   Dual-path method (quantum mechanical)

In section 2.3, it was shown how the dual-path setup works and that it gives access to all signal and noise moments. In this section, it will be reviewed with respect to the quantum aspects and to signal quadrature moments. Figure 2.9 shows the model of the setup. It shall be explicitly noted that the theoretical considerations for Sec. 2.6 are results of a collaboration with the group of Prof. Enrique Solano from Universidad del País Vasco in Bilbao, Spain. The derivation of the quantum mechanical treatment of the dual-path method has been done by Daniel Ballester and Roberto Di Candia and will be published elsewhere soon.

The first element of the setup is a hybrid ring, which is modeled as a 50:50 beam
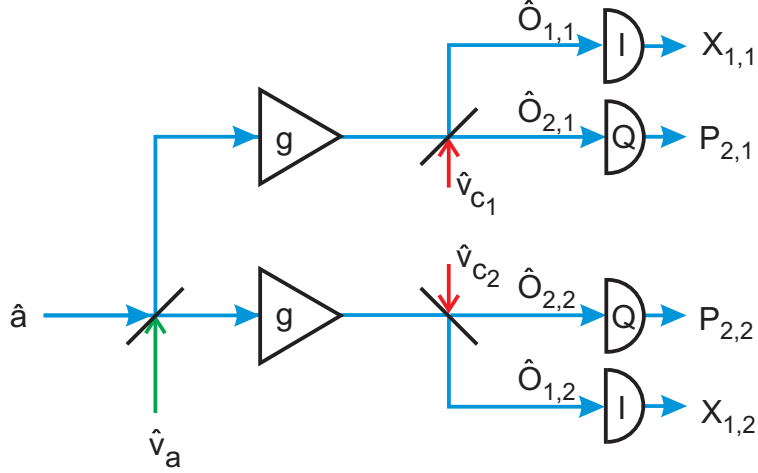
Figure 2.9: Schematic sketch of the dual-path setup considering quantum effects introduced by taking into account ancilla state $\hat{v}_a$ at the hybrid ring, and noise modes added in amplifiers and in IQ-mixers $\hat{v}_{C1,2}$

.

splitter with two bosonic input modes $\hat{a}$ and $\hat{v}_a$. Here, $\hat{a}$ is the propagating microwave mode of interest and $\hat{v}_a$ is a known ancilla state as already discussed in 2.3. The output of the hybrid is then given as:

$$\begin{pmatrix} \hat{c}_1 \\ \hat{c}_2 \end{pmatrix} = \frac{1}{\sqrt{2}} \begin{pmatrix} 1 & 1 \\ -1 & 1 \end{pmatrix} \begin{pmatrix} \hat{a} \\ \hat{v}_a \end{pmatrix} = \frac{1}{\sqrt{2}} \begin{pmatrix} \hat{a} + \hat{v}_a \\ -\hat{a} + \hat{v}_a \end{pmatrix} . \tag{2.34}$$

The next step is amplification of the signals $\hat{c}_1$ and $\hat{c}_2$. The amplification is modeled following Caves [34],

$$\hat{C}_k = \sqrt{g_k}\, \hat{c}_k + \sqrt{g_k - 1}\, \hat{h}_k^\dagger, \quad k = 1, 2 \quad , \tag{2.35}$$

with $\hat{h}_k^\dagger$ being the creation operator of the added noise in the amplification process. C_k is a bosonic mode and thus has to satisfy the standard bosonic commutation relations. In the following it will be assumed that the power gains g_1 and g_2 are equal, thus $g := g_1 = g_2$.

The last component of each chain is an IQ-Mixer to extract the quadrature moments of the signal. Its theoretical treatment has already been given in Sec. 2.4. The output is:

$$\begin{pmatrix} \hat{O}_{1,k} \\ \hat{O}_{2,k} \end{pmatrix} = \frac{1}{\sqrt{2}} \begin{pmatrix} 1 & 1 \\ 1 & -1 \end{pmatrix} \begin{pmatrix} \hat{C}_k \\ \hat{v}_{C_k} \end{pmatrix} = \frac{1}{\sqrt{2}} \begin{pmatrix} \hat{C}_k + \hat{v}_{C_k} \\ \hat{C}_k - \hat{v}_{C_k} \end{pmatrix}, \tag{2.36}$$

where $\hat{C}_k$ is the input signal as derived in Eq. (2.35), $\hat{v}_{C_k}$ is the noise at the fourth port of the IQ-Mixer and the index k gives the dual-path channel (see also Fig. 2.9). The quadratures of these output bosonic modes are given by

$$\hat{X}_{1,k} = \frac{\hat{O}_{1,k} + \hat{O}_{1,k}^\dagger}{\sqrt{2}} \quad \text{and} \tag{2.37}$$

$$\hat{P}_{2,k} = -i\frac{\hat{O}_{2,k} - \hat{O}_{2,k}^\dagger}{\sqrt{2}} \quad . \tag{2.38}$$

The measurable envelope signal then becomes

$$\hat{\xi}_k := \hat{X}_{1,k} + i\hat{P}_{2,k} \tag{2.39}$$

which, as already shown, is equal to

$$\hat{\xi}_k = \hat{C}_k + \hat{v}_{C_k}^\dagger. \tag{2.40}$$

Finally, all elements described above are combined to yield the following equalities:

$$\begin{aligned}
\hat{\xi}_1 &= \frac{\sqrt{g}}{\sqrt{2}}\,\hat{a} + \frac{\sqrt{g}}{\sqrt{2}}\,\hat{v}_a + \sqrt{g-1}\,\hat{h}_1^\dagger + \hat{v}_{C_1}^\dagger \\
\hat{\xi}_2 &= -\frac{\sqrt{g}}{\sqrt{2}}\,\hat{a} + \frac{\sqrt{g}}{\sqrt{2}}\,\hat{v}_a + \sqrt{g-1}\,\hat{h}_2^\dagger + \hat{v}_{C_2}^\dagger
\end{aligned} \tag{2.41}$$

In the following, some operators are defined to simplify the notation

$$\hat{V}_k^\dagger := \frac{\sqrt{2}}{\sqrt{g}}\left(\sqrt{g-1}\,\hat{h}_k^\dagger + \hat{v}_{C_k}\right) \quad, \tag{2.42}$$

$$\hat{S}_k := \frac{\sqrt{2}}{\sqrt{g}}\hat{\xi}_k \quad, \tag{2.43}$$

$$\hat{S}_1 = \hat{a} + \hat{v}_a + \hat{V}_1^\dagger \quad, \tag{2.44}$$

$$\hat{S}_2 = -\hat{a} + \hat{v}_a + \hat{V}_2^\dagger \quad. \tag{2.45}$$

Comparing this notation to the classical case (see Sec. 2.3), some differences are evident. The signal which ultimately shall be reconstructed is called S in Sec. 2.3, whereas here it is represented by the signal mode operator $\hat{a}$. Furthermore, the ancilla state V is represented by the operator $\hat{v}_a$ and the noise contributions in each channel are contained in the noise operators $\hat{V}_{1,2}$.

Now, the field moments $\left\langle(\hat{a}^\dagger)^l\hat{a}^m\right\rangle$ can be deduced from the directly measurable moments $\left\langle(\hat{S}_1^\dagger)^{l_1}(\hat{S}_2^\dagger)^{l_2}\hat{S}_2^{m_2}\hat{S}_1^{m_1}\right\rangle$. Using the above definitions, one can obtain explicit formulas for the moments of the original signal, $\left\langle(\hat{a}^\dagger)^l\hat{a}^m\right\rangle$, and the moments of the noise operators, $\left\langle\hat{V}_1^r(\hat{V}_1^\dagger)^s\right\rangle$ and $\left\langle\hat{V}_2^r(\hat{V}_2^\dagger)^s\right\rangle$:

$$\left\langle (\hat{a}^\dagger)^l \hat{a}^m \right\rangle = (-1)^{l_2+m_2} \left\langle (\hat{S}_1^\dagger)^{l_1} (\hat{S}_2^\dagger)^{l_2} \hat{S}_2^{m_2} \hat{S}_1^{m_1} \right\rangle$$

$$- \sum_{k_1=0}^{l_1} \sum_{k_2=0}^{l_2} \sum_{j_1=0}^{m_1} \sum_{j_2=0}^{m_2-1} \sum_{k_1'=0}^{l_1-k_1} \sum_{k_2'=0}^{l_2-k_2} \sum_{j_1'=0}^{m_1-j_1} \sum_{j_2'=0}^{m_2-j_2} \binom{l_1}{k_1} \binom{l_2}{k_2} \binom{m_1}{j_1} \binom{m_2}{j_2} \binom{l_1-k_1}{k_1'} \binom{l_2-k_2}{k_2'}$$

$$\times \binom{m_1-j_1}{j_1'} \binom{m_2-j_2}{j_2'} (-1)^{l_2+m_2+j_2+k_2} \left\langle (\hat{a}^\dagger)^{k_1+k_2} \hat{a}^{j_1+j_2} \right\rangle \left\langle (\hat{v}_a^\dagger)^{k_1'+k_2'} \hat{v}_a^{j_2'+j_1'} \right\rangle$$

$$\times \left\langle \hat{V}_1^{\,l_1-k_1-k_1'} (\hat{V}_1^\dagger)^{m_1-j_1-j_1'} \right\rangle \left\langle \hat{V}_2^{\,l_2-k_2-k_2'} (\hat{V}_2^\dagger)^{m_2-j_2-j_2'} \right\rangle$$

$$- \sum_{k_1=0}^{l_1} \sum_{k_2=0}^{l_2} \sum_{j_1=0}^{m_1-1} \sum_{k_1'=0}^{l_1-k_1} \sum_{k_2'=0}^{l_2-k_2} \sum_{j_1'=0}^{m_1-j_1} \binom{l_1}{k_1} \binom{l_2}{k_2} \binom{m_1}{j_1} \binom{l_1-k_1}{k_1'} \binom{l_2-k_2}{k_2'} \binom{m_1-j_1}{j_1'}$$

$$\times (-1)^{l_2+k_2} \left\langle (\hat{a}^\dagger)^{k_1+k_2} \hat{a}^{j_1+m_2} \right\rangle \left\langle (\hat{v}_a^\dagger)^{k_1'+k_2'} \hat{v}_a^{j_1'} \right\rangle \left\langle \hat{V}_1^{\,l_1-k_1-k_1'} (\hat{V}_1^\dagger)^{m_1-j_1-j_1'} \right\rangle \left\langle \hat{V}_2^{\,l_2-k_2-k_2'} \right\rangle$$

$$\times \left\langle \hat{V}_2^{\,l_2-k_2-k_2'} \right\rangle$$

$$- \sum_{k_1=0}^{l_1} \sum_{k_2=0}^{l_2-1} \sum_{k_1'=0}^{l_1-k_1} \sum_{k_2'=0}^{l_2-k_2} \binom{l_1}{k_1} \binom{l_2}{k_2} \binom{l_1-k_1}{k_1'} \binom{l_2-k_2}{k_2'} (-1)^{l_2+k_2} \left\langle (\hat{a}^\dagger)^{k_1+k_2} \hat{a}^m \right\rangle \left\langle (\hat{v}_a^\dagger)^{k_1'+k_2'} \right\rangle$$

$$\times \left\langle \hat{V}_1^{\,l_1-k_1-k_1'} \right\rangle \left\langle \hat{V}_2^{\,l_2-k_2-k_2'} \right\rangle \left\langle \hat{V}_2^{\,l_2-k_2-k_2'} \right\rangle$$

$$- \sum_{k_1=0}^{l_1-1} \sum_{k_1'=0}^{l_1-k_1} \binom{l_1}{k_1} \binom{l_1-k_1}{k_1'} \left\langle (\hat{a}^\dagger)^{k_1+l_2} \hat{a}^m \right\rangle \left\langle (\hat{v}_a^\dagger)^{k_1'} \right\rangle \left\langle \hat{V}_1^{\,l_1-k_1-k_1'} \right\rangle \left\langle \hat{V}_2^{\,l_2-k_2-k_2'} \right\rangle,$$

$$(2.46)$$

$$\left\langle \hat{V}_1^r (\hat{V}_1^\dagger)^s \right\rangle = \left\langle (\hat{S}_1^\dagger)^r \hat{S}_1^s \right\rangle$$

$$- \sum_{k_1=0}^{r} \sum_{j_1=0}^{s-1} \sum_{k_1'=0}^{r-k_1} \sum_{j_1'=0}^{s-j_1} \binom{r}{k_1} \binom{s}{j_1} \binom{r-k_1}{k_1'} \binom{s-j_1}{j_1'} \left\langle (\hat{a}^\dagger)^{k_1'} \hat{a}^{j_1'} \right\rangle$$

$$\times \left\langle (\hat{v}_a^\dagger)^{r-k_1-k_1'} \hat{v}_a^{s-j_1-j_1'} \right\rangle \left\langle \hat{V}_1^{k_1} (\hat{V}_1^\dagger)^{j_1} \right\rangle$$

$$- \sum_{k_1=0}^{r-1} \sum_{k_1'=0}^{r-k_1} \binom{r}{k_1} \binom{r-k_1}{j_1'} \left\langle (\hat{a}^\dagger)^{k_1'} \right\rangle \left\langle (\hat{v}_a^\dagger)^{r-k_1-k_1'} \right\rangle \left\langle \hat{V}_1^{k_1} (\hat{V}_1^\dagger)^s \right\rangle,$$

$$(2.47)$$

$$\left\langle \hat{V}_2^r (\hat{V}_2^\dagger)^s \right\rangle = \left\langle (\hat{S}_2^\dagger)^r \hat{S}_2^s \right\rangle$$

$$- \sum_{k_1=0}^{r} \sum_{j_1=0}^{s-1} \sum_{k_1'=0}^{r-k_1} \sum_{j_1'=0}^{s-j_1} \binom{r}{k_1} \binom{s}{j_1} \binom{r-k_1}{k_1'} \binom{s-j_1}{j_1'} (-1)^{k_1'+j_1'} \left\langle (\hat{a}^\dagger)^{k_1'} \hat{a}^{j_1'} \right\rangle$$

$$\times \left\langle (\hat{v}_a^\dagger)^{r-k_1-k_1'} \hat{v}_a^{s-j_1-j_1'} \right\rangle \left\langle \hat{V}_2^{k_1} (\hat{V}_2^\dagger)^{j_1} \right\rangle$$

$$- \sum_{k_1=0}^{r-1} \sum_{k_1'=0}^{r-k_1} \binom{r}{k_1} \binom{r-k_1}{j_1'} (-1)^{k_1'} \left\langle (\hat{a}^\dagger)^{k_1'} \right\rangle \left\langle (\hat{v}_a^\dagger)^{r-k_1-k_1'} \right\rangle \left\langle \hat{V}_2^{k_1} (\hat{V}_2^\dagger)^s \right\rangle.$$

$$(2.48)$$

Here we have set $m_1 + m_2 = m$ and $l_1 + l_2 = l$.

It can be stated that the ancilla operator satisfies $\left\langle (\hat{v}_a^\dagger)^q \hat{v}_a^{q'} \right\rangle = 0$ whenever $q \neq q'$, because this state is prepared in a thermal distribution. Likewise one sets $\left\langle \hat{h}_k \right\rangle = \left\langle \hat{h}_k^\dagger \right\rangle = 0$, and $\langle \hat{v}_{C_k} \rangle = \left\langle \hat{v}_{C_k}^\dagger \right\rangle = 0$, for both branches.

Of the many possible strategies to compute the signal moments $\left\langle (\hat{a}^\dagger)^l \hat{a}^m \right\rangle$ from the previous formula, the one that seems most appealing for the dual-path method is the symmetrized case:

$$
\begin{aligned}
l_1 &= \left\lceil \tfrac{l}{2} \right\rceil && \text{(ceil of } l/2) \\
l_2 &= \left\lfloor \tfrac{l}{2} \right\rfloor && \text{(floor of } l/2) \\
m_1 &= \left\lfloor \tfrac{m}{2} \right\rfloor && \text{(floor of } m/2) \\
m_2 &= \left\lceil \tfrac{m}{2} \right\rceil && \text{(ceil of } m/2)
\end{aligned}
$$

This will allow to cancel higher order moments of the noise (note that $l_1 + l_2 = l$ and $m_1 + m_2 = m$ hold). For example, with this choice one gets

$$
\left\langle \hat{a}^\dagger \hat{a} \right\rangle = \left\langle \hat{S}_1^\dagger \hat{S}_2 \right\rangle - \left\langle \hat{v}_a^\dagger \, \hat{v}_a \right\rangle, \tag{2.49}
$$

where $\left\langle \hat{v}_a^\dagger \, \hat{v}_a \right\rangle$ is known.

In this spirit, recursive formulas can be derived that will allow to calculate the moments of the original signal and of the added noise from the experimentally accessible moments of the envelope signal. In fact, if one makes use of the symmetrized strategy to determine $\left\langle (\hat{a}^\dagger)^l \hat{a}^m \right\rangle$, then one will only need knowledge of the moments $\left\langle \hat{V}_1^r (\hat{V}_1^\dagger)^s \right\rangle$ and $\left\langle \hat{V}_2^r (\hat{V}_2^\dagger)^s \right\rangle$, with r, s up to $r = \left\lceil \tfrac{l}{2} \right\rceil$, $s = \left\lfloor \tfrac{m}{2} \right\rfloor$ and $r = \left\lfloor \tfrac{l}{2} \right\rfloor$, $s = \left\lceil \tfrac{m}{2} \right\rceil$, respectively.

2.6.1   Wigner function reconstruction

The Wigner function [37] is a quasi probability distribution and it carries the same information about a quantum state as the density matrix $\hat{\rho}$. It is defined as [27]

$$
W(q, p) = \frac{1}{2\pi} \int_{-\infty}^{+\infty} e^{ipx} \left\langle q - \frac{x}{2} \middle| \hat{\rho} \middle| q + \frac{x}{2} \right\rangle dx, \tag{2.50}
$$

where q and p span the phase space. For classical states, the Wigner function cannot take negative values. Hence, if one is able to demonstrate that the Wigner function of an experimentally generated state is negative in some regions, one can be certain that it is a quantum state. As prototypical examples, the Wigner functions of a Fock- and a vacuum-state can be found in Fig. 2.10.

The key motivation for setting up and characterizing the dual-path receiver, the state reconstruction of propagating microwaves, translates into Wigner function reconstruction. However, the details of the reconstruction process are beyond the
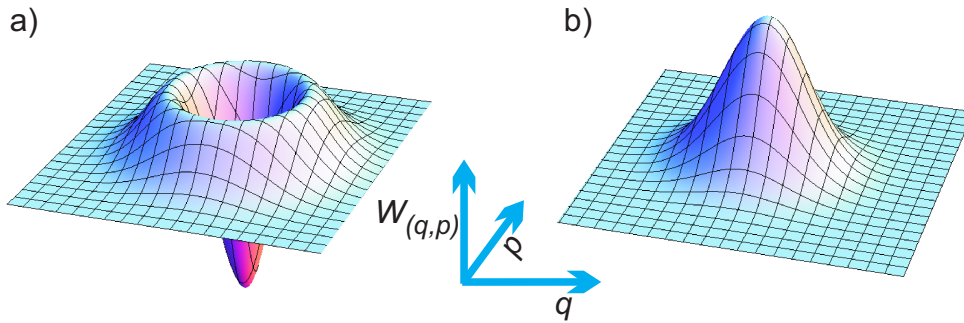
Figure 2.10: Wigner functions of (a) a Fock state $|1\rangle$ and (b) a vacuum
state. In (a) the red regions below the blue plane identify the shown state
as a quantum state. This, of course, is true for a Fock state.

scope of this work. In brief, the expectation value inside the integral of Eq. (2.49)
can be expressed as a function of the expectation values $\langle (\hat{a}^{\dagger})^{l} \hat{a}^{m} \rangle$ of the quadrature
moments reconstructed as shown in Sec. 2.5. Considering that from a given set of
experimental data the quadrature moments can be extracted reliably only up to a
certain order, there are at least two different approaches to calculate the Wigner
function from such data:

Truncation This method assumes all moments higher then a certain order to be
zero. This method is expected to work well for Fock states. However, it is
not very accurate when Gaussian states, such as squeezed states, have to be
analyzed. The mathematical foundation of this work is a truncated Taylor
expansion of the displacement operator [2].

Maximum entropy principle This approach optimizes parameters of reconstruc-
tion based on the maximum entropy principle [38]. It is best suited for Gaus-
sian states.

Chapter 3

Experimental techniques

This chapter covers the experimental setup, the measurement software and the characterization of the dual-path receiver. Section 3.1 describes the experimental setup and its components. Section 3.2 treats software requirements and their implementation. Finally, Sec. 3.3 gives an introduction to realtime measurements.

3.1   Experimental setup

As explained in Sec. 2.3, the dual-path method splits a signal and separately amplifies the outputs (see schematic in Fig. 3.1) for reconstruction of the original signal by means of statistical methods. The focus of this work is on the receiver part of the dual-path setup which exclusively consists of room-temperature components. To build up a realistic test environment, the cryogenic part (see Fig. 3.1), which in the original experiment splits and amplifies the signals with unavoidably adding noise, is emulated by room-temperature components. In the following, this part of the setup will be called *signal emulator* and is explained in subsection 3.1.1. The dual-path receiver itself is divided into the *heterodyne converter* and the *digitizer*. The heterodyne converter is responsible for the down conversion of the signals and is covered in section 3.1.2. The digitizer converts the analog signal to digital data and is described in section 3.1.3. A schematic overview of the setup is shown in Fig. 3.2 and a complete block diagram can be found in Sec. 3.1.4. A description of the symbols used is given in App. A.
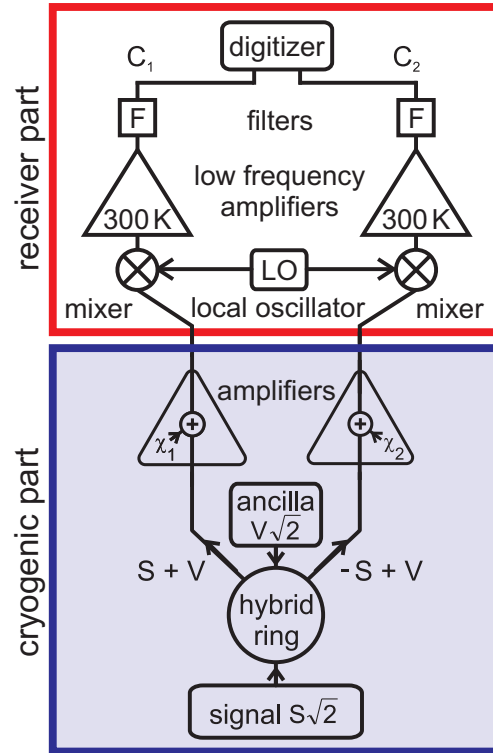
Figure 3.1: Scheme of the dual-path method with the receiver part marked by a red rectangle. (Picture with kind permission of E. P. Menzel [25]).
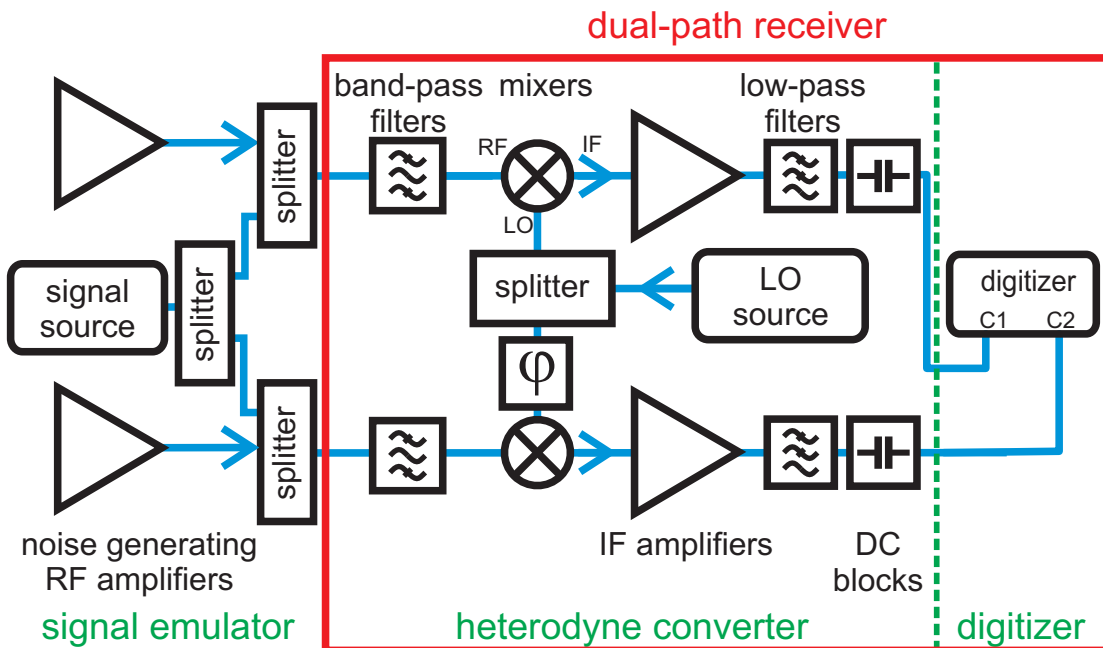
Figure 3.2: Setup for dual-path receiver tests.

3.1.1   Signal emulator

The *signal emulator* (see Fig. 3.3) generates the signals and noise required to characterize the dual-path receiver. Essentially, the signal emulator mimics a weak mi-
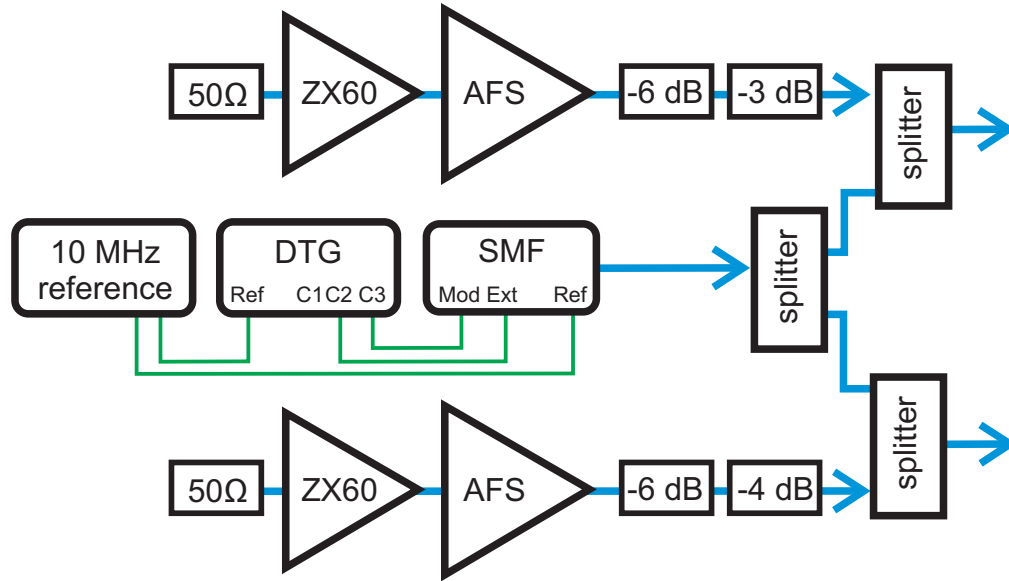
Figure 3.3: Test setup: *Signal emulator.*

crowave signal which is split and amplified by noisy amplifiers. To this end, the
signal is generated directly at an amplitude equal to that of the amplified weak sig-
nal. The emulated signal is at a frequency of $5 - 6$ GHz, which is typical for circuit
QED experiments and where the hybrid ring used in future experiments works as
a 50:50 beam-splitter. In order to obtain a realistic signal-to-noise ratio, additional
white noise is added. The signals, coherent microwaves pulses, are generated by a
Rohde & Schwarz SMF100A signal generator (see App. A.2.1). The duty time of the
pulses and their phase are externally controlled by a Tektronix DTG5334 data tim-
ing generator (see App. A.4.1) sending trigger-signals to the SMF100A. The signal
pulse is triggered every 20 µs with a duty time of 1 µs. To guarantee synchronization,
SMF and DTG are connected to a Rb-reference. In order to emulate the splitting
of the signal in the hybrid ring, the signal is split with a Miteq ZFRSC-183-S+ (see
App. A.1.4) resistive power divider. Therefore, the power of each of the resulting
signals is reduced by 6 dB with respect to the SMF output power. Finally, at the
output ports of the *signal emulator* a signal level 11.4 dB lower than the value set
at the microwave source is obtained. In contrast to the signals split by the hybrid
ring in the original setup, the outputs of the resistive power divider have no relative
phase shift.

In the next step, white noise is added via a reversely mounted power divider to each
signal chain. For this purpose the thermal noise of a $50\,\Omega$ load at room temperature
amplified by a Mini-Circuits ZX60-6013E (see App. A.2.2) together with the noise
added by the amplifier is used. This gives amplified thermal noise which again is
amplified by an AFS amplifier (see App. A.2.2). In order to compensate for gain
inequalities of the two amplifiers and to get the desired signal to noise ratio, the out-
puts are attenuated to appropriate levels. We emphasize that separate noise sources
are used for the two signal chains to ensure statistical independence.

3.1.2   Heterodyne converter

The *heterodyne converter* is required because capturing the signal at its full band-width and original frequency in the gigahertz range would produce a lot more data than can be processed. The *heterodyne converter* realizes a frequency-conversion of the signal of interest to an intermediate frequency in the megahertz regime, so it can be digitized at a sampling rate of a few hundreds of megahertz. The sampling rate by intention is much higher than the one required by the *Nyquist-Shannon sampling theorem* [39], in order to resolve a few data points per signal period for visualization. Also, the cut off of the final low pass filters used in the setup is not perfectly steep, so the additional bandwidth is used to avoid possible aliasing artifacts.

The dual-path receiver is designed according to the well known heterodyne or super-heterodyne principle [40]. However, it consists of two separate branches, one for each amplification and detection chain, as can be seen in Fig. 3.4. For each chain, the
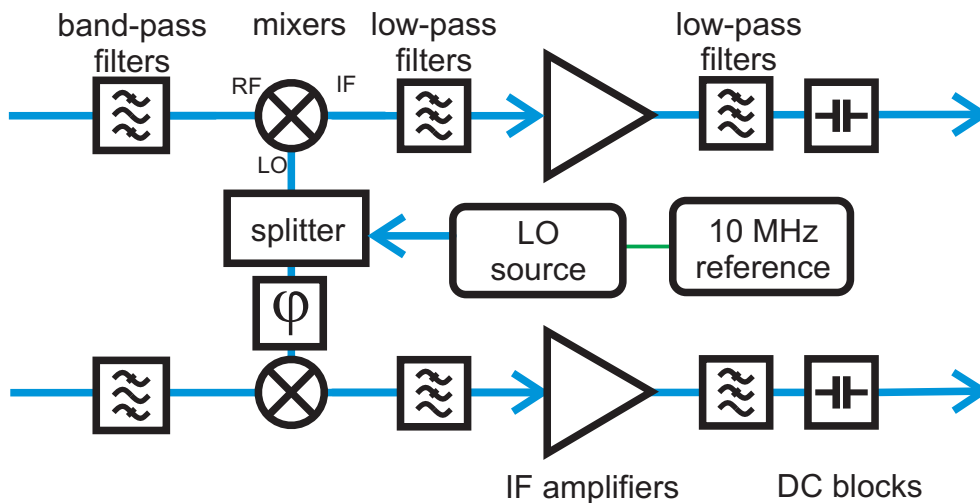
Figure 3.4: Test setup: *Heterodyne converter.*

incoming signal is first band pass filtered to limit it to the frequency-band of interest and to avoid saturation of the mixer with power originating from noise-contributions outside this band. In the next step, the signal is down-converted by mixing it with a slightly detuned local oscillator (LO). In one of the arms, a delay can be induced by means of a computer controlled phase-shifter (see App. A.1.6) in order to compensate for different cable lengths and signal propagation times in the two arms. Typical RF and LO frequencies are 5-6 GHz, intermediate frequencies range from 5 to 16 MHz. The down-converted signal may nevertheless contain frequencies higher than 25 MHz, which are not of interest in the experiment, and so the signal is again low pass filtered before entering an IF-amplifier. In this way, one can extend the dynamic range of the dual-path receiver. The amplitude of the amplified signal is chosen such that one can make full use of the input-range of the digitizer hardware.

Finally, another low-pass filter damps high frequency fluctuations and a DC-block is used to eliminate a possible DC-bias.

3.1.3   Digitizer

For digital data-processing, the signals are discretized with an Acqiris DC440 analog-to-digital converter (ADC) card. This card provides a resolution of 12 bit with possible voltage ranges from $\pm 125\,\text{mV}$ to $\pm 5\,\text{V}$. The range used in most experiments in this work is $\pm 1\,\text{V}$. The sampling frequency is $400\,\text{MHz}$, which corresponds to a time resolution of $2.5\,\text{ns}$. The measurement process is triggered by a high/low pulse of $2.1\,\mu\text{s}$ length from the DTG. In order to avoid jitter and phase drifts, the digitizer card and the DTG creating the control pulses use an external Rb-reference (see App. A.4.5) signal for synchronization. This setup is displayed in Fig. 3.5.

Figure 3.5: Test setup: *Digitizer*.

3.1.4   Complete setup

Figure 3.6 shows the complete experimental setup of the dual-path receiver relevant for this work. Most of the symbols are self-explanatory, but some may look uncommon to the reader and therefore are given in Tab. 3.1 (complete list in App. A).

Symbol	Description
M-M , F-F	SMA adapter (male to male, female to female, see App. A.1.7).
SMA 2BNC	SMA to BNC adapter (see App. A.1.7).
EL302RT	Laboratory power supply (see App. A.4.2).
TD 2m, MB 7"	Microwave cable. The label codes the manufacturer and length in meter and inches, respectively (see App. A.1.8). <u>Note</u>: Only blue lines are cables, black lines indicate direct connections.

Table 3.1: Description of uncommon symbols in Fig. 3.6.
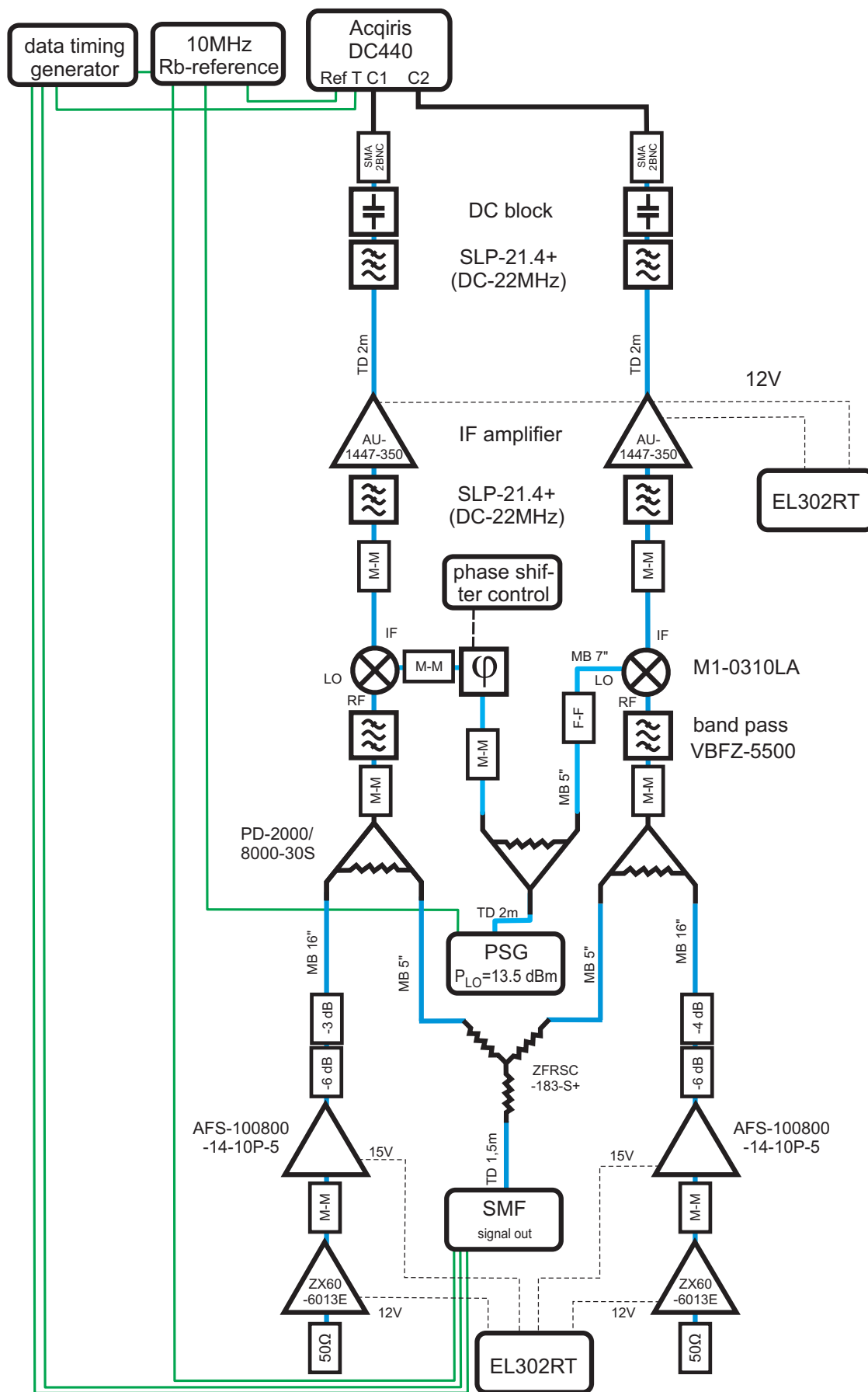
Figure 3.6: Block diagram of the complete experimental setup.

3.1.5   Timing

In this subsection, the timing of the signal generation and measurement is discussed. In order to be able to apply statistical signal recovery methods, an ensemble of *identical* measurements has to be prepared. For an ideal sinusoidal signal without noise this means that not only the amplitude, but also the phase has to coincide for every realization of the measurement. In the remainder of this work, realizations are called traces and points inside the traces are called samples (see Fig. 3.7). Averaging is done for every sample over all recorded traces, so in the end a single averaged trace for every signal or quadrature moment is obtained.
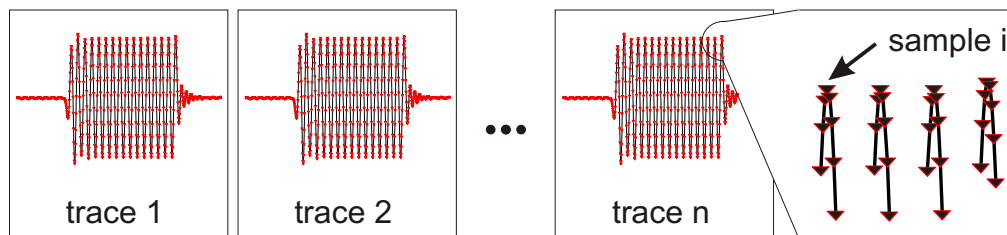
Figure 3.7: In the measurements averaging over an ensemble of traces is done, where each trace has a length of 2.1 µs, corresponding to 840 data points. After averaging a single trace with 840 data points is obtained for every measured quadrature or signal moment.

Although the trace length is 2.1 µs, only every 20 µs a new trace is recorded. This is due to the time required to potentially adjust the phase of the source signal (see section 4.1.6) for the generation of statistical mixtures. Within the measurement window of 2.1 µs, a signal pulse of 1 µs is generated. The trigger-signals required to control the digitizer and the signal source are generated by a data timing generator. Figure 3.8 and 3.9 show the corresponding signals and their levels. During the high time of the *measurement*-trigger a trace such as the one shown in Fig. 3.7 is generated. This gives a lower bound for the measurement time. For example, a measurement with 10 million traces at least takes 3 min and 20 s. It has to be noted that the frequency of measurement ($1/20$ µs) and the IF frequency have to be commensurable. If this is not the case ensemble-averaging will annihilate the signal.
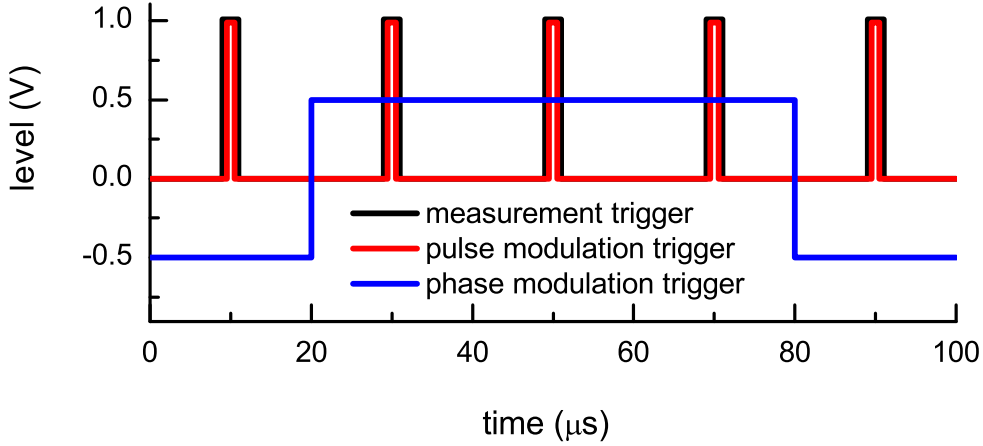
Figure 3.8: High and low time of triggers generated by the data timing generator.
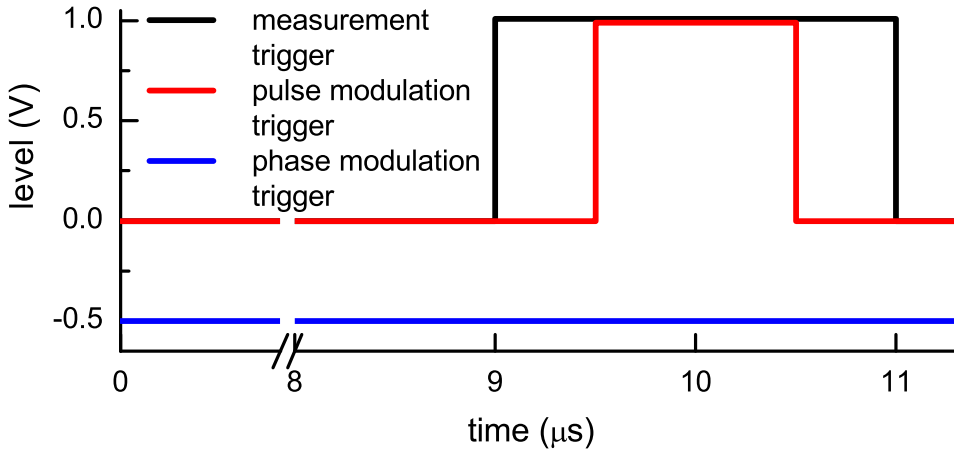
Figure 3.9: Detail view on trigger levels for one measurement period. The second half of the period (12-20 μs) is not shown, because all triggers are in the low state there.

3.1.6   Dual-path calibration

In the theory presented in Ch. 2, both chains have equal characteristics and therefore signals traveling through the arms of the receiver will arrive at the digitizer at the exact same phase ϕ and have the same amplitude A. This is not true for a real experiment, because two microwave components (amplifiers, mixers, cables, ...) will never have exactly the same parameters (gain/loss, length, ...). In the dual-path receiver, the phase difference $\Delta\phi$ originating from different cable lengths is compensated by a computer controlled, motorized phase shifter (see Sec. A.1.6). The difference in amplitude ΔA is compensated by introducing a *balance factor* which is multiplied with every point of channel 1. This is illustrated in Fig. 3.10. To programmatically determine the balance-factor and adjust the phase, a LabVIEW routine has been written, whose flow diagram is shown in Fig. 3.11. The calibration routine runs in a loop until the phase difference reached is below a certain limit and

the relative change of the balance factor is less than a given parameter. At most 10 loop-repetitions are done to avoid infinite loops. The stop-criteria can be set in the LabVIEW interface. In practice, the balance factor is determined within the first loop repetition and does not change significantly thereafter. With respect to the phase difference, values of 0.2° can be reached within 10 repetitions.
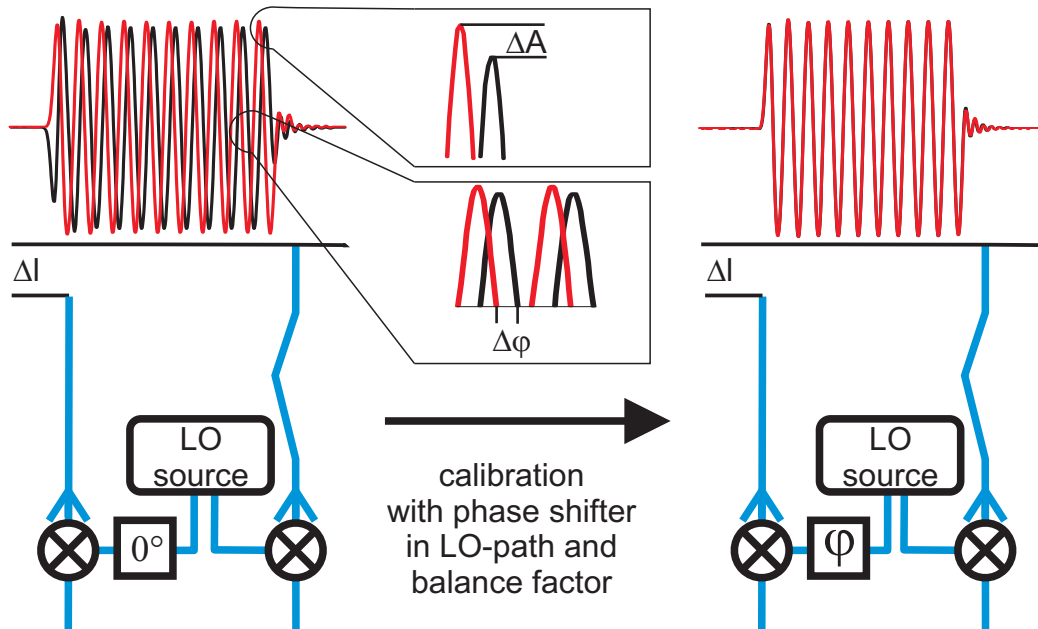
Figure 3.10: Calibration: Phase shift $\Delta\phi$ (mainly caused by differences of electrical length Δl) and differences in amplitude ΔA are compensated by a phase shifter in the LO-arm and by introducing a balance factor, respectively.
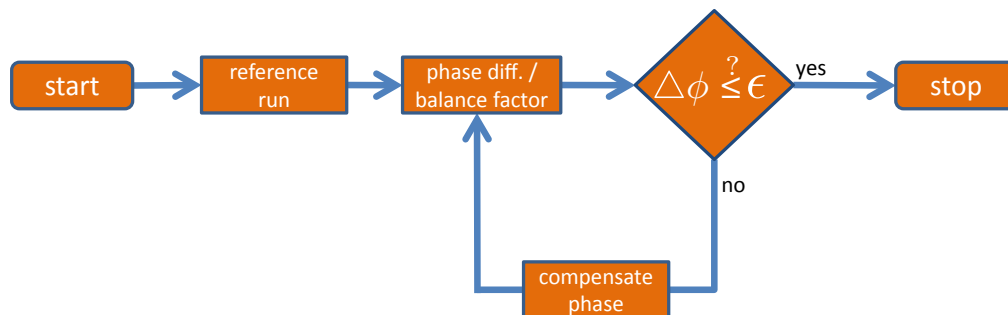
Figure 3.11: Program flow of LabVIEW calibration routine for automatically determine phase shifter position and balance factor.

3.2   Software

The setup described in section 3.1 produces a set of discretized waveforms. Since the Acqiris card can store at most 8×10^6 samples per channel, after approximately 8000

traces the data has to be transferred to a computer for further processing. A software developed by E. P. Menzel was available in version 8 at the beginning of this work. This version has been extended during this work and the version number raised to 9. In this section, the requirements for this software and its implementation, including an integration into the existing LabVIEW environment is described. Furthermore, a simulation software based on the measurement software will be introduced.

3.2.1   Measurement software

In table 3.2, a list of requirements for the measurement software and a comparison of the versions at the beginning and at the end of this work can be found. In this section, first an overview of the program flow is given and then the data processing and how the software satisfies each of the requirements is explained in detail.

Description	version 8	version 9
Data retrieval from Acqiris card	yes	optimized
Calculation and averaging of moments	signal only	signal and IQ
Digital single channel IQ-calculation	no	yes
Data export	yes	yes
Save and reuse raw data	save	save and reuse
LabVIEW integration	yes	user interface simplified
Command line version	no	yes
Performance	acceptable	improved

Table 3.2: Software requirements and achievements in different versions.

Program flow

After the program is invoked, either by LabVIEW or from the command line, it starts a loop which retrieves a predefined number of datasets from the Acqiris card and processes them. The processing step inside this loop corrects for offsets of the captured signal traces (low frequency drifts), calculates quadrature moments by single channel digital homodyning up to a desired order and sums up the results for every point in time. When the loop is left after a predefined number of repetitions a mean value for each quadrature moment at every point of time is calculated and the obtained data is written into a data-file. In Fig. 3.12, a flow chart for the measurement process is shown.

Data retrieval

Since the memory of the Acqiris card is limited to store 8×10^6 samples of data for each channel and in the experiment up to several million of signal traces, each consisting of 840 samples, have to be analyzed, it is necessary to retrieve the data in a number of cycles. This itself is a two-step process: First, the data acquisition has to be triggered and then the data has to be transferred from the device memory of the
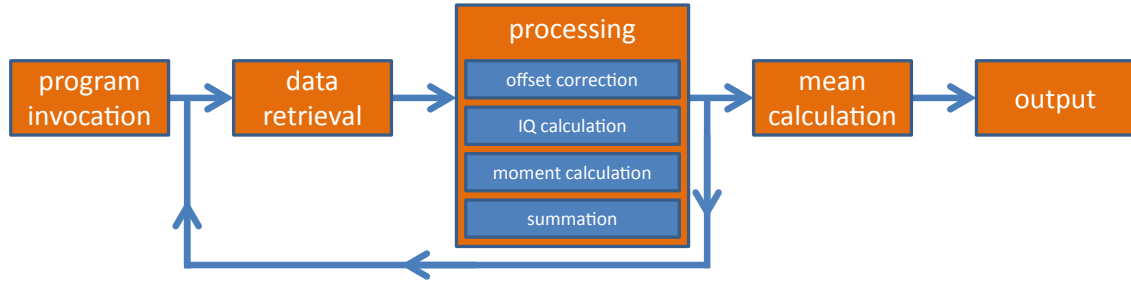
Figure 3.12: A flowchart for the measurement process as implemented in the measurement software. Parallelization is not considered in this scheme.

Acqiris card to the PC. One major improvement of version 9 of the measurement-software is the change from a monolithic form, in which data processing completely stopped while acquiring and transferring new data, to a threaded non-blocking version. This means that data-processing is continued while new data is read from the device and implies faster measurements for a given number of traces.

Calculation and averaging of moments

For every point of time in every captured signal-trace all statistical moments up to a given order have to be calculated. In the end, the recorded traces are averaged and an ensemble averaged trace is obtained. For a single arm, this can be expressed as

$$\langle C_1^j(t) \rangle = \frac{1}{N} \sum_{i=1}^{N} C_{1,i}^j(t), \tag{3.1}$$

where N is the ensemble size. Unfortunately, the number of traces required for reducing the noise to a given level by averaging grows strongly for higher moments. Furthermore, the number of products $\langle C_1^l C_2^m \rangle$ to be calculated and averaged in the case of two arms increases for higher moments. This results in a requirement for significant computing power. For IQ measurements, combinations of signal quadrature moments $\langle I_1^l Q_1^m I_2^r Q_2^s \rangle$ up to the desired moment order have to be computed. For analyzing moments up to order n the number of IQ-combinations L is given by:

$$L = \sum_{i=1}^{n} \binom{i+k-1}{i}. \tag{3.2}$$

where $k = 4$ because two quadratures per arm must be considered. For example, using moments up to 4th order requires 69 IQ-combinations. Calculating the complex envelope is not implemented in the measurement software because this can conveniently be done after averaging.

Digital single channel IQ-calculation

An implementation of the single channel digital homodyne (see section 2.4) has been added in version 9. Due to the numerical integration involved in digital homodyning,

this is the most demanding task in terms of computation power in the measurement program. Therefore, some effort has been invested in implementing a Streaming SIMD Extensions (SSE, [41]) version of the calculations. However, it turned out that single precision is not sufficient for these calculations and SSE commands using double precision did not bring a significant advantage in computation time. Instead, a runtime parameter has been established that allows to evaluate the integral only at every nth point and using the last calculated integration value for the points in between.

Data export
All results are saved to an ASCII file and can therefore easily be imported into any desired program for further processing and analysis.

Save and reuse raw data
In contrast to version 8, version 9 allows for reusing previously saved raw (not averaged) data to redo the moment calculations. This is especially useful for debugging and for the analysis of special input data which cannot be generated with the simulation tool [42], e.g., bandwidth limited noise (see Sec. 4.3.1).

LabVIEW integration
Already version 8 was integrated in the LabVIEW measurement-environment used at WMI. In version 9, some unused settings where removed and others concerning IQ-calculation where added.

Command line version
A command line version of the measurement software has been implemented, which also serves as the code-base for the simulation tool. The command line version is controlled via a parameter file.

Performance
Besides the integration of IQ-calculations via single channel digital homodyning, the second main task for the enhancement of the measurement software was to improve performance. Version 8 sequentially performed the following tasks for a desired number of repetitions: invoke the data retrieval, wait for completion of the latter, transfer the memory contents, and process the data.

This procedure can be considerably enhanced by doing calculations during the memory transfer and by exploiting the multicore architecture of modern CPUs. Therefore, the measurement program has been redesigned to use threads. As a consequence, it is now capable of using multiple CPU-cores and can process part of the current data set while the next one is transferred to the PC. The essential idea is to introduce one *datareader-thread* and several *worker-threads*. Figure 3.13 shows a visualization of the invocation of one datareader-thread and multiple worker-threads

on a multi-core CPU. The mapping of the threads to the CPU-cores is not shown, but under experimental conditions this configuration almost uses 100% of CPU time.
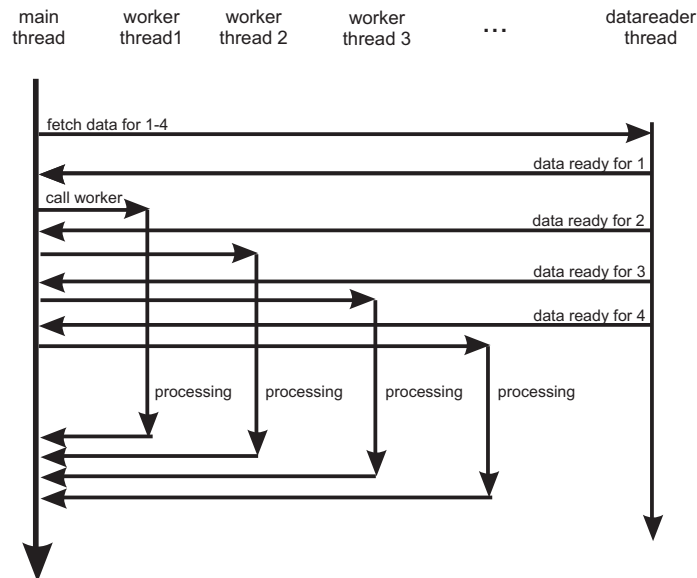
Figure 3.13: The *dataread-thread* fetches data from the Acqiris card and passes it to worker threads. While data is processed by the *worker-threads* new data can be fetched. When processing is finished the worker threads report this to the *main-thread* and new data is passed from the *datareader-thread*.

Figure 3.14 shows a performance comparison of version 8 and version 9 for calculating signal moments up to the 4th moment, with and without IQ-calculations, for different numbers of traces. Three main features are observed: First, there is a clear performance gain in version 9 with respect to version 8 when digital homodyning is turned off. Second, the performance of Version 9 is clearly limited by the digital homodyning procedure. Finally, both version 8 and version 9 cannot provide realtime data processing. For this purpose an analog-digital converter (ADC) board with an integrated field programmable gate array (FPGA) logic is required (see Sec. A.3.2). Realtime measurements would yield a significant performance gain, as can be seen in Fig. 3.14. For realtime measurements taken at a rate of $50 \cdot 10^3$ traces/s speedup of factor 8.5 is gained. But as most experiments allow for higher rates, much higher speedups can be realized, e.g. at rate of $1 \cdot 10^6$ traces/s a speedup-factor of 172 can be reached.

3.2.2 Simulation of measurements

Based on the measurement program, a program simulating the dual-path receiver has been written by Philipp Summer during his bachelor thesis in supervision of the author of this thesis. It is used to make predictions on effects of different bit-resolutions, ensemble sizes and rounding methods of the digitizer. Also, different
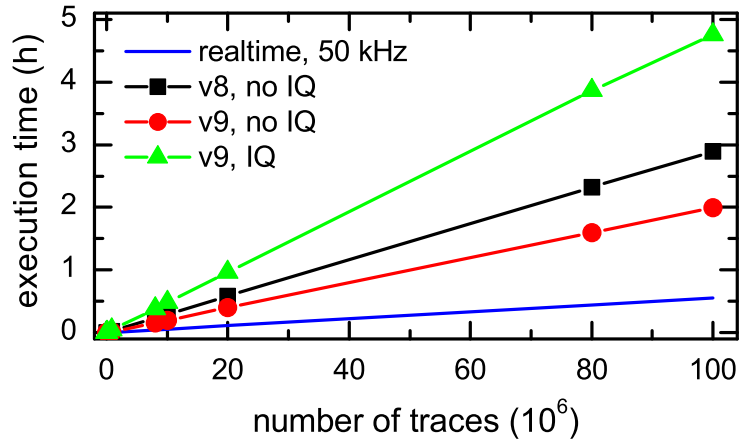
Figure 3.14: Performance of different versions of the measurement program
 compared to a realtime measurement.

signal to noise ratios were studied. For more detailed information regarding these
simulations, the reader is referred to [42].

3.3   Field programmable gate array

As described above, using the Acqiris card for data-retrieval introduces a delay time because after $8 \cdot 10^6$ samples the data has to be transferred to a computer. This transfer takes a significant amount of time and makes realtime measurements impossible (see Fig. 3.14). To overcome this problem, an ADC card equipped with a field programmable gate array (FPGA [43]) is used. A FPGA is capable of doing specific data processing tasks at very high speed since a customized logic can be implemented in its hardware. It is loaded with a user-programmed logic which runs at full clock speed, which in our case is 200 MHz. This allows for realtime data-aquisition at a 5 ns sampling interval. In the case of the dual-path setup, the FPGA records the voltage of the two dual-path chains, calculates signal moments and sums them up continuously. After recording and processing a given number of traces, the summed up moments are transferred to the measurement PC. The communication between the measurement PC and the FPGA card is done by an extended version of the so called *Snap*-tool, delivered by the card manufactor[1].

During this work, the foundations for a TCP/IP based client-server functionality has been added to the *Snap*-tool. In this way, one can have the FPGA-card connected to one PC while controlling it and doing data analysis from another machine (see Fig. 3.15). Within this work, a beta-version of the server and a simple test client have
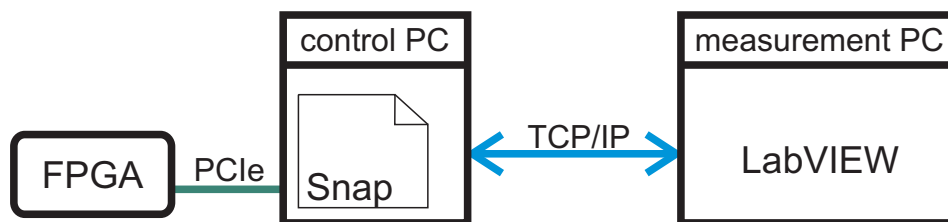
Figure 3.15:   Client-server architecture of the measurement software for realtime measurements with a FPGA card.

been implemented. The client is able to send commands to the server via the network and the servers processes them and gives a reply. By now, simple commands such as reporting the FPGA-status are implemented. Extending the server to full functionality is straightforward. The client is written in LabVIEW using only standard techniques and can be easily integrated into the existing measurement program.

---

[1]FPGA logic programming and improvement of Snap-program have been done by Matthias Ihmig.

Chapter 4

Experimental results

This chapter consists of two parts: Characterization and signal reconstruction. Section 4.1 contains the results of the characterization measurements done to reveal parameters of operation of the dual-path receiver. Section 4.2 deals with the measurement of signal mixtures and compares the results to simulations and to the results of E. P. Menzel [25].

4.1 Characterization

In this section, basic properties of the components of the setup and the dual-path receiver as a whole, such as noise features, linearity in power and phase stability are tested.

4.1.1 Motorized phase shifters

Non-idealities in cable lengths and therefore phase differences in the arms of the dual-path receiver are compensated by phase shifting one of the local oscillator signals (see Sec. 3.1.6). For this purpose, a motorized phase shifter (see App. A.1.6) is used, which has to be characterized with respect to linearity and accuracy. To this end, the complex transmission parameter of the phase shifter is measured with a vector network analyzer (Rohde & Schwarz ZVA24, see App. A.3.4) at a frequency of 5.63 GHz. The analyzer sends a coherent probe signal into the phase shifter and measures the phase shift due to the presence of the phase shifter. This setup is depicted in Fig. 4.1. The test procedure consists of a calibration, a linear and a random test run. The calibration is done by sweeping the range of possible step motor positions while measuring the phase and thus obtaining a mapping of step motor positions to phase shifts. The linearity and the accuracy are tested by plotting the phase measured against the phase set. The phase in one case is increased monotonously, in the other set to random values. A figure of merit for linearity is given by how close the linear fit is to a line with slope 1 and the accuracy by the maximum deviation from this fit. The measurement results are shown in Figs. 4.2-
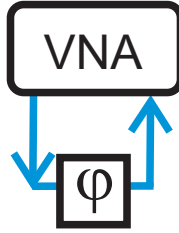
Figure 4.1: Setup for characterization measurements of motorized phase shifters.

4.4. One can see that for linearly increasing phases a maximum deviation of 0.1°occurs. For randomly set phases the deviation raises to 0.5°. This is within the range of linearity needed for measurements. Additionally, uncertainties in setting the phase are smaller than the phase drifts that anyhow are occurring in the system (see Sec. 4.1.7).
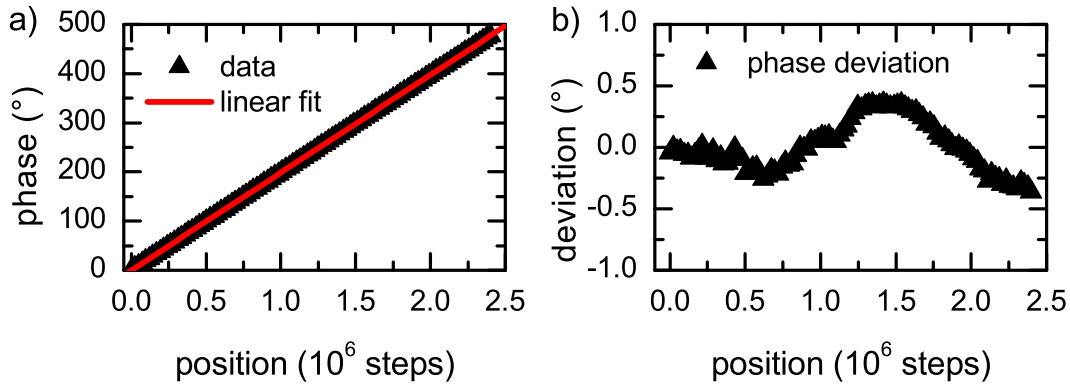
Figure 4.2: Calibration data of the phase shifter. a) Measured phase of motorized phase shifter depending on step motor position. b) Deviation.
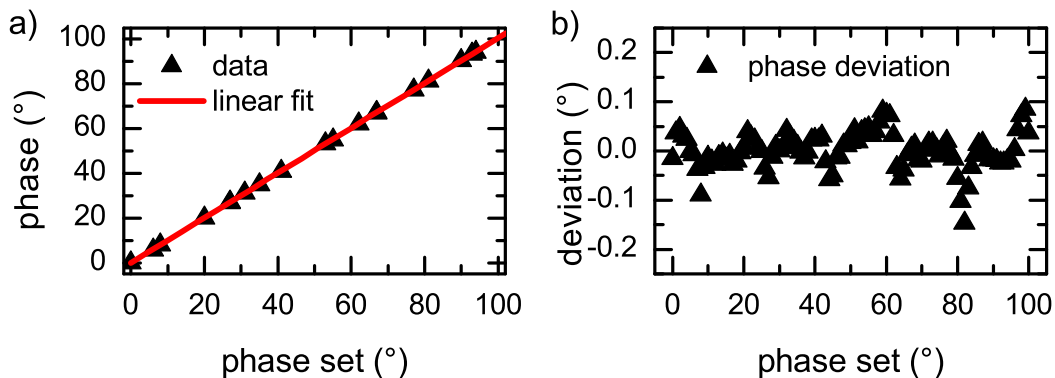
Figure 4.3: Test with monotonously increasing set phase. a) Measured phase of motorized phase shifter (slope of fit 0.999 ± 1.129^{-4}). b) Deviation.
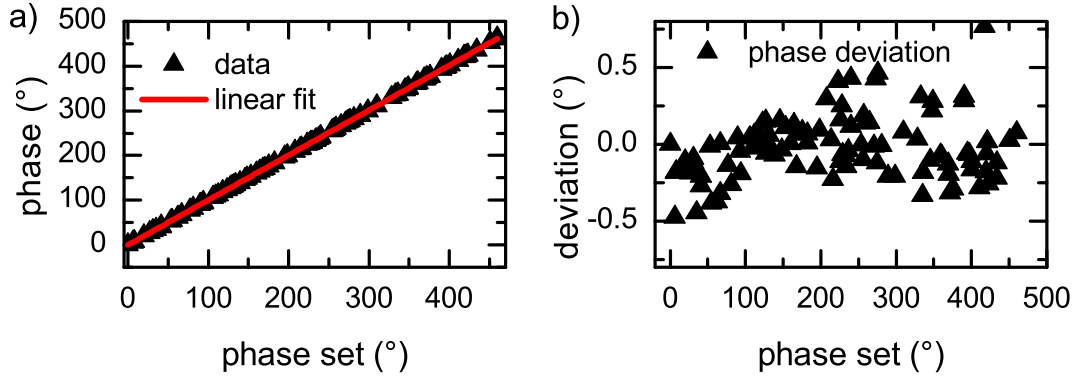
Figure 4.4: Test with random set phase. a) Measured phase of motorized phase shifter (slope of fit 1.004 ± 8.06^{-5}). b) Deviation.

4.1.2 Decorrelation effects

As already mentioned in Sec. 3.1.6, phase differences originating from different cable lengths in the two arms of the dual-path setup are compensated by using a phase shifter in one of the LO-paths. The main source of phase differences are differences in the electrical length of the RF-paths. These effects are studied in the following by inserting additional cable lengths into one of the RF-paths. Although inserting a phase shifter is equivalent to inserting small cable lengths < 0.5 m, microwave cables of a length of 0.5 to 10 m are investigated (see Fig. 4.5a). In a second step, cables are also inserted into the IF path (see Fig. 4.5b). In this setup, a noise signal which
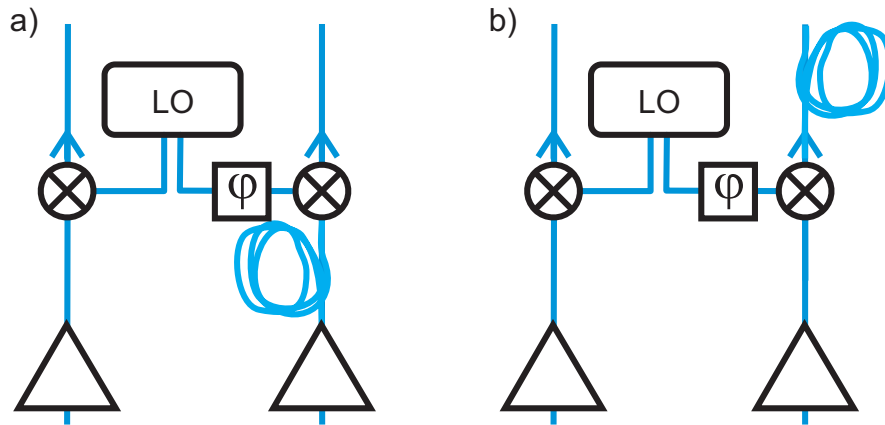
Figure 4.5: By inserting microwave cables of different lengths in one arm of the setup, decorrelation effects are studied. In (a) cables are inserted into the RF-path, in (b) into the IF-path.

is white within a bandwidth of $B = 80$ MHz is generated, split and sent through both chains, where the signal in one chain is delayed by inserting a cable of a certain length. We then measure the correlation factor

$$g_c(\tau) = \frac{\langle C_1 C_2 \rangle|_\tau}{\sqrt{\langle C_1^2 \rangle \langle C_2^2 \rangle}|_{\tau=0}} \quad , \tag{4.1}$$

which is defined as the ratio between the cross correlations at time τ and the square root of the autocorrelations at $\tau = 0$. The time τ relates to the cable length via the propagation delay of $4.56\,\text{ns/m}$ in the inserted cables (Teledyne Reynolds True blue 205, see App. A.1.8). As the signal is filtered with a cutoff-frequency of approximately $20\,\text{MHz}$, one expects to see a correlation-function of band limited white noise [44]

$$ g_\text{c}(\tau) \propto \frac{\sin\left(W\tau/2\right)}{W\tau/2}\cos\left(\omega_0\tau\right) \quad , \tag{4.2} $$

where $\omega_0 \equiv 2\pi f_0$ is the band center and W is the bandwidth of the noise signal. g_c is expected to be independent of the selected RF and IF-frequencies as long as the center frequency f_0 of the noise in RF is close enough to the LO-frequency to give a noise band in IF that is broader than $20\,\text{MHz}$, which is always the case for the measurements shown in this section.

In Figs. 4.6-4.8 the correlation factor g_c is plotted. For $\tau = 0$, the value of g_c is 0.997, which indicates nearly perfect correlation, thus no decorrelation effects are caused by the receiver. Figure 4.6 exactly shows the expected behavior for the
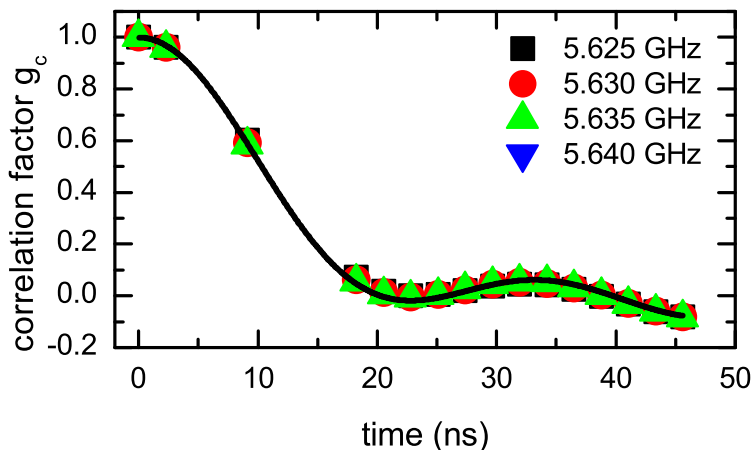
Figure 4.6: Effect of inserting cables of different length into one IF-path (see Fig. 4.5b). Measurements at different LO-frequencies give the same results. The black line is a fit of Eq. (4.2) to the data.

case of inserting cables of different lengths after one of the IF-amplifiers. The same modulated cardinal sine function is observed for every chosen LO-frequency. Figure 4.7 shows the same measurements, but this time cables have been inserted into the RF-path. A clear dependence on the LO-frequency is observed in these experiments. This behavior could not be explained by a theoretical model yet. However, Fig. 4.8 shows that we can exclude a dependence of the modulation on the noise source or the frequency at which the setup was calibrated (adjustment of LO-phase and determination of balance factor, see Sec. 3.1.6).

 Although the above effects were not completely clarified, two important conclusions can be drawn. First, as the expected cardinal sine is observed, the calibration routine works well enough to preserve correlation effects for two chains of different length.
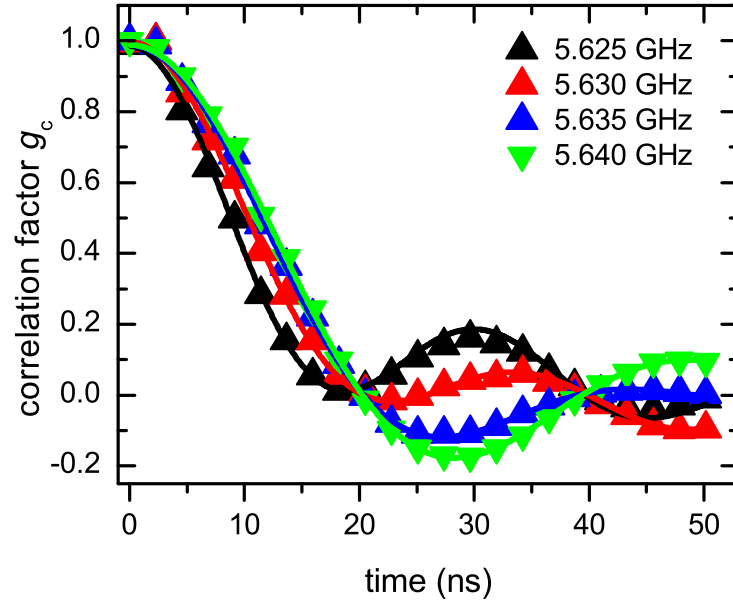
Figure 4.7: Effect of inserting cables of different length into one RF-path (see Fig. 4.5a). Measurements at different LO-frequencies do no longer coincide as in Fig. 4.6. The setup is calibrated with a coherent probe signal (IF-frequency $=10\,\mathrm{MHz}$) at each cable length. The colored lines are fits of Eq. (4.2) to the data.
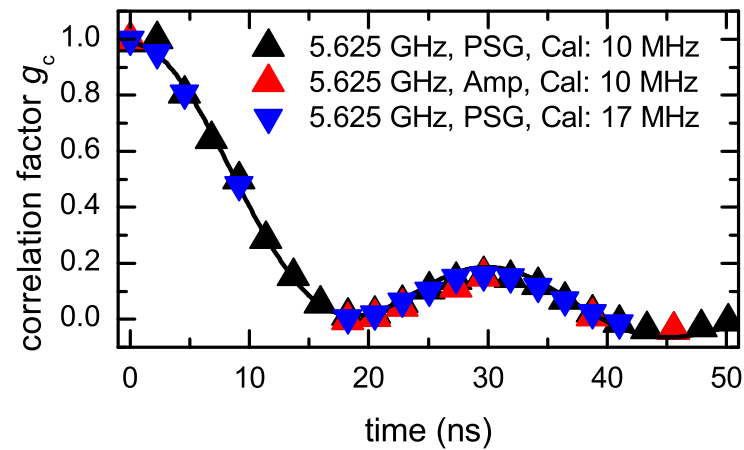

Figure 4.8: g_c for band-limited noise generated by a microwave source (PSG) and the amplified signal from a $50\,\Omega$ terminator as noise sources (Amp) can be seen. 'Cal' denotes the IF frequency at which the setup is calibrated. The black line is a fit of Eq. (4.2) to the data.

Second, for the practically relevant case of RF-paths differing in length by less that $0.5\,\mathrm{m}$, the correlations are very well preserved.

4.1.3   Noise sources

As one wants to measure with high accuracy, diminishing noise contributions is an important task. In particular correlated noise occurring in both channels presents a problem, because the dual-path method is based on statistical independence of the noise sources. Two main sources of noise have been found:

- Noise from the power supply & control unit of the step motor in the phase shifter

- Noise originating in the digitizer card

The first noise source can be overcome by adapting the setup. But the noise originating from the digitizer card is an intrinsic feature of the specific card and will not change unless another digitizer card is used.

Power supply & step motor controller

The motorized phase shifter is operated by a DR12024 (App. A.4.2) as a power supply, which has turned out to be a significant source of noise. Thus it has been replaced by an EL302RT (App. A.4.2) power supply. Figure 4.9 shows a comparison of the spectra of the dual-path receiver using DR12024, EL302RT and with power supplies unplugged. The right plot shows a regime from 0 to 500 kHz, the left shows a frequency range from 0 to 40 MHz. It can be clearly seen that the DR12024 power
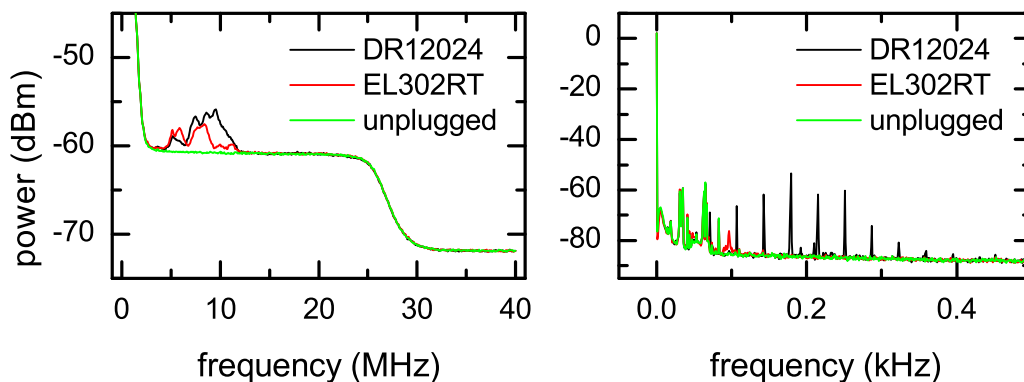
Figure 4.9: Spectra showing noise features using two different and no power supplies at all in different frequency ranges.

supply gives a lot of unwanted noise features, whereas the EL302RT has much less, but still is not perfect. The measurements are taken with RF power turned off, using a Rohde & Schwarz FSV spectrum analyzer (see App. A.3.3).

After minimizing the noise contributions from the power supply the measurement method is changed to doing Fourier transforms of traces captured with the measurement program. These traces are thus averaged and reveal correlated noise contributions in the cross moments. Investigations show that the step motor controller is a considerable source of correlated noise. Figure 4.10 shows a Fourier transform of

an average trace taken with the power of the step motor controller turned on and off. To handle the problem of this noise source a computer programmable switch (see App. A.4.4) is used to cut galvanic connections from the step motor controller to the step motor while measurements are running. This also solves the problem of noise from the power supply completely.
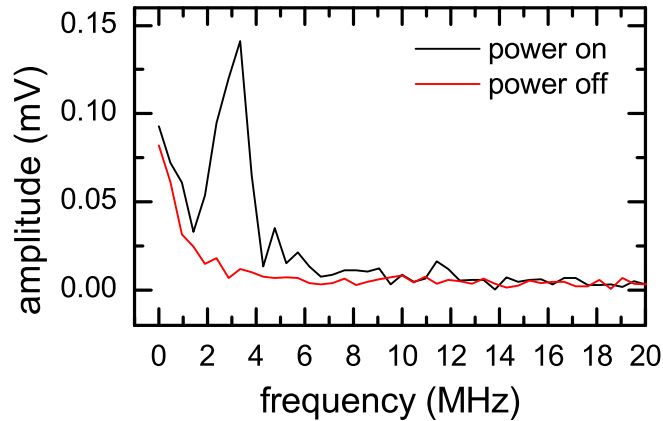
Figure 4.10: Fourier transform of an average signal trace (1st moment) with step motor controller on (black) or off (red).

Digitizer noise

It has been seen that there are two intrinsic noise components in the digitizer card. To measure these components, the digitizer card inputs have been terminated by means of 50 Ω-terminators (see Fig. 4.11).
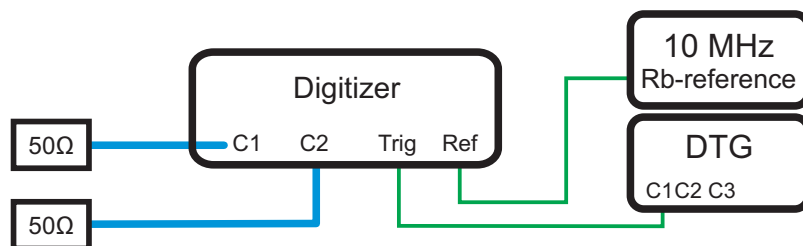
Figure 4.11: Setup for testing digitizer noise. The inputs of the digitizer are terminated by 50 Ω so only noise generated by the digitizer itself is captured.

Figure 4.12 shows that signal components at 10, 25, 50, 75 MHz, ... are always present, although the digitizer inputs are terminated. It also can be seen that the noise contributions in channel 2 are significantly higher than in channel 1. In addition to the peaks at the above mentioned frequencies, the digitizer noise also increases during the high-times of the measurement-trigger and decreases during low-times. Figure 4.13 shows these trends for different DTG timing settings and clearly
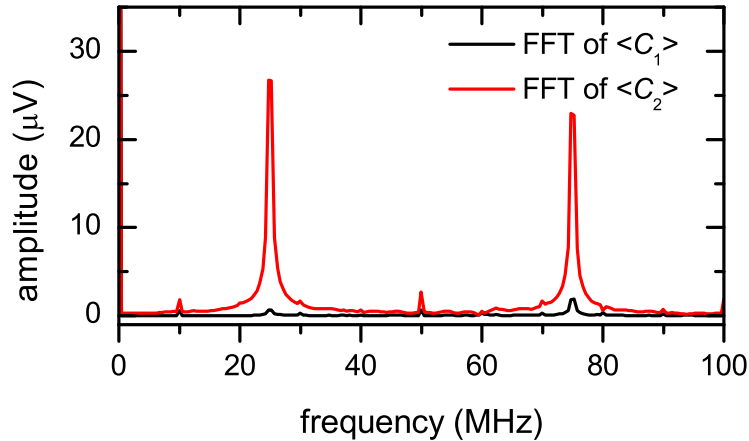
Figure 4.12: Fourier transform of an averaged 2.1µs (840 points) trace
for digitizer channels one (black) and two (red). A significant difference
between the to input channels can be recognized.

identifies the trigger signal as the source of this noise contribution. Obviously, the
trigger cannot be turned off to solve this problem. The red lines in Fig 4.13 show
the increasing and decreasing trend for a 20 µs DTG-period. As in the experiment
only during the first 2.1 µs of every 20 µs a measurement is done, only the increasing
trend is added to the measured signals and can be seen in measurements at very low
power.
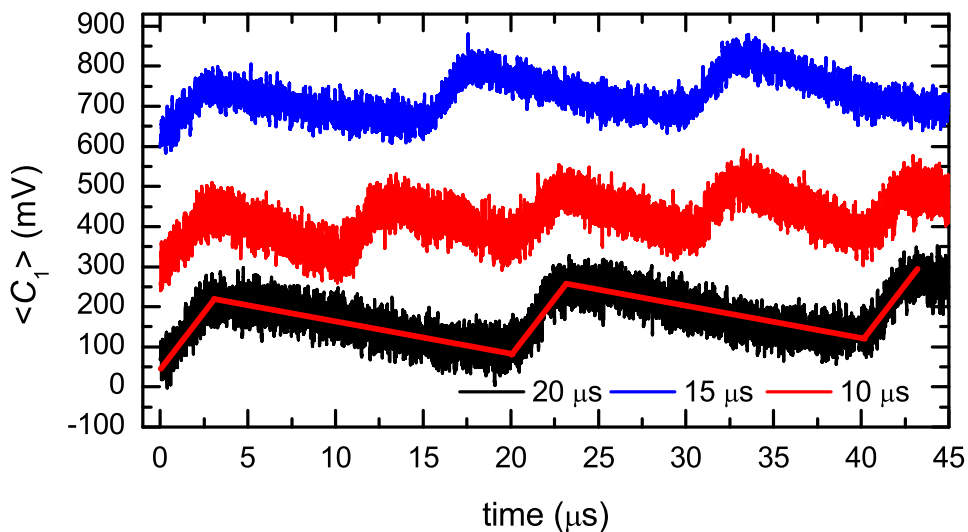
Figure 4.13: The acquiris digitizer shows a periodic noise signal clearly
correlated to the measurement trigger. Three different periods for the
measurement trigger are shown: 20 µs (black), 15 µs (blue, with an offset
of 600mV) and 10 µs (red, with an offset of 300mV). The noise signal is
increasing while the measurement trigger is high and is decreasing while
it is low. The red line is a guide to the eye illustrating this trend.

4.1.4   Additional filters

The heterodyne converter shown in Fig. 3.4 contains a 20 MHz low-pass filter in front of the IF-amplifier in each chain. Its purpose is to reduce the overall power sent to the IF-amplifier and to prevent the amplifier from showing compression effects already at low powers. This, in turn, expands the region of linearity of the dual-path receiver. The two low-pass filters, marked red in Fig. 4.14, have not been present in the original receiver, so their influence on the overall setup has to be tested.

Figure 4.15 shows that the additional filters delay the signal, but do not qualitatively
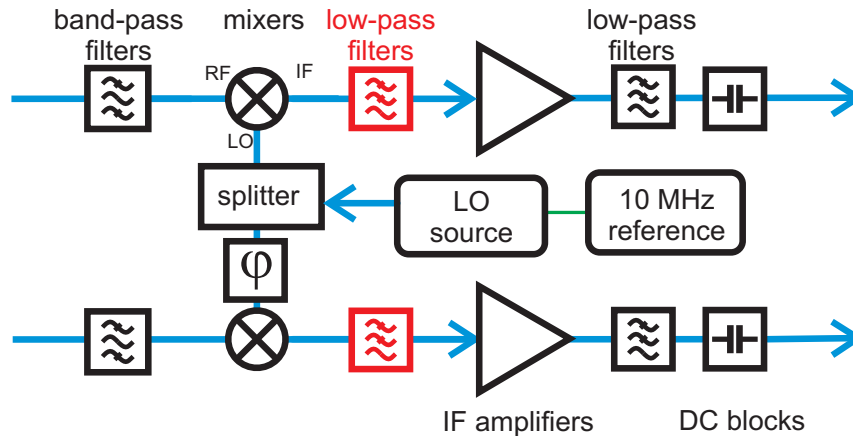
Figure 4.14: *Heterodyne converter*-part of test setup, filters in front of IF-amplifiers are marked red.

change it. The test signal is at 5.63 GHz, resulting in a down-converted signal of 10 MHz. Figure 4.16 shows the spectra of white noise and a sine signal, respectively,
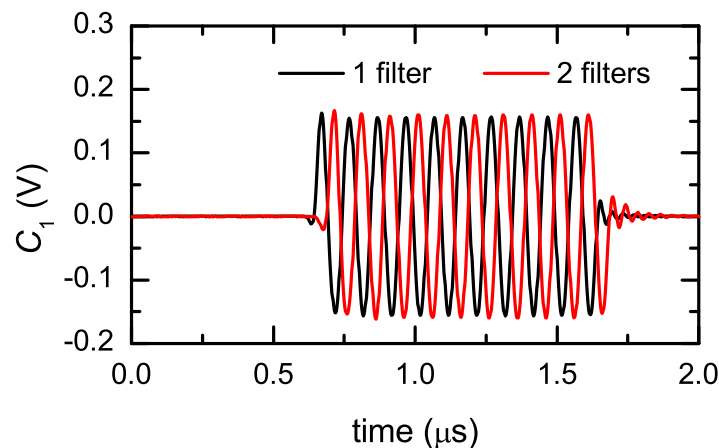
Figure 4.15: Averaged signal trace without (black line) and with the additional filter mounted (red line).

fed into the receiver with and without the additional filters. It can be seen that the spectra are not changed by the additional filters in the frequency range of interest (< 20 MHz). Only the filter-slope gets steeper and hence the cutoff is sharper. Following

[45], an equivalent noise bandwidth can be derived for the two filter configuration of Fig. 4.16. The equivalent noise bandwidth gives the cutoff frequency of a perfect, rectangular shaped, filter, having the same integral-area in the power-spectra as the physical filter. Having this single number, it is much easier to estimate the transmitted power like it is done in section 4.1.8. Mathematically, the equivalent noise bandwidth B_N is defined as:

$$B_N = \frac{1}{H_0^2} \cdot \int_0^\infty H_V^2(f) df, \tag{4.3}$$

where $H_V(f)$ is the voltage-transmission-function and H_0 is the voltage-transmission-function at the center frequency of the filter pass-band. Using this method, the equivalent noise bandwidths become $B_{N,1 \text{ filter}} = 24.3\,\text{MHz}$ for a single filter and $B_{N,2 \text{ filters}} = 23.8\,\text{MHz}$ for two filters.
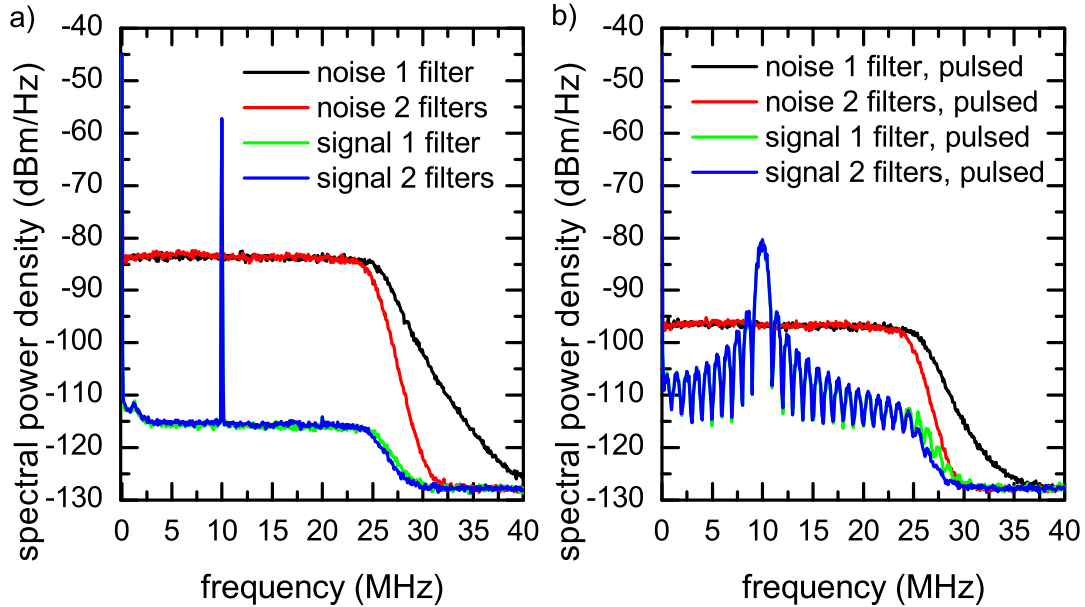
Figure 4.16: Spectra of continuous wave (a) and pulsed signal (b). Spectra were taken for a sine and a noise signal with and without additional filters.

4.1.5 Jitter

A signal showing slight deviations from ideal periodicity is said to have *jitter*. In case of the dual-path receiver, this means a deviation in time of the start of a recorded pulse or, equivalently, of the peaks of a signal. To characterize the jitter, a rectangular pulse was generated and measured directly with the acquiris card ten million times. The pulse shows overshoot, thus has a peak at its start which, for each trace, should be at the same point of time when no jitter occurs (see Fig. 4.17). Figure 4.18 shows histograms of peak positions for different synchronization methods of the digitizer card. The histogram in Fig. 4.18a clearly shows that jitter appears when using the digitizer's internal reference. Looking at Fig. 4.18b, the histogram
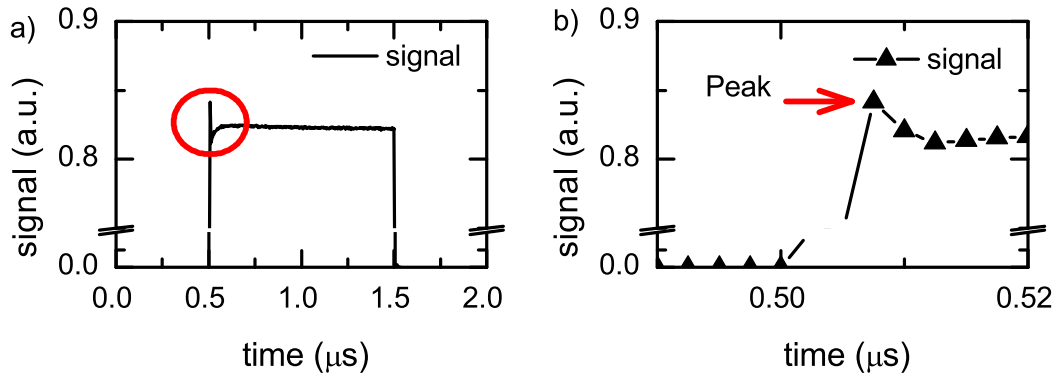
Figure 4.17: a) A rectangular pulse is generated to test if the signal starts at the same point in time in every recorded trace. b) Detail view of the peak structure.

only has one bin, meaning that no jitter occurs when using the external Rb-reference (A.4.5). This result strongly backs up the decision to make the effort of using an external reference for synchronization.
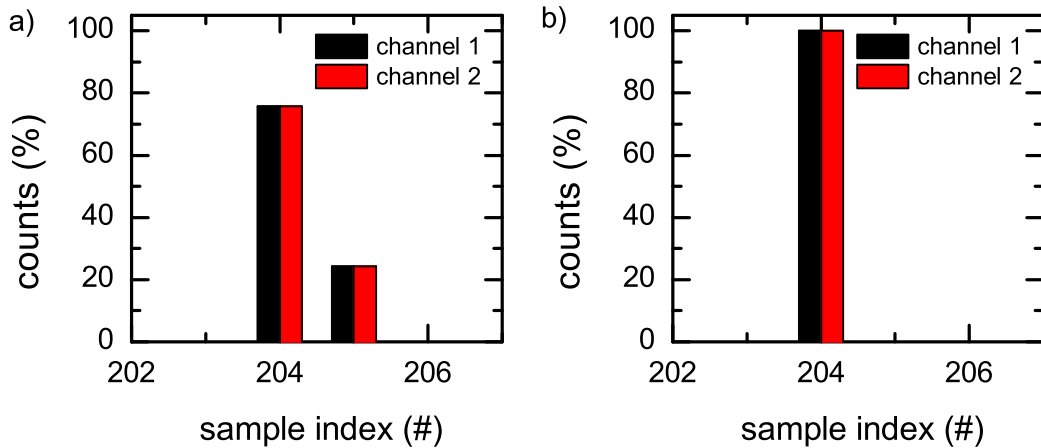

Figure 4.18: Histogram of: a) Pulse start index using the internal reference. b) Pulse start index using the external Rubidium reference (see App. A.4.5).

4.1.6 Phase modulation time

For some experiments it is necessary to set the phase of the signal differently for every trace or at least for some of them (see Sec. 4.2.2). Adjustment and stabilization of the phase takes the microwave source some time and this time limits the speed at which pulses can be generated. The microwave source used in the experiment (SMF, see A.2.1) offers three modes for phase adjustments:

- high bandwidth

- high deviation

- low noise

The task is to verify if the actual measurement period is chosen correctly and to find out which option sets the phase fastest. A signal trace of $40\,\mu s$ length has been recorded. After $20\,\mu s$ from the start of the trace a phase shift of $360°$ is triggered. To determine the point in time at which the phase shift is done and the signal is stable again, the signal in the first period is fitted to a perfect sine. This fit is extrapolated over the whole time of $40\,\mu s$. At the point of time where the measured signal and the extrapolated fit coincide again, the phase shift is finished. Figure 4.19 shows this for the *high deviation* option of the SMF, which is used in the measurements in this work. In App. B.2 data for the other two options can be found. According to this data, it would be possible to shorten the measurement time by using e.g. the *high bandwidth*-mode instead of *high deviation*. Table 4.1 shows the times needed to adjust the phase for each option. As shown in Fig. 3.8, every $20\,\mu s$ a trace is recorded. The trigger for the start of the measurement is fired $9\,\mu s$, the trigger for the signal pulse $9.5\,\mu s$ after the trigger for phase adjustment. This means phase adjustment has to be done within $9.5\,\mu s$ and this is achieved. It would be possible to shorten the interval of measurements by using another option, but since such phase modulation is only relevant for characterization and proof of principle measurements, it is not critical for real experiments to gain speed on that. The important result here is that the measurement period of $20\,\mu s$ used in the present thesis and also in previous experiments was chosen correctly and can safely be used.

option	adjustment time
high deviation	$8.90\,\mu s$
high bandwidth	$3.65\,\mu s$
low noise	$6.80\,\mu s$

Table 4.1: Time needed for phase adjustments of $360°$ when using different SMF options.
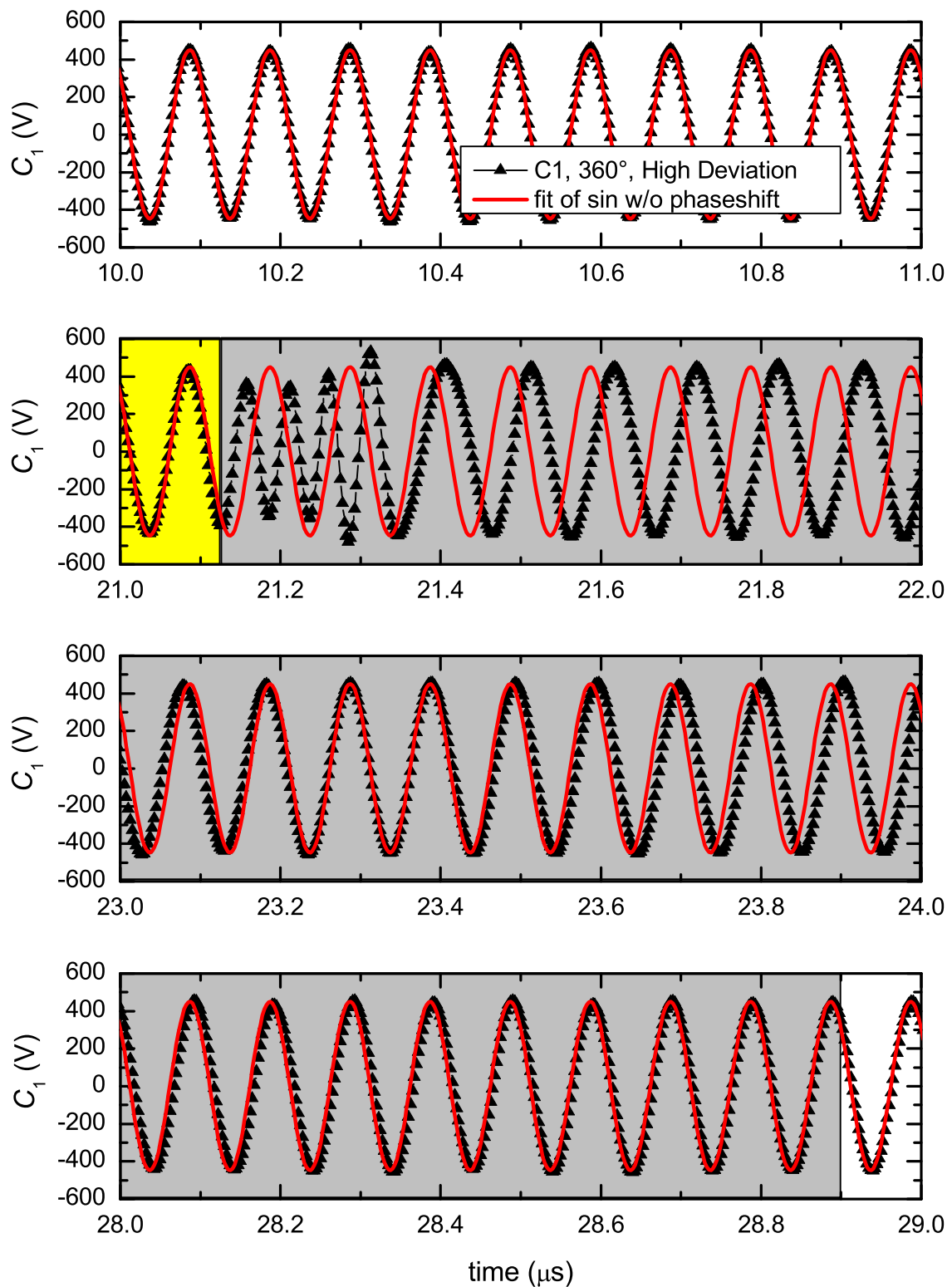
Figure 4.19: Timetrace of SMF output for a phase shift of 360° in *HighDe-viation* mode (black) compared to a fit of the signal before triggering the phase shift (red). The gray shaded area marks the region in time in which phase adjustment is in progress. The yellow area indicates the time in which the trigger already is fired, but the phase adjustment process has not started.

4.1.7 Phase stability

Due to the large number of traces required for dual-path measurements, the measurement time can be rather long. It is not clear in advance that the phase difference of signals generated by microwave sources for the probe signal and the local oscillator, like the SMF, is stable, even if these sources are phase locked to the same 10 MHz reference. Phase stability is important, not only for proof of concept and characterization measurements, but also for real measurements (e.g., a JPA needs a microwave source driving it), thus it is investigated. The dual-path receiver is tested on phase stability as a black box device, meaning that sources of phase deviation cannot be identified. A set of 32 segments, each containing 8192 traces, is recorded. After measurement of each of these 32 segments a delay of 1 minute was kept, which leads to a 31 minutes investigation period. For every trace in every segment amplitude and phase have been analyzed by a sinusoidal fit. The time evolution of phase and the overall distribution of phases is investigated by generating one histogram over all traces and an individual one for every segment. Figure 4.20a shows the
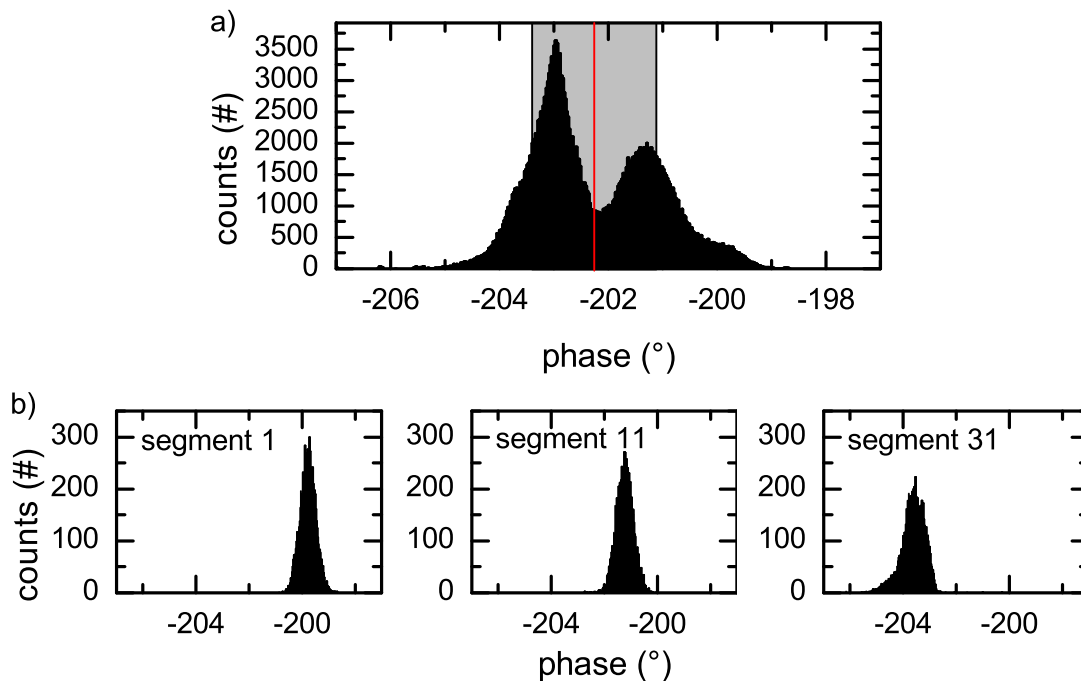
Figure 4.20: a) Histogram of measured phases in all segments. The red line and the gray shaded area mark the mean value $\mu = -202.3°$ and a one sigma vicinity of $\pm 1.14°$. b) Histogram of measured phases in segment 1, 11 and 31. Absolute phase values are arbitrarily referenced, as only the time drift and spread is of interest.

distribution of phase for the whole period, Fig. 4.20b for segment numbers 1, 11 and 31. This means the phase histogram for the first measurement and then after 10 and 30 minutes, respectively. From these measurements it can be seen that the phase drifts in time, with a mean value $\mu = -202.3°$ and a standard deviation $\sigma = 1.1°$

for the whole observation period of 31 minutes. This has to be considered when designing an experiment, because possible negative effects of phase drifts were already observed by E. P. Menzel during his work on JPAs [35].

4.1.8 Linearity

In theory, amplifiers are linear devices, meaning that the gain is constant with input power. In reality, this can only be an approximation for a limited power range. Starting at a certain input power, amplifiers will show compression [46]. For linearity tests the signal emulator part of the dual-path receiver (see Fig. 3.2) is slightly modified. The amplifiers for noise generation are removed and a PSG microwave source is used instead of a SMF (see Fig. 4.21). The PSG is used because it is capable
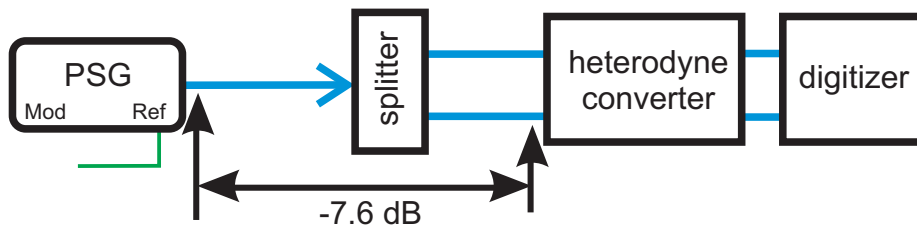
Figure 4.21: Measurement setup for testing linearity of the dual-path receiver. Due to losses in the cable and the splitter, the power level at the receiver input is 7.6 dB lower than at the PSG-output.

of generating band limited white noise. Powers in a range from -100 to -24 dBm for band limited noise (bandwidth $B = 80$ MHz, center frequency $f_0 = 5.64$ GHz) and a sine signal (frequency $f_0 = 5.624$ GHz) were tested. The results and figures already account for the fact that the power level at the receiver input is 7.6 dB lower than at the PSG. Figure 4.22 shows the power dependence of the time and ensemble
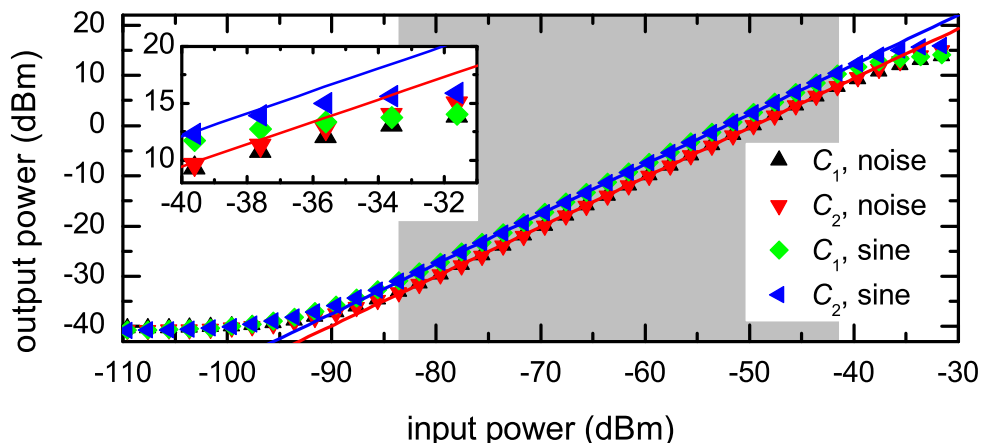
Figure 4.22: Linearity of receiver in power for different input signals. Gray shaded area marks the range of linearity.

averaged rms-power at the digitizer. The setup behaves almost perfectly linear for

input powers from -83.6 up to $-41.6\,\mathrm{dBm}$. For powers lower than $-83.6\,\mathrm{dBm}$, the resolution limit of the dual-path receiver is reached (see Sec. 4.2). For input powers larger than $-41.6\,\mathrm{dBm}$ compression effects of the amplifiers begin to disturb linearity (see Fig. 4.22).

Comparing the 1 dB compression points (for a definition see [45]) in Tab. 4.2, it can be seen that for the case of the sine-signal compression shows up at larger powers as compared to noise as input (see also Fig. 4.23). This is due to the fact that the measured sine-signal has a frequency within the pass-band of the combination of filters used in the setup, and thus no power is filtered by the band-pass and low-pass filters. Further, one can see that channels one and two do not behave exactly equally. This can be attributed to deviations in the specifications of the components used in the two dual-path arms, especially of the amplifiers, even though they are of the same model. Using the results gained in Sec. 4.1.4, where the noise bandwidth was

channel	signal type	1 dB comp. pt.	channel	signal type	1 dB comp. pt.
C_1	sine	$-39.0\,\mathrm{dBm}$	C_2	sine	$-36.6\,\mathrm{dBm}$
C_1	noise	$-38.2\,\mathrm{dBm}$	C_2	noise	$-35.6\,\mathrm{dBm}$

Table 4.2: 1 dB compression points

found to be $B_{\mathrm{N,2\ filters}} = 23.8\,\mathrm{MHz}$ one can estimate the offset between the trace for white noise and for the sine-signal in Fig. 4.22. The power carried in the filtered noise signal should be the fraction $23.8/40$ of the whole power sent by the signal generator, which gives an offset of $2.3\,\mathrm{dB}$. As the sine-signal carries all power in one frequency within the pass-band, the given ratio defines the offset between the curves in Fig. 4.22. The measured offset in the linear region is $2.6\,\mathrm{dB}$.

Finally, the conversion gain in the linear region can be found in Tab. 4.3. It is in the order of $52\,\mathrm{dB}$, which is in good agreement with what can be derived from the data sheets of the used components.

channel	signal type	gain	channel	signal type	gain
C_1	sine	$52.4\,\mathrm{dB}$	C_2	sine	$52.4\,\mathrm{dB}$

Table 4.3: Conversion gain of the dual-path receiver in linear operation.
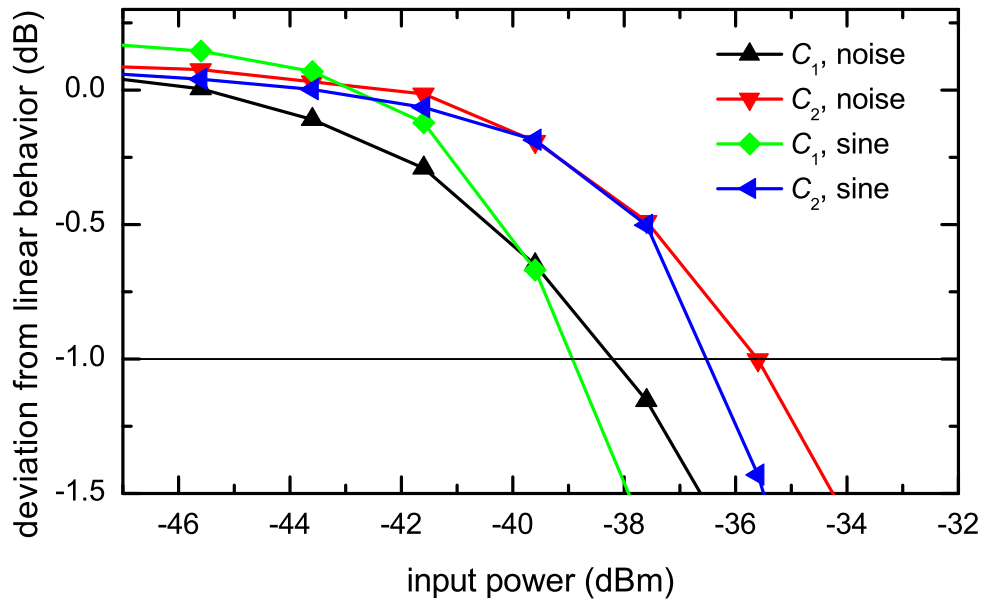
Figure 4.23: Plotting the difference of measured values to an extrapolation
of a linear fit of the data in the linear region clearly shows the 1 dB
compression points and that they are different for each channel and for
different types of signals.

4.1.9 Third moment of amplifiers

During his measurements for Ref. [25], E. P. Menzel recognized a permanent third
moment originating from the noise of the detection chain. To get clarity on this
third moment, measurements on it are done within this thesis. As a first step, a
power-sweep (setup in Fig. 4.21) is performede to investigate the time- and ensemble-
averaged third moments of the dual-path channels in dependence on power. Fig-
ure 4.24 shows clearly that a third moment arises when the region of amplifier
compression is reached. In Fig. 4.25, the same data is shown in a logarithmic scale.
This uncovers that the third moments are always present, even for very low powers.
As the third moment drastically increases when reaching the power region in which
the amplifiers start to show compression (see Sec. 4.1.8), the amplifiers where sus-
pected to be the origin of the effect. The amplifiers are traced down as the source
by replacing them by each other. In this case, one observes the exact same behavior
as before, but with channels exchanged (data not shown).
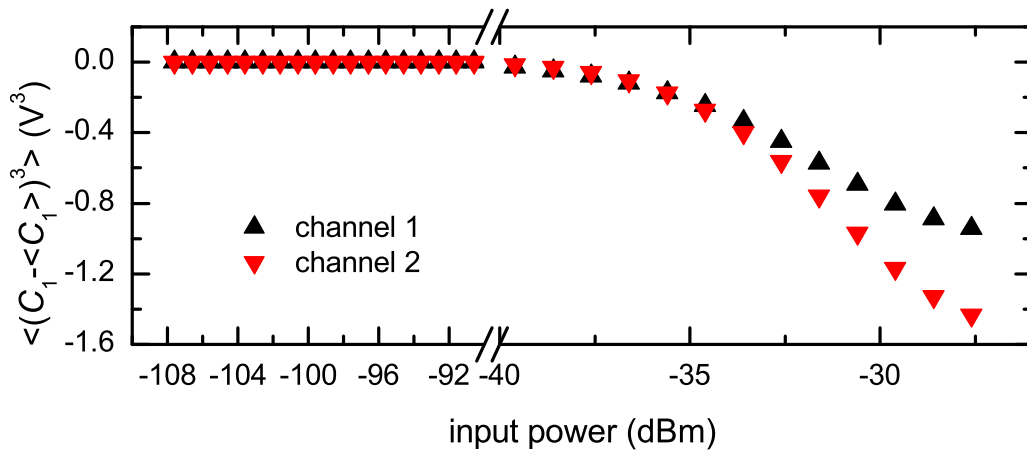
Figure 4.24: Third moment depending on input power. The appearing third moment has been identified to result from the amplifiers coming into the region of compression.
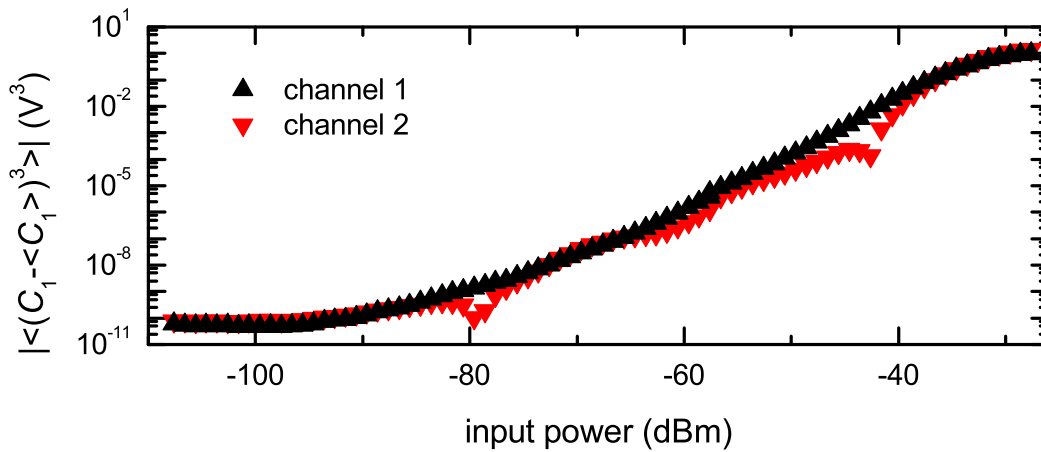
Figure 4.25: On a logarithmic scale a permanently present third moment can be seen. The logarithm of the absolute value of the third central moment is plotted. The dips in the red curve (channel 2) have not yet been identified.

4.2 Resolution limits of the dual-path receiver

In this section, a resolution limit definition in the context of the present setup is given and a probe signal is presented. Based on this, the resolution limits of the dual-path receiver are investigated. A precise review on the probe signal, measurement process and dual-path correction is given. Finally, the resolution limit measurements and dependencies on ensemble size and noise spectral density are discussed. Where possible, the measurements are compared to corresponding simulations and to the results of Menzel *et al.* [25].

4.2.1 Resolution limit definition

The dual-path method recovers moments of small signals from an ensemble of noisy traces. A figure of merit for the quality of the method, and thus also for the receiver, is the resolution limit, which is defined by the smallest signal moment that can be distinguished from noise.
The first three (central) signal moments are defined as

$$FM := \langle S \rangle \quad , \tag{4.4}$$

$$SCM := \langle (S - \langle S \rangle)^2 \rangle \quad , \tag{4.5}$$

$$TCM := \langle (S - \langle S \rangle)^3 \rangle \quad , \tag{4.6}$$

where FM is the first moment, SCM and TCM are the second and third *central* moments. For now, a sine-signal, free of any noise, shall be considered. Differing from higher moments, the *raw* first moment is used, because the first central moment is zero by definition. The variance or squared standard deviation $\sigma_{n,\text{signal}}^2$ of any of the central moments is defined as

$$\sigma_{n,\text{signal}}^2 := \frac{1}{T_{\text{pulse}}} \int_0^{T_{\text{pulse}}} (nCM(t) - \overline{nCM(t)})^2 dt \quad , \tag{4.7}$$

where n gives the order of the moment and $\overline{nCM(t)}$ is the time average of $nCM(t)$ in one period of the probe signal. For the considered case of a sine-signal, $\sigma_{n,\text{signal}}$ can be calculated analytically (see App. B.3). In an actual experiment, although already dual-path corrected traces of the signal moments (see Sec. 4.2.3) are analyzed, remaining noise contributions will cause statistical deviations. The variance $\sigma_{n,\text{noise}}^2$ of these contributions can be seen in the off-pulse region, where no sine-signal is present at all. As we expect the signal and the noise to be statistically independent, the standard deviation in the pulse region is $\sigma_n = \sqrt{\sigma_{n,\text{noise}}^2 + \sigma_{n,\text{signal}}^2}$. Using the fact that $\sigma_{n,\text{signal}}^2$ is input power dependent (derived for probe signal in App. B.3), with a factor of proportionality β_n, the root mean square amplitude σ_n is defined as

$$\sigma_n(P) = \sqrt{\sigma_{n,\text{noise}}^2 + \sigma_{n,\text{signal}}^2} = \sqrt{\sigma_{n,\text{noise}}^2 + \beta_n P^n} \quad , \tag{4.8}$$

where P is the input power. The resolution limit for a moment of order n then is defined as the power $P_{\text{RL},n}$ at which the contribution of $\sigma_{n,\text{signal}}$ becomes equal to the noise contribution $\sigma_{n,\text{noise}}$. This can be written as

$$\beta_n P^n = \sigma_{n,\text{signal}}^2 \overset{!}{=} \sigma_{n,\text{noise}}^2 \quad . \tag{4.9}$$

This leads to expressions for resolution limits of the first moment $P_{\text{RL},1}$, the second central moment $P_{\text{RL},2}$, the third central moment $P_{\text{RL},3}$ and in general the nth central moment $P_{\text{RL},n}$:

$$P_{\text{RL},1} = \beta_1^{-\frac{1}{1}} \cdot \sigma_{1,\text{noise}}^{2/1} \tag{4.10}$$

$$P_{\text{RL},2} = \beta_2^{-\frac{1}{2}} \cdot \sigma_{2,\text{noise}}^{2/2} \tag{4.11}$$

$$P_{\text{RL},3} = \beta_3^{-\frac{1}{3}} \cdot \sigma_{3,\text{noise}}^{2/3} \tag{4.12}$$

$$P_{\text{RL},n} = \beta_n^{-\frac{1}{n}} \cdot \sigma_{n,\text{noise}}^{2/n} \tag{4.13}$$

4.2.2 Probe signal

As propagating quantum microwaves are expected to cause non-zero higher central moments at the dual-path receiver, using a coherent probe signal is not sufficient. Thus a way had to be found to generate a probe signal which shows higher order moments. Up to now only moments up to the third order are measured, so at least a third order moment had to be generated. This problem is solved by forcing the SMF to generate two signals S_1 and S_2, phase shifted by an angle $-\varphi$ or $+\varphi$, at a rate of 1:x. This means every xth trace is of type S_2 (phase shifted by $+\varphi$), all others are of type S_1 (phase shifted by $-\varphi$). Thus, an ensemble consists of signals S_1 and S_2 with probability of occurrence $p_{\text{S}1} = x/(1+x)$ and $p_{\text{S}2} = 1/(1+x)$. On average, this gives a first moment signal of the form:

$$\langle S \rangle = p_1 S_1 + p_2 S_2 \tag{4.14}$$

$$\langle S \rangle = p_1 A \sin\left(\omega t - \varphi\right) + p_2 A \sin\left(\omega t + \varphi\right) \quad . \tag{4.15}$$

For a fixed ratio of 1:3 and a fixed phase shift $\varphi = 90°$, as it will be used for resolution limit measurements, this leads to

$$\langle S \rangle = -\frac{A}{2} \cos\left(\omega t\right) \quad , \tag{4.16}$$

$$\langle (S - \langle S \rangle)^2 \rangle = \frac{3}{4} A^2 \cos^2(\omega t) \quad , \tag{4.17}$$

$$\langle (S - \langle S \rangle)^3 \rangle = \frac{3}{4} A^3 \cos^3(\omega t) \quad . \tag{4.18}$$

It is notable that although the factor $\frac{3}{4}$ appears in the second and third central moment. This needs not be true in general for higher moments. Using the analytical expressions (4.17) and (4.18) for the second and third central moment, the

fitting parameters β_2 and β_3 can be derived analytically and are compared to the values obtained from measurements and simulations (see Tab. 4.4). The values show nearly perfect agreement. All measurements in the following are performed at a

Type	N	P_{noise} (dBm)	Fig.	β_2	β_3
Exp.	1^7	-57	4.31	$9.47 \cdot 10^4$	$2.9 \cdot 10^8$
Sim.	1^7	-57	4.31	$1.03 \cdot 10^5$	$3.14 \cdot 10^8$
Sim.	10^6	-57	B.5, B.6	$1.06 \cdot 10^5$	$3.03 \cdot 10^8$
Exp.	10^5	-57	B.5, B.6	$1.02 \cdot 10^5$	$3.07 \cdot 10^8$
Sim.	10^5	-57	B.5, B.6	$1.06 \cdot 10^5$	$3.03 \cdot 10^8$
Sim.	10^4	-57	B.5, B.6	$1.06 \cdot 10^5$	$3.02 \cdot 10^8$
Sim.	10^7	-50	B.4	$1.03 \cdot 10^5$	$3.13 \cdot 10^8$
Sim.	10^7	-40	B.4	$1.03 \cdot 10^5$	$3.15 \cdot 10^8$
Theory	-	-	-	$1.03 \cdot 10^5$	$3.12 \cdot 10^8$

Table 4.4: Fitting parameters β_{nCM}

LO-frequency of $5.624\,\text{GHz}$ and RF-frequency of $5.640\,\text{GHz}$, if not stated else.

φ-dependence

To prove that the phase shifted signals show the expected behavior the φ-dependent cross variance amplitude $\alpha = A^2 \sin^2(\varphi)$ is investigated for a 1:1 mixture. Figure 4.26 shows measurement, simulation and additionally a comparison to the results in [25]. Almost perfect agreement is achieved.
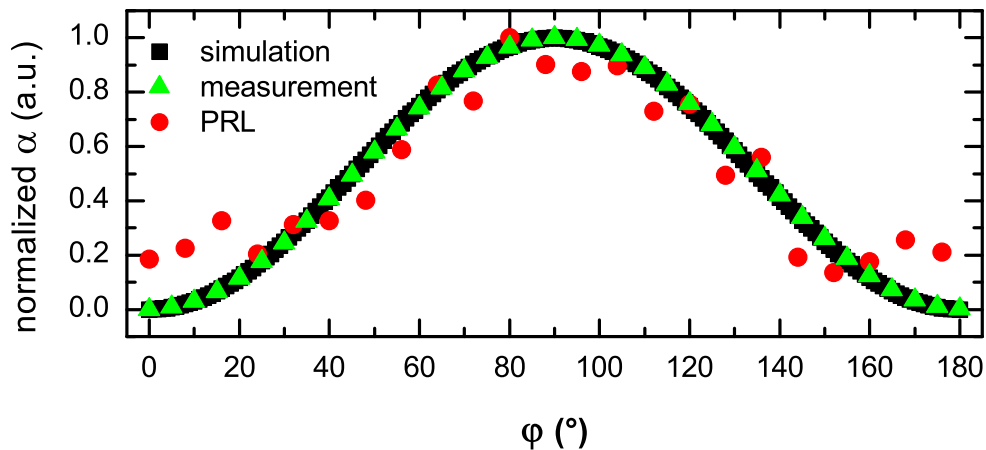
Figure 4.26: φ-dependence of a 1:1 signal mixture. As measurements in [25] were done near the resolution limit some deviations appear (red data points from Ref. [25]. To be able to compare the data sets, they have been normalized.

4.2.3 Dual-path correction and moment statistics

In simple words, one wants to measure a very low power signal. As detectors are not capable of directly measuring such low level signals, they have to be preamplified and thus noise is added. The dual-path scheme is able to separate the original signal from the noise contributions by splitting the signal. The signal emulator discussed in Ch. 3 provides a composition of a sinusoidal *probe signal* (see Sec. 4.2.2), generated by a signal source, and *white noise*, generated by amplification of the Johnson-Nyquist noise signal of a $50\,\Omega$ terminator at room temperature.

Thus, a single measurement gives a trace in which the probe signal cannot be recognized anymore. However, moments can be calculated, giving a time trace for every moment in each channel, e.g., $C_1(t)$, $C_2(t)$, $C_1(t)C_1(t)$, $C_1(t)C_2(t)$, $C_2(t)C_2(t)$, ... (see Fig. 4.29). By averaging a recorded ensemble of such moment traces a time trace for every moment and channel is obtained, e.g. $< C_1(t) >$, $< C_2(t) >$, $< C_1(t)C_1(t) >$, $< C_1(t)C_2(t) >$, $< C_2(t)C_2(t) >$, ... (see Fig. 4.30). The reader once again shall be advised that the plotted signal moments are *not* the moments of the probe signal. In order to access the moments of the probe signal the dual-path scheme has to be applied by means of equations[1] given in chapter 2. For example, the third central moment TCM of the probe signal is obtained by

$$
\begin{aligned}
TCM &= \langle (S - \langle S \rangle)^3 \rangle \\
&= \frac{1}{2}\big(\,(\,\langle C_1 C_2 C_2 \rangle - 2\langle C_1 C_2 \rangle\langle C_2 \rangle - \langle C_2 C_2 \rangle\langle C_1 \rangle\,) + 2\langle C_1 \rangle\langle C_1 \rangle\langle C_1 \rangle + \\
&\qquad (\,\langle C_1 C_1 C_2 \rangle - 2\langle C_1 C_2 \rangle\langle C_1 \rangle - \langle C_1 C_1 \rangle\langle C_2 \rangle\,) + 2\langle C_1 \rangle\langle C_1 \rangle\langle C_1 \rangle\,). \quad (4.19)
\end{aligned}
$$

Figure 4.27 shows an ensemble-averaged third central moment for every point in time, obtained by using Eq. (4.19). Now, this trace indeed characterizes the probe signal. $\sigma_{3,\text{noise}}$ and $\sigma_3(P)$ can be obtained from statistics in time domain in the off-pulse
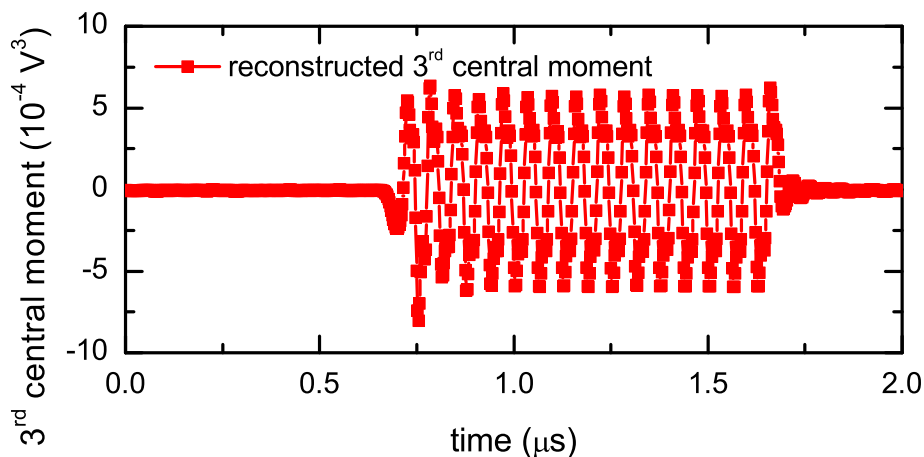
Figure 4.27: Reconstructed 3$^{\text{rd}}$ central moment trace of the signal.

---

[1]Some signs in Eq. (4.19) differ from theory in Ch. 2, because the *signal emulator* uses a power divider whereas in theory a hybrid ring is assumed.

and on-pulse regions, respectively. To clarify the order of the different averaging procedures and moment calculations, the steps just described are summarized as a flow-diagram in Fig. 4.28.
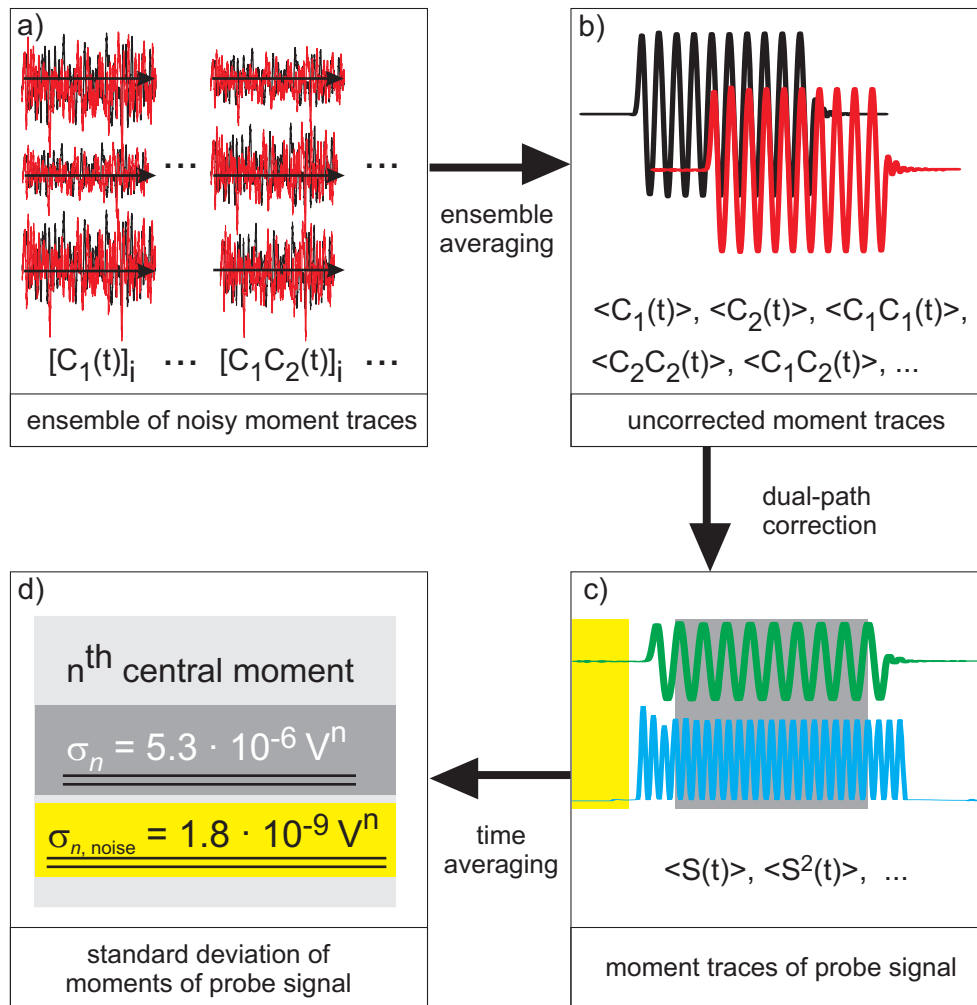
Figure 4.28: The measurement and dual-path correction process: a) An ensemble of time traces of moments is recorded. The moments of the probe signal cannot be recognized in a single trace. b) By averaging an ensemble of noisy moment traces the uncorrected signal moments $< C_1(t) >, < C_2(t) >, < C_1(t)C_1(t) >, < C_1(t)C_2(t) >, \ldots$ are obtained. c) Applying dual-path correction allows for reconstruction of the signal moments of the probe signal. d) Time domain statistics in the off-pulse region (yellow shaded area) is used to obtain $\sigma_{n,\text{noise}}$ and in the on-pulse region (gray shaded area) to determine σ_n of the probe signal.
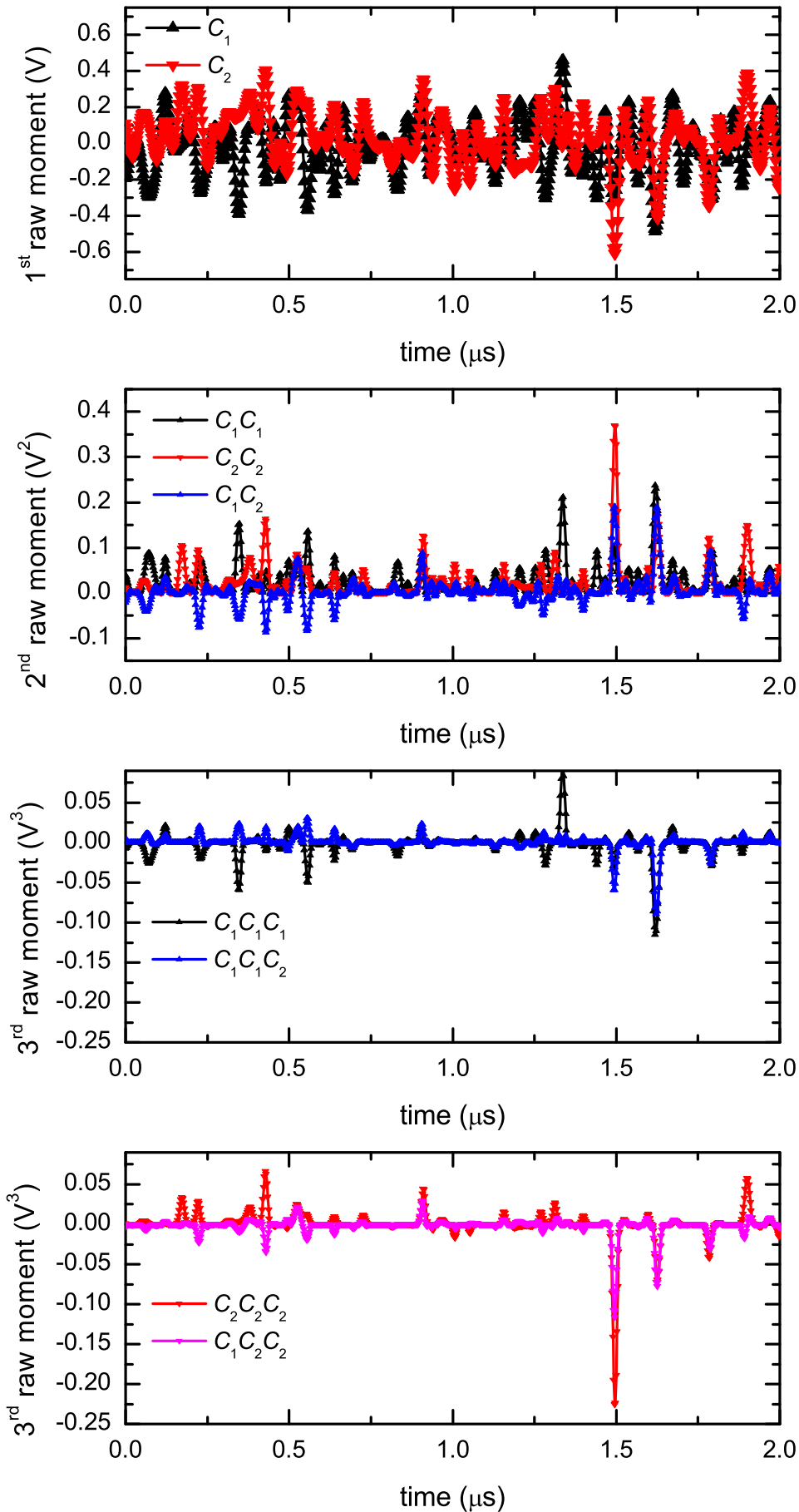
Figure 4.29: Raw signal moment traces. An ensemble of such traces is recorded for averaging. Note that the signal levels are large compared to the signal level of the averaged signals in Fig. 4.30.
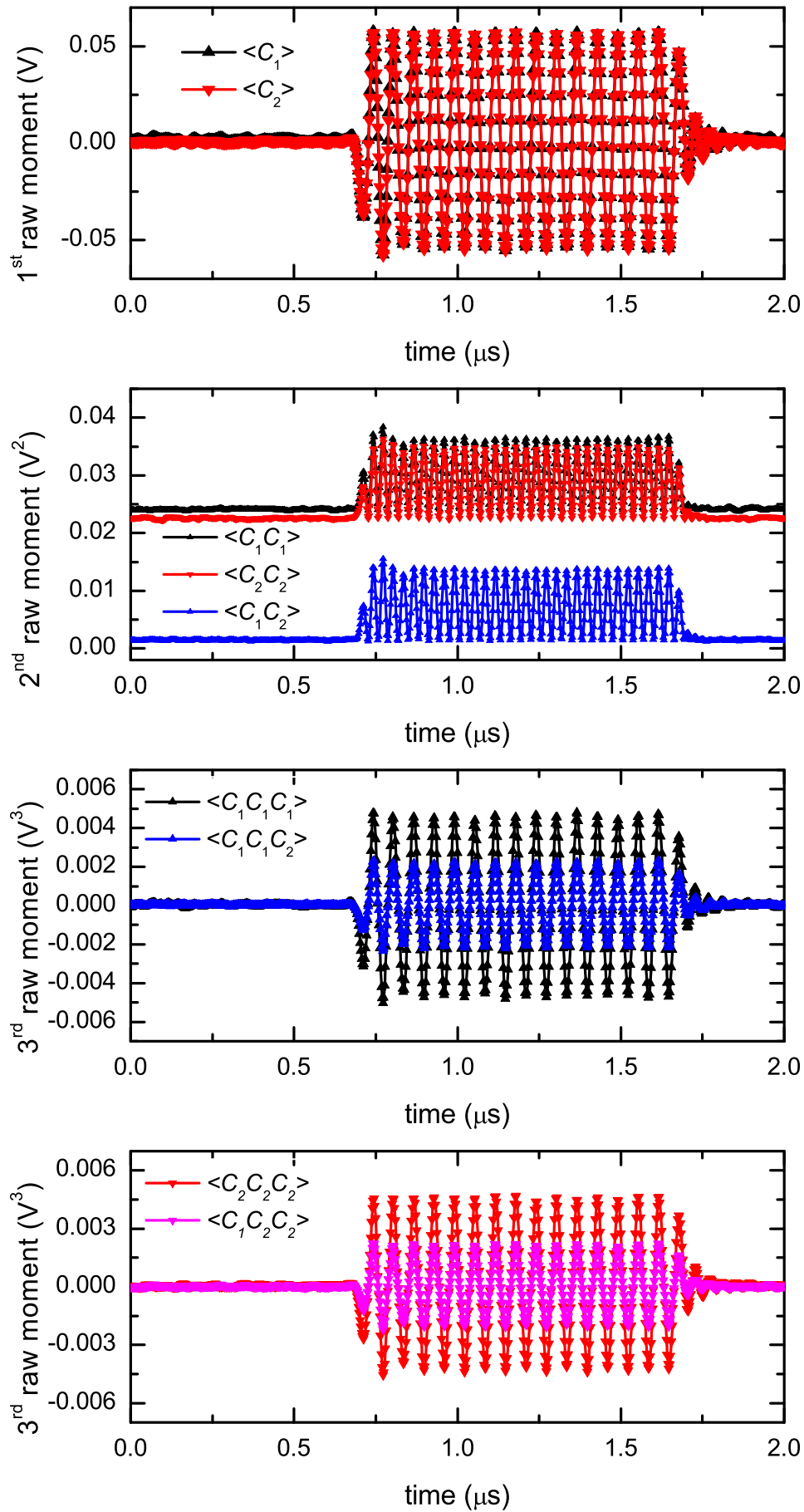
Figure 4.30: Averaged signal moment traces. Note the low signal levels.

4.2.4 Resolution limit measurements

In order to make use of Eqs. (4.10)-(4.12), the parameters β_n and $\sigma_{n,\text{noise}}$ are required. These can be determined by plotting the σ_n of a signal moment against input power[2] and fitting the data to Eq. (4.8). The parameter β_n is determined by the interception of the extrapolated high power limit with the y-axis at $0\,\text{dBm}$ input power (see Fig. 4.31) or can also be obtained analytically (see App. B.3). $\sigma_{n,\text{noise}}$ is given by
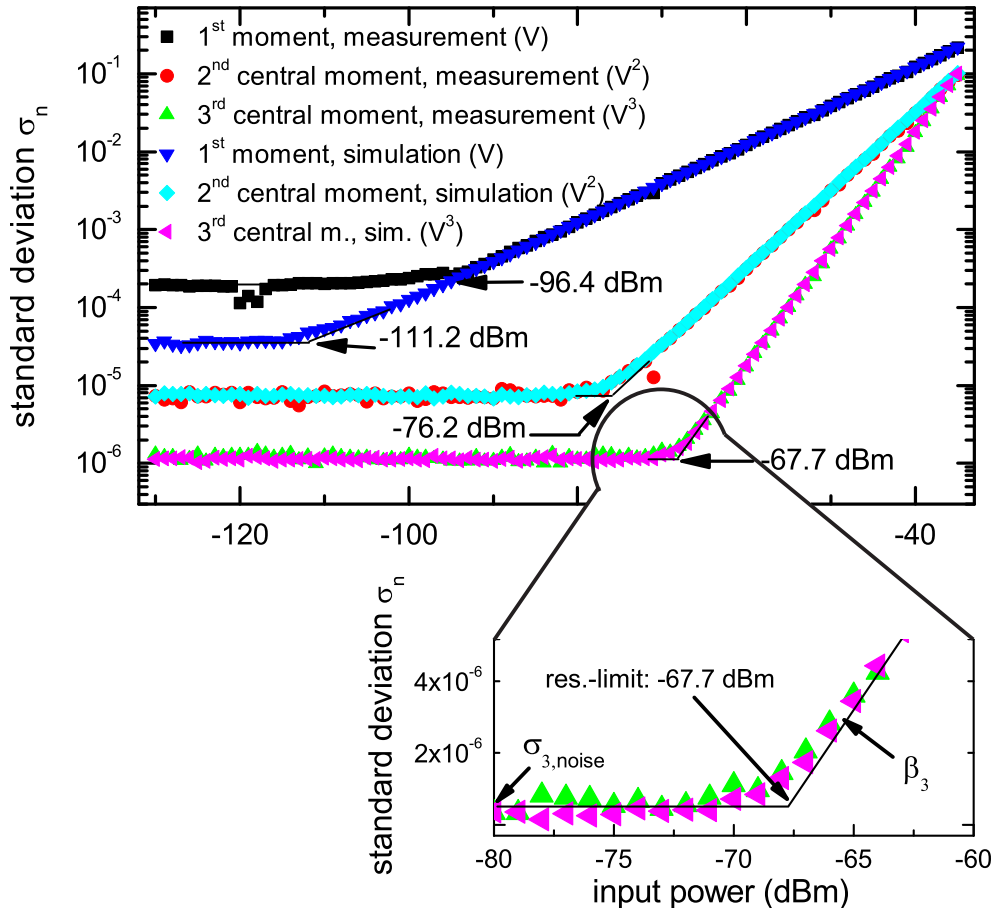
Figure 4.31: Power sweep to determine the resolution limit of first, second and third moment. The blow-up shows how the fitting parameters ($\sigma_{n,\text{noise}}$ and β) can be obtained in geometrical way. The interception of the black lines indicating asymptotic behaviors of the curve gives the resolution limit. The mean value at low powers determines $\sigma_{n,\text{noise}}$ and β is given by the y-interception of the high power asymptote with a vertical line at $0\,\text{dBm}$ input power.

the saturation value in the low power limit of the power sweep (see Fig. 4.31) or by calculating the standard deviation in the off-pulse region of a moment trace (at any input power). Using this method and already knowing β_n from a single power sweep

---

[2]Indeed the source output power, which is $11.4\,\text{dB}$ higher than the input power at the receiver input, is plotted (see also Fig. 4.36a).

or using the analytical value, it is possible to calculate the resolution limit without performing a power sweep. This approach tremendously saves measurement time. Figure 4.31 shows a power sweep for experiment and simulation. The agreement between experiment and simulation is very good, with the exception of the first moment. A possible reason for this can be the fact that in the simulation real white noise is generated, whereas in the experiment all signals are band limited. Another reason could be spurious signals at the digitizer card. However, from Fig. 4.31 the parameters $\beta_1 = 1.52 \cdot 10^2, \beta_2 = 1.03 \cdot 10^5$ and $\beta_3 = 3.14 \cdot 10^8$ are obtained. To
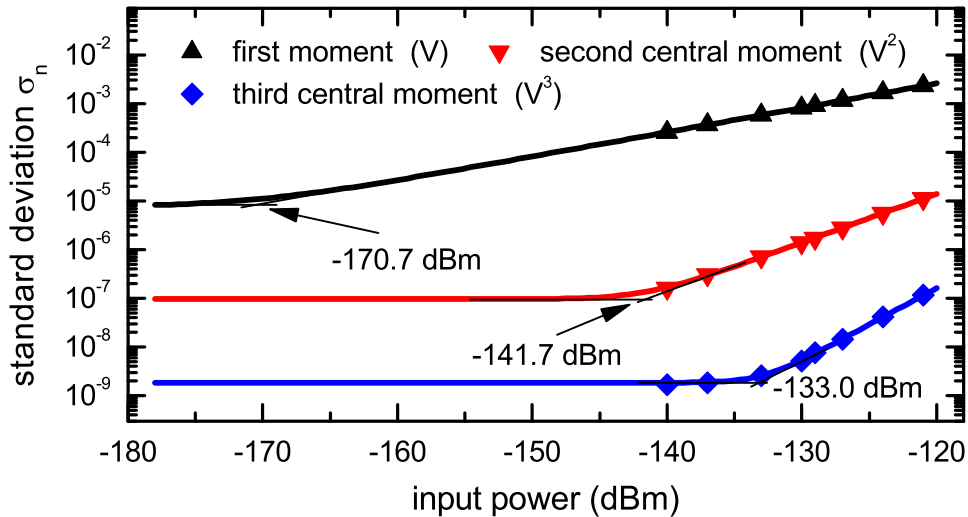
Figure 4.32: Extrapolation of data in [25] to obtain resolution limits, denoted by the black arrows. The power considered at the x-axis is at the input of the hybrid ring in the cryogenic setup of [25].

demonstrate how useful the different ways of obtaining the fitting parameters are, in Fig. 4.32 the resolution limits of the first, second and third moment are determined from data measured in [25]. The problem is that data for input powers lower than $-140\,\mathrm{dBm}$ is not available. Nevertheless, the resolution limits can be obtained by calculating $\sigma_{n,\mathrm{noise}}$ from the off-pulse region of a trace at one of the measured powers and then fitting to Eq. (4.8) with only β_n as fitting parameter.

4.2.5 Dependence on noise spectral density

In this section, the dependence of resolution limit on the noise spectral density at the receiver input is investigated. For measurements the *signal emulator* was slightly modified by adding two programmable step attenuators in order to be able to control the noise added to the signal (red in Fig. 4.33). Figure 4.34 shows a sweep of *noise spectral densities* from -170 to $-131\,\mathrm{dBm/Hz}$ for a signal of $-60\,\mathrm{dBm}$, done with an ensemble size of 10^7 samples for simulation and measurement. The lower bound of the sweep range was chosen close to the spectral density of room-temperature thermal noise of $-174\,\mathrm{dBm/Hz}$. The dependence on noise spectral density in Fig. 4.34
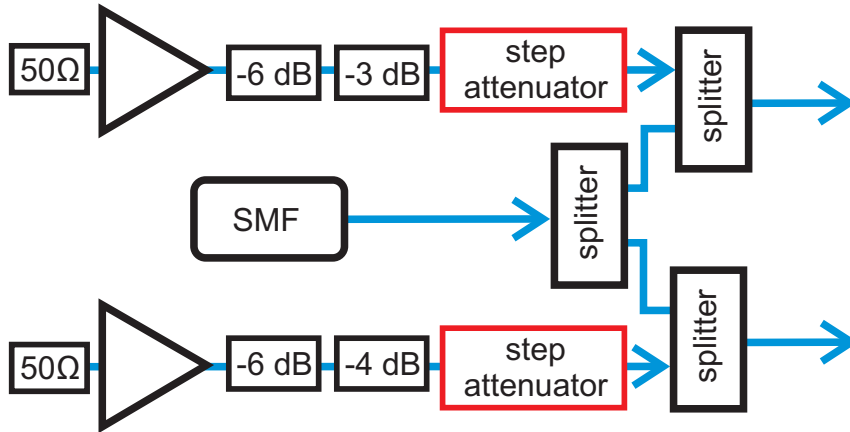
Figure 4.33: Setup for noise spectral density dependence of resolution limit. Note: The power level of the signal at the output of the signal emulator is 11.4 dB lower than the power set at the microwave source (see Fig. 4.36).
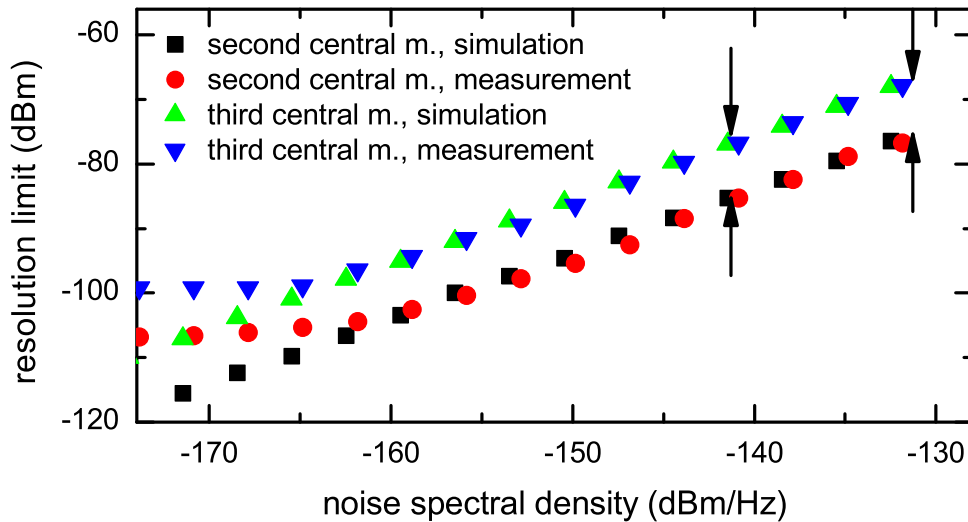
Figure 4.34: Resolution limit of second and third central moment depending on noise spectral density. Arrows indicate resolution limits obtained by power sweeps shown in Fig. B.4.

was obtained by simulating or measuring $\sigma_{n,\text{noise}}$ for every noise spectral density and using the already known β_n to calculate the resolution limit with Eqs. (4.10)-(4.12). To confirm the results, simulations of signal power sweeps for fixed noise spectral densities of -131.4 and -141.4 dBm/Hz have been done (Fig. B.4, arrows in Fig. 4.34) and the results do coincide. Additionally, Fig. 4.34 shows that the resolution limit is linear in noise spectral density and saturates for spectral noise densities lower than -162 dBm/Hz per chain. As in this test setup no cryogenic setup is connected, this gives the point where the receiver noise dominates in the system. For future experiments, this means that signals have to be amplified above the resolution limit associated to this -162 dBm/Hz spectral noise density, to be able to resolve second and third moments. Of course, additional noise contributions

are expected to originate from the cryogenic part of the setup, so the signal level at the input of the dual-path receiver will have to be higher than the lower bound given by the curve at the specified noise density. So far, all resolution limit values have been given in terms of the power level set at the SMF. To be able to give estimations on necessary signal levels at the output of the cryogenic setup, respectively the input of the receiver, in Fig. 4.35 the lower bound for the signal at the receiver input (resolution limit) is plotted depending on the noise spectral density at the receiver input (see Fig. 4.36 for details). It shall be noted that this does not mean that signals lower than the lower bound cannot be resolved. If in the cryogenic part the signal is amplified above the lower bound and the noise added is low enough, or in other words the signal to noise ratio is high enough, then the level of the lowest signal that can be resolved is not limited by the receiver noise. This also is in agreement with theoretical predictions, which tell us that the signal to noise ratio at the first cryogenic amplification stage governs the resolution limit that can be obtained.

As an example let us consider that we want to resolve a signal of $-144\,\mathrm{dBm}$ (equals one photon on average in [25]) and the cryogenic setup has a spectral noise density of $-95\,\mathrm{dBm/Hz}$ at its output. This noise level is $70\,\mathrm{dB}$ above the point where the receiver noise gives significant contributions and thus completely governs the noise in the system. From Fig. 4.35 we see that the original signal has to be amplified up to a level of $-55\,\mathrm{dBm}$ and $-44\,\mathrm{dBm}$ at the receiver input for resolving the second and third central moment, respectively (see Fig. 4.35). This equals an amplification of $\approx 90\,\mathrm{dB}$ of the original $-144\,\mathrm{dBm}$ signal and reproduces the conditions in Ref. [25] well.
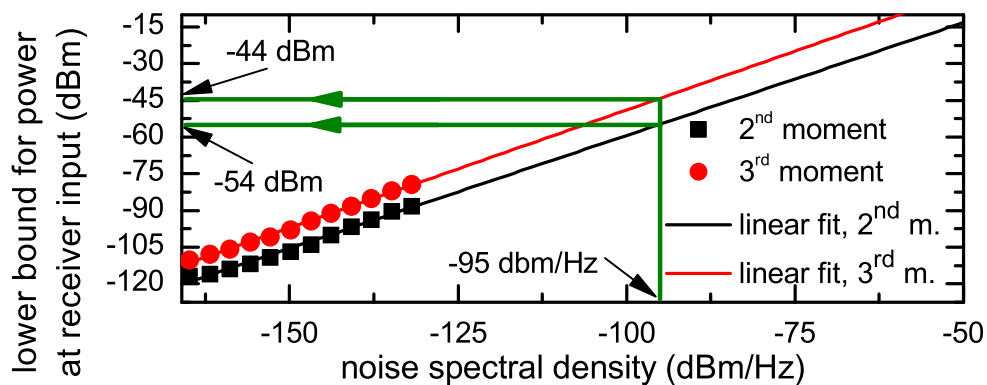
Figure 4.35: Lower bound on the signal level required at the receiver-input for resolving signals. Depending on how much noise is added to the receiver noise by the cryogenic setup, the resolution limit will get worse. The green lines indicate the example given in the main text, where an assumed noise spectral density of $-95\,\mathrm{dBm/Hz}$ leads to lower bounds for the signal at the receiver input of $-55\,\mathrm{dBm}$ and $-44\,\mathrm{dBm}$, respectively.
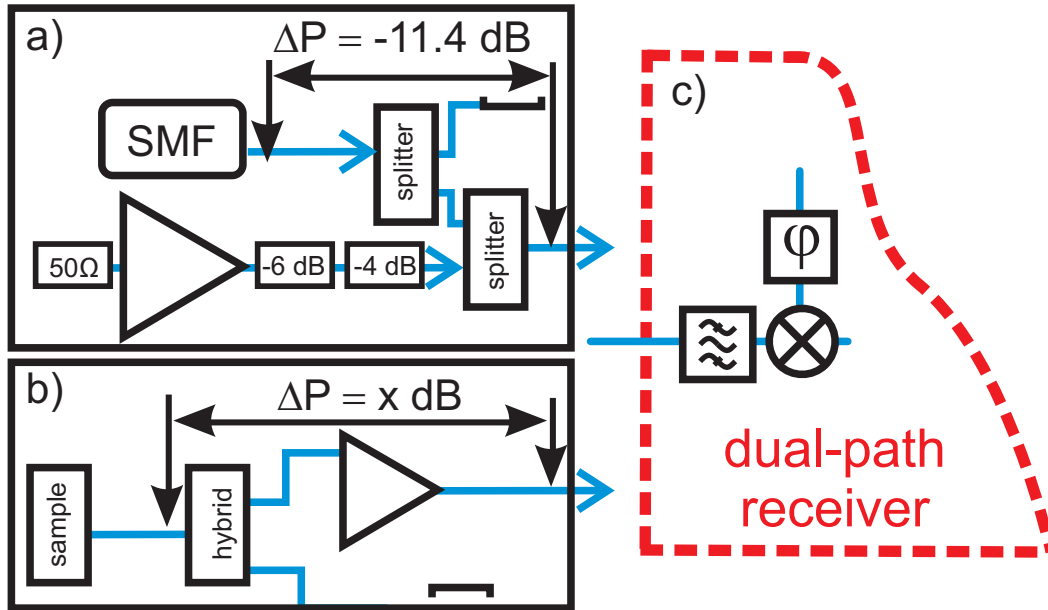
Figure 4.36: Comparison of signal generation in signal emulator and in real
dual-path experiment: a) The signal generated by the SMF is attenuated
by 11.4 dB and artificially generated noise is added. b) In the experiment,
the signal at the input port of the hybrid ring is amplified by x dB and
noise is added in this process. c) Either signals from (a) or (b) can be
measured.

4.2.6   Dependence on ensemble size

Due to general statistical arguments the standard deviation σ_n of the nth moment
should be proportional to $\frac{1}{\sqrt{N}}$, where N is the ensemble size. Thus, according to
Eqs. (4.13) the resolution limit is expected to be proportional to $\sigma_n^{\frac{2}{n}} \propto (\frac{1}{\sqrt{N}})^{\frac{2}{n}} = N^{-n}$.
Simulations on the influence of the ensemble size are plotted in Fig. 4.37. Linear
fits of the double logarithmic plot give slopes of -1, $-1/2$ and $-1/3$ for the first
moment, second central moment and third central moment, respectively. This is
in perfect agreement with the statistical arguments. Figures B.5 and B.6 show
snapshot measurements confirming the simulation results of Fig. 4.37. It can be
seen that increasing the ensemble size is a reliable way to obtain better resolution
limits. This illustrates the importance of realtime measurements using a FPGA-card
(see Sec. 3.3).
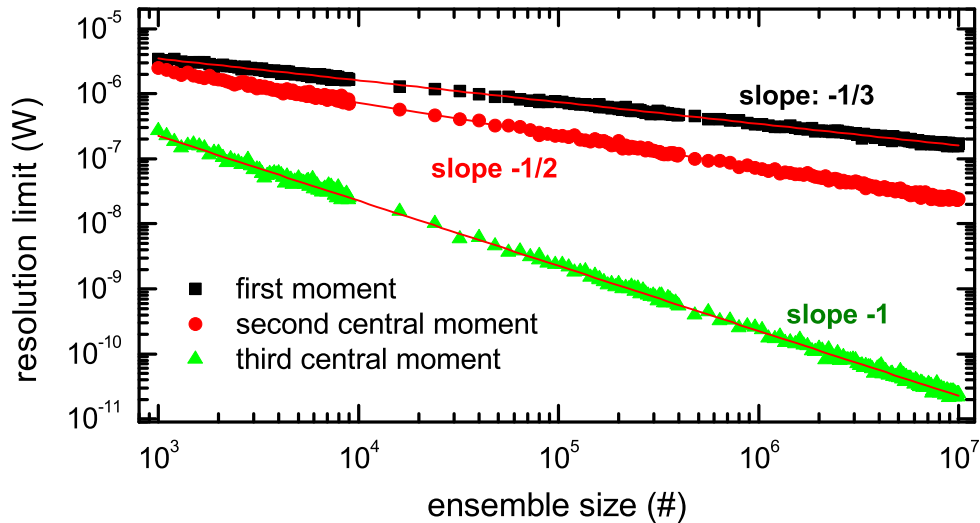
Figure 4.37: Ensemble size dependence of resolution limit for different moments. Slopes of fit curves are in perfect agreement with statistical predictions.

4.3 Preliminary IQ-measurements

Signal quadratures and their moments are required for signal reconstruction and their measurement has been introduced in Sec. 2.4. As mentioned in Sec. 3.2, the feature of quadrature moment measurement has been implemented and added to the measurement software during the course of this thesis. All measurements in Sec. 4.2 have been done with the IQ-option activated, so data for obtaining resolution limits for IQ-measurements is available. As still some work on theory (quantum reconstruction, definition of resolution limits for complex signals, oscillations in digital homodyning) has to be done, only some preliminary results are shown in this section.

Figures 4.38-4.40 show traces of averaged, uncorrected I and Q moments. In exact analogy to 'ordinary' signals, the noise background is canceled in the terms correlating signals from different chains, e.g., $\langle I_1 I_2 \rangle$ in Fig. 4.39. In the higher order moments an oscillation is observed, which is inspected in the following.
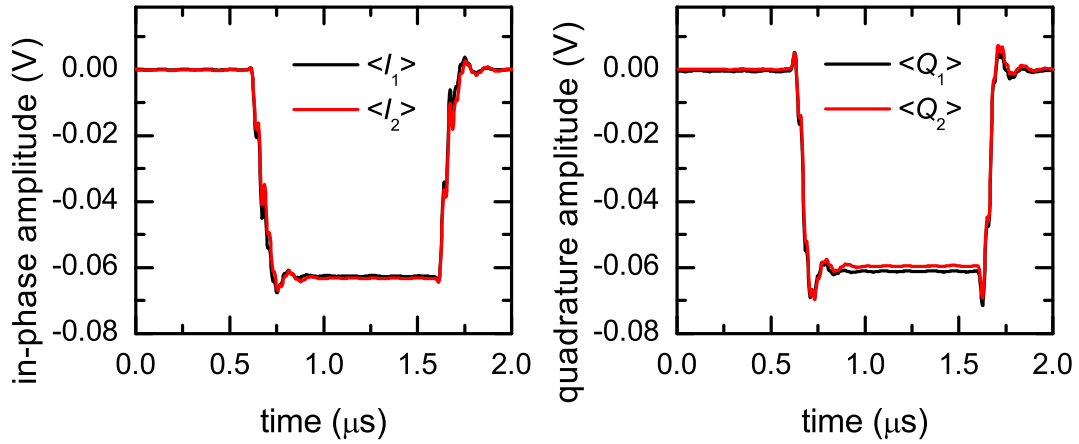
Figure 4.38: Exemplary traces for the first moment of I, respectively Q.
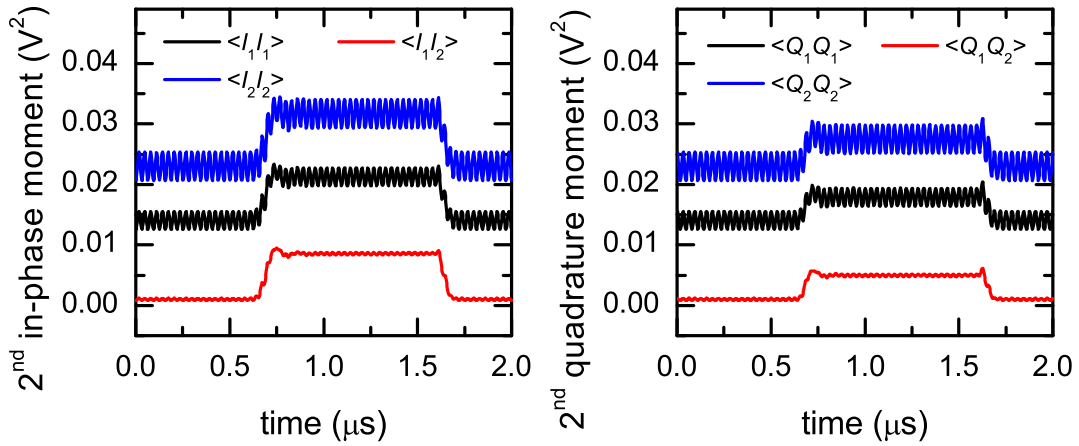
Figure 4.39: Exemplary traces for the second moments of I, respectively Q. Oscillations are observed in the whole time-trace.
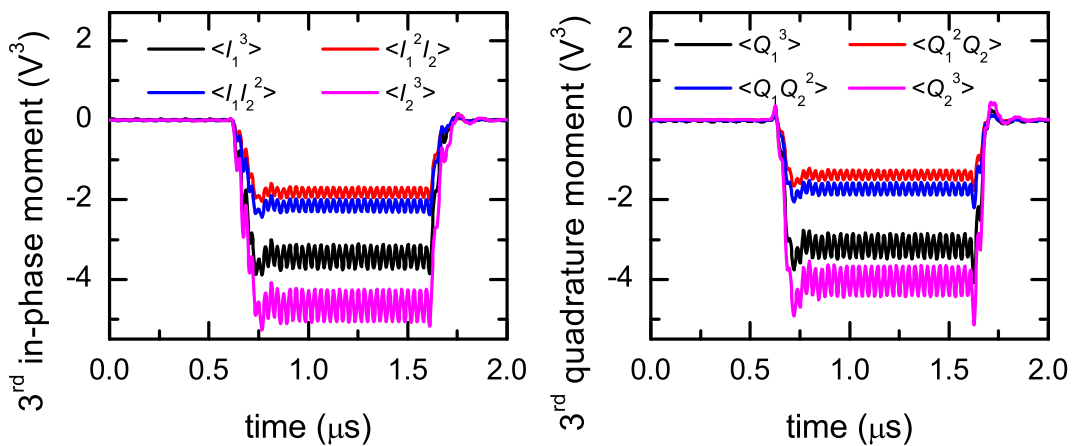
Figure 4.40: Exemplary traces for the third moments of I, respectively Q. Oscillations are observed in the whole time-trace.

4.3.1   Oscillation in IQ-reconstruction of band limited noise

Measurement of quadrature components I, Q is done by means of *single channel digital homodyne* (see Sec. 2.4). In experiments, the second moment of I, respectively Q, show oscillations at double intermediate frequency, which is not expected at first hand. The oscillations appear in the whole signal trace, not only in the pulse region and thus have to be a feature of the noise. The oscillation could not be reproduced in simulations with white noise. Thus, a dataset with digitally filtered white noise, simulating band-limited noise, was generated to use it as an input for the dual-path simulation. With this approach it was possible to reproduce the behavior of the real setup. Therefore, the oscillations can be attributed to the band-limitation introduced by filters in the setup. Figure 4.41 shows a simulation for the second moment of I, $\langle I^2 \rangle$, for white noise and for band-limited noise. A possible solution to this issue is time averaging over one period of the IF-frequency, either with decimation of time-points or in a sliding average.
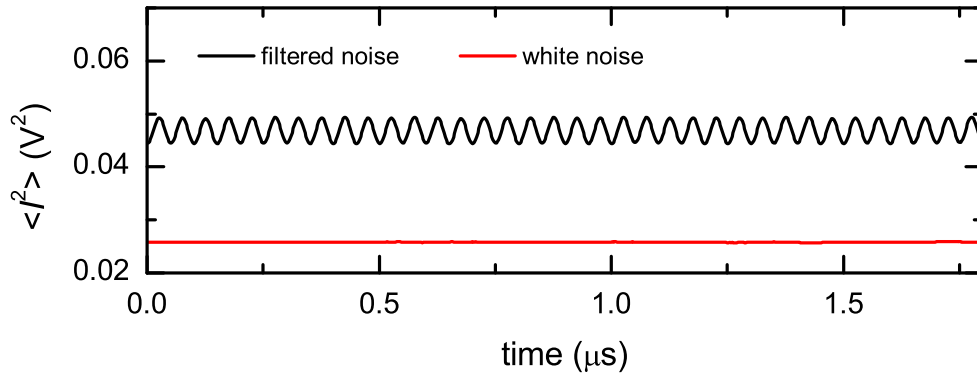
Figure 4.41: Using band-limited noise as an input results in oscillations in the quadrature moments. This behavior is not observed for white noise.

Chapter 5

Summary & Outlook

In recent years, the new field of circuit QED, dealing with quantum electrodynamics realized with superconducting circuits at cryogenic temperatures, has emerged. Impressive progress was made in both, understanding physical foundations [17] and in applications of circuit QED in quantum information processing [12]. Despite great achievements, state reconstruction of propagating microwaves still is challenging. With the introduction of the dual-path method [25] by Menzel *et al.*,a possible solution to this problem was given. In this thesis, a key component of this dual-path method, the dual-path receiver, is thoroughly investigated. In this way, we bring the dual-path method one step further towards becoming a standard tool in state reconstruction. As a first step, an overview on the theory of the dual-path method and the interesting physics behind state reconstruction of non-classical states is given. In strong contrast, the experimental part of this work then deals with very technical details.

The first main achievement of this work is the documentation of the receiver design in all its technical details. In addition, a number of improvements in the receiver design were implemented. For example, additional filters, automatic correction for imbalances, galvanically separating the phase shifter from the power supply, and different types of power supplies are considered, tested and implemented. The thorough characterization of the receiver is an important prerequisite when planning to use the receiver in quantum state reconstruction experiments. Hence, properties of the dual-path receiver and its components, such as phase stability, timing, calibration, decorrelation effects, jitter and linearity have been investigated.

The second major development performed during this work is the measurement software. Digital homodyne detection has been implemented and the measurement time has been considerably reduced by using modern programming techniques.

The third main result is the guideline to building future setups given by the proof-of-principle experiments and resolution limit observations. In particular, the results for the dependence of the receiver resolution on ensemble size and noise spectral density give indications on future improvements of the dual-path receiver and provide efficient procedures for characterization and calibration. Additionally,

most experimental results are backed up by simulations and are compared to Ref. [25] to prove consistency and reproducibility.

In summary, on the basis of this thesis a well-documented and well-characterized dual-path receiver is available and can be used for implementing an experiment utilizing the dual-path scheme for reconstruction of propagating quantum microwaves, such as the upcoming measurements of squeezed states generated by a Josephson parametric amplifier. Because of the implementation of digital homodyning, this can be done on a two-channel digitizer, which is available at WMI. Furthermore, the stage is set for creating *Wigner function*-reconstruction software. Based on the work already done during this thesis, it should be straightforward to combine the existing measurement program developed and the MATLAB-prototypes for reconstructing Wigner functions, done by the group of Prof. Solano. The implementation and thorough tests of reconstruction of a non-classical state with this software will be a interesting and challenging assignment. Additionally, based on the preliminary work during this thesis it will soon be possible to replace the Acqiris digitizer card by an analog to digital converter utilizing a FPGA. Using this powerful data-processor in conjunction with IQ-mixers will allow for realtime measurements of fourth and higher moments in reasonable measurement time.

The dual-path method [25] is a very promising candidate for becoming a standard tool in state-reconstruction of propagating quantum microwaves. With respect to competing methods [22], the advantage of the dual-path method clearly is that off-the-shelf components are used and detector noise moments are determined simultaniously, but on the other side it is demanding in theory and in terms of technical complexity. Thus, the successful state-reconstruction of non-classical states using the dual-path method in upcoming experiments at WMI will be a landmark for the future of this technique.

Appendix A
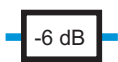
Components

Here all microwave component symbols will be shown and the devices will be explained very briefly. For further information please refer to textbooks such as Ref. [46]. For technical information on the devices used in this specific setup, the reader may follow the provided links to the manufacturer.

A.1 Passive microwave components

A.1.1 Attenuator

An attenuator consists of a resistor network, typically in a T-configuration, and reduces signal power by a given factor. The devices used in this work provide nearly constant attenuation between DC and 18 GHz.

Symbol	Technical information
-6 dB	`www.aeroflex-inmet.com` Series: 18AH

A.1.2 Filters

Filters limit the bandwidth of a signal. Two types of filters are used in the present thesis: low pass and band pass filters. In reality, filters will strongly attenuate the signal in the stop-pass band and let the signal pass virtually without loss in the pass-band. The devices used in this work are non-resistive, thus filtering is done by reflective losses.

Symbol	Technical information
SLP-21.4	`www.minicircuits.com` low pass
VBFZ-5500	`www.minicircuits.com` band pass
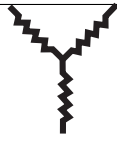
A.1.3 DC-Block

A DC-Block filters out any DC-components of the signal. Therefore it is an special
case of a low-pass filter.

Symbol	Technical information
8535	`www.aeroflex-inmet.com`

A.1.4 Power divider

This element is used to split up a microwave signal. In the experiment, a Willkinson
type Miteq PD2000/8000-30S (3 dB) and a resistive Mini-Circuits ZFRSC-183-S+
(6 dB) are used.

Symbol	Technical information
	`www.miteq.com`
	`www.minicircuits.com`

A.1.5 Termination

A terminator is a resistor that terminates the line.

Symbol	Technical information
50Ω	`www.hubersuhner.com`

A.1.6 Phase shifter

This elements allows to control the phase of the microwave signal. We use a
'trombone-type' phase shifter, which varies the phase be varying the length of the
transmission line. This type of phase shifter typically allows to shift between $30\,°$
and $90\,°$ per GHz. As our model shifts $90\,°$ per GHz and the typical measuring fre-
quency is at $5.6\,$GHz we can shift more than a full period, which is sufficient for our
purposes. In order to be able to control the phaseshifter with a PC and to obtain

the needed accuracy an existing phase shifter was modified for our experiment.

Symbol	Technical information
φ	www.nanotec.com
	www.atmmicrowave.com (P1607-28)

A.1.7   Adapters

Adapters are needed to switch between different connector types or to connect components which have connectors of same gender. Our setup mainly uses the SMA standard, only the connectors of the Acqiris digitizer card are of BNC type.

Symbol	Technical information
M-M	www.aeroflex.com
F-F	www.aeroflex.com
SMA 2BNC	www.aeroflex.com

A.1.8   Cables

Two types of microwave cables are used in the setup: Teledyne Reynolds True Blue 205 and Astrolab original MiniBend. In figures these are distinct by abbreviations 'TD' and 'MB' followed by the cable length, e.g. 'TD xm' oder 'MBx"', where the length x for TD is given in meters and for MB in inches.

Symbol	Technical information
TD 2m	
MB 7"	www.teledynereynolds.co.uk
	www.minibend.com

A.2   Active microwave components

A.2.1   Microwave source

Two different types of microwave sources are used, a Rohde & Schwarz SMF100A signal generator(SMF) and two Agilent Technologies E8267D (PSG).

Symbol	Technical information
SMF signal out	www.rohde-schwarz.com
PSG LO Out	www.agilent.com

A.2.2   Amplifiers

An amplifier increases the power of a signal by usage of an external power supply. In our setup, we use MiniCircuits ZX60-6013E and Miteq AFS-00100800-14-10P-5 for amplification in RF-frequencies of several gigahertz. For amplification in the IF band of several megahertz we use Miteq AU-1447-350.

Symbol	Technical information
	www.miteq.com www.minicircuits.com

A.2.3   Mixer

Mixers use a nonlinear device to achieve frequency conversion of an input signal [46]. In the mixers we use a radio frequency f_{RF} and a local oscillator f_{LO} are combined in such a way that the output signal is at the intermediate frequency $f_{IF} = f_{RF} - f_{LO}$. In addition signals at higher frequency are created in the mixing process, but these are filtered by an internal low pass filter. In the experiments, a Marki Microwave M1-0310LA is used.

Symbol	Technical information
IF LO —⊗— RF	www.MarkiMicrowave.com

A.3   Measuring devices

A.3.1   Acqiris card

As digitizer for all measurements in this thesis an Acqiris DC440 card is used. It has a resolution of 12bit, 400 MHz maximum sampling rate and internal sample memory

for 2×8000 samples. It can measuren in voltage ranges from ± 125mV to ± 5V.

Symbol	Technical information
Digitizer C1 C2 Trig Ref	www.acqiris.com www.agilent.com

A.3.2   FPGA card

A 4-port *Innovative Integration X5-RX* FPGA-card will be used for future realtime measurements. Information can be found at: www.innovative-dsp.com.

A.3.3   Spectrum Analyzer

A spectrum analyzer is used for the observation of signals in the frequency domain. We use two models from Rohde & Schwarz, the FSP7 and the FSV30. Further information can be found at www.rohde-schwarz.com and in [45].

A.3.4   Vector network analyzer

A vector network analyzer is used to measure the scattering parameters of circuit networks, mainly by means of S-parameters because reflection and transmission of electrical networks are convenient to measure at high frequencies. We use two models, Rohde & Schwarz ZVA8 and ZVA24. Further information can be found at www.rohde-schwarz.com and in [47].

A.4   Auxiliary devices

A.4.1   Data timing generator

The Tektronix DTG5334 Data Timing Generator is used to create the trigger signals which control pulsing and phase adjustment of the signals generated by the SMF microwave source.

Symbol	Technical information
DTG C1C2	www.tek.com

A.4.2   Voltage source

As voltage supply for step motors and amplifiers two EL302RT laboratory power supplies are used.

Symbol	Technical information
EL302RT	`www.aimtti.com`

A.4.3   Cooling device

Some of the amplifiers used in the setup need active cooling, which is achieved by usage of a circulation cooler with a temperature stability of $0.1\,\mathrm{K}$. To thermically couple the heat sink of the amplifier to the water cooling circuit, a standard GPU-cooler is used. The cooling device used is a Van der Heijden CoolCare. `www.van-der-heijden.de` gives technical information for the circulation cooler. At `www.alphacool.com` information on the used GPU-Cooler is provided.

A.4.4   CSI7002

This device consists of an array of relais and is controlled via commands sent over a serial interface from a PC.

A.4.5   Frequency standard

Stanford Research Systems FS725 Rubidium Frequency Standard technical information: `www.thinksrs.com`

Appendix B

Additional data

B.1 Calibration data of MPS2

As during characterization two phase-shifters have been in use, two data sets were measured, but only one device is actually used in the final setup. The figures in the main text only show the one actually used, which is called MPS1. Data for the other, called MPS2, can be found in Figs B.1(a)-B.1(c).

B.2 Phase modulation time for unused modes

Also the unused phase modulation modes of the SMF were analyzed. Results are shown in Figs. B.2 and B.3.
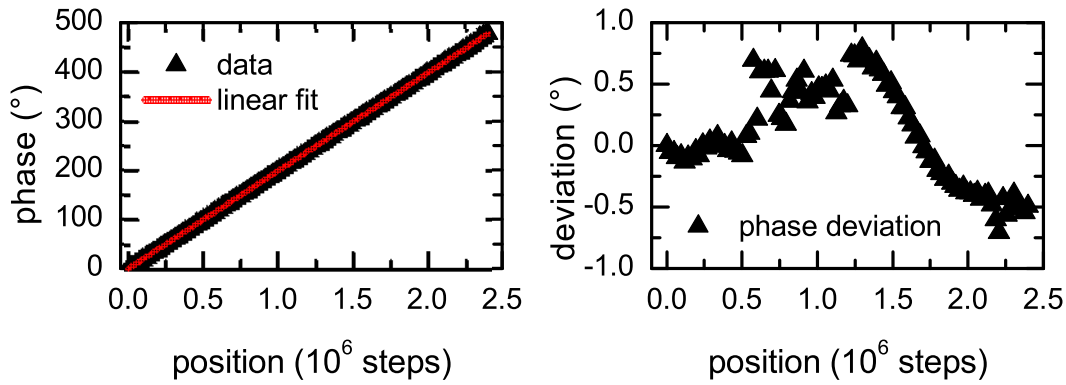
(a) Measured phase of motorized phase shifter depending on step motor position (left) and deviation from value calculated from fit(right).
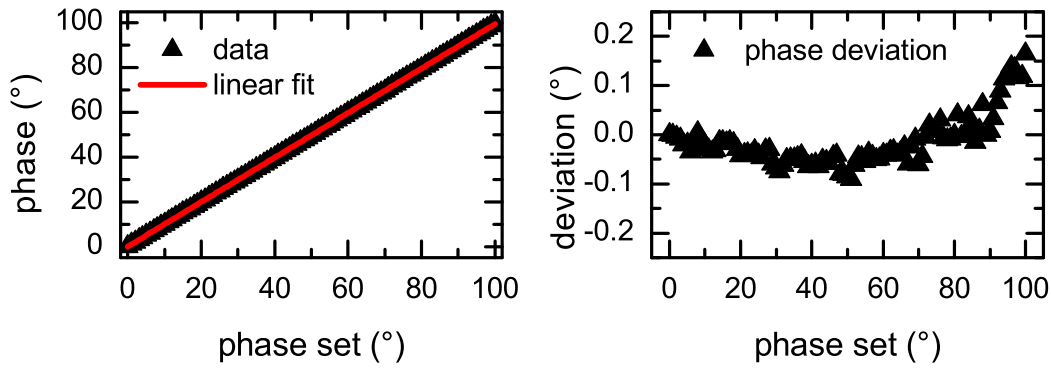
(b) Calibration data of the phase shifter. (left) Measured phase of motorized phase shifter depending on step motor position. (right) Deviation.
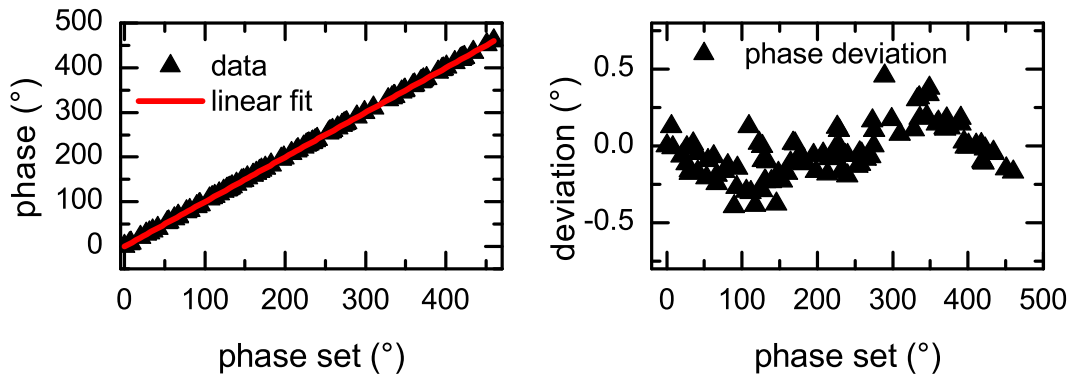
(c) Test with monotonously increasing set phase. (left) Measured phase of motorized phase shifter. (right) Deviation.

Figure B.1: Data for motorized phase shifter 2 (MPS2).
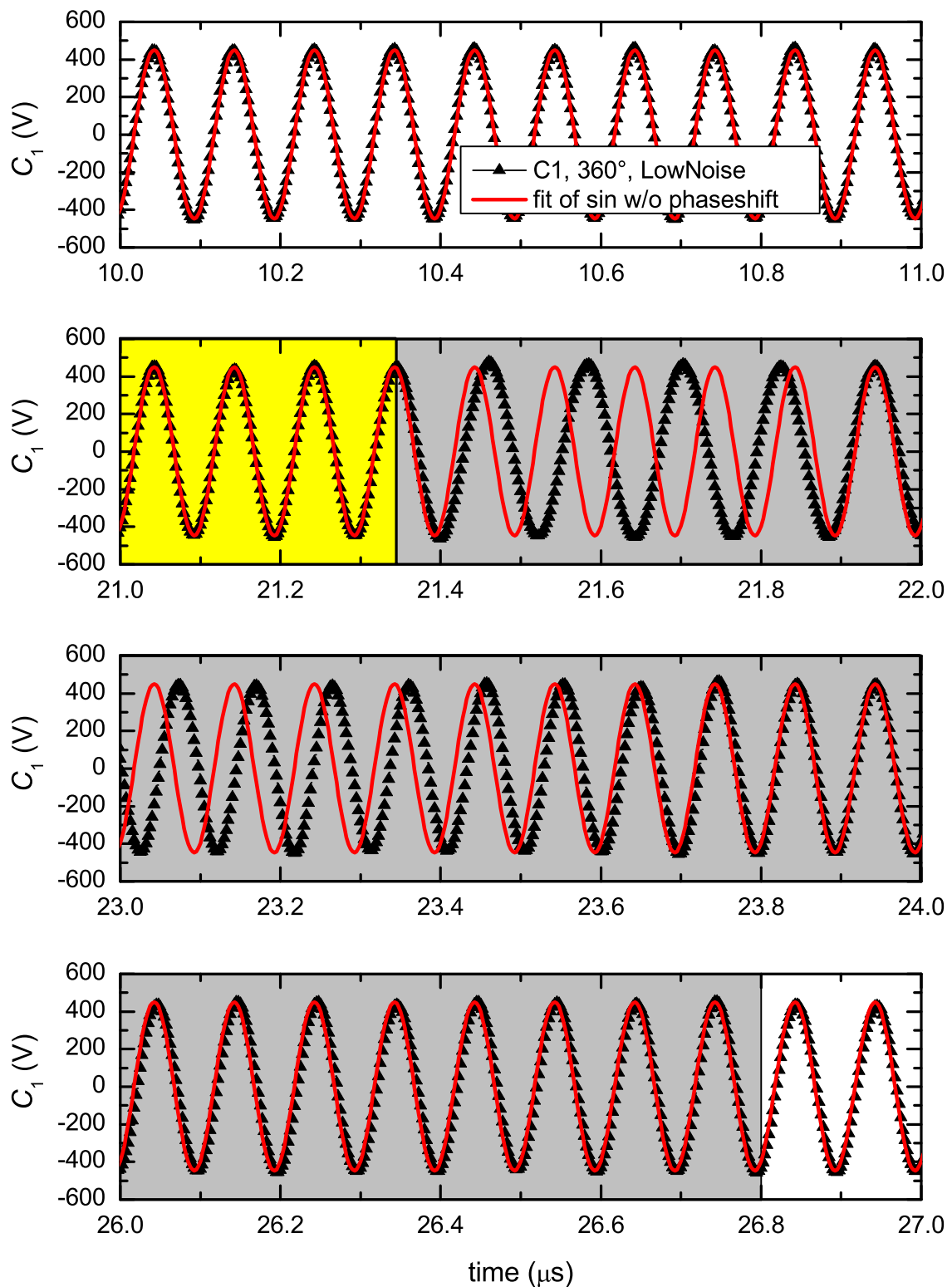
Figure B.2: Timetrace of SMF output for a phase shift of 360° in 'LowNoise' mode (black) compared to a fit of the signal before triggering the phase shift (red). The gray shaded area marks the region in time in which phase adjustment is in progress. The yellow area indicates the time in which the trigger already is fired, but the phase adjustment process has not started. Note: The yellow shaded area starts at 20µs.
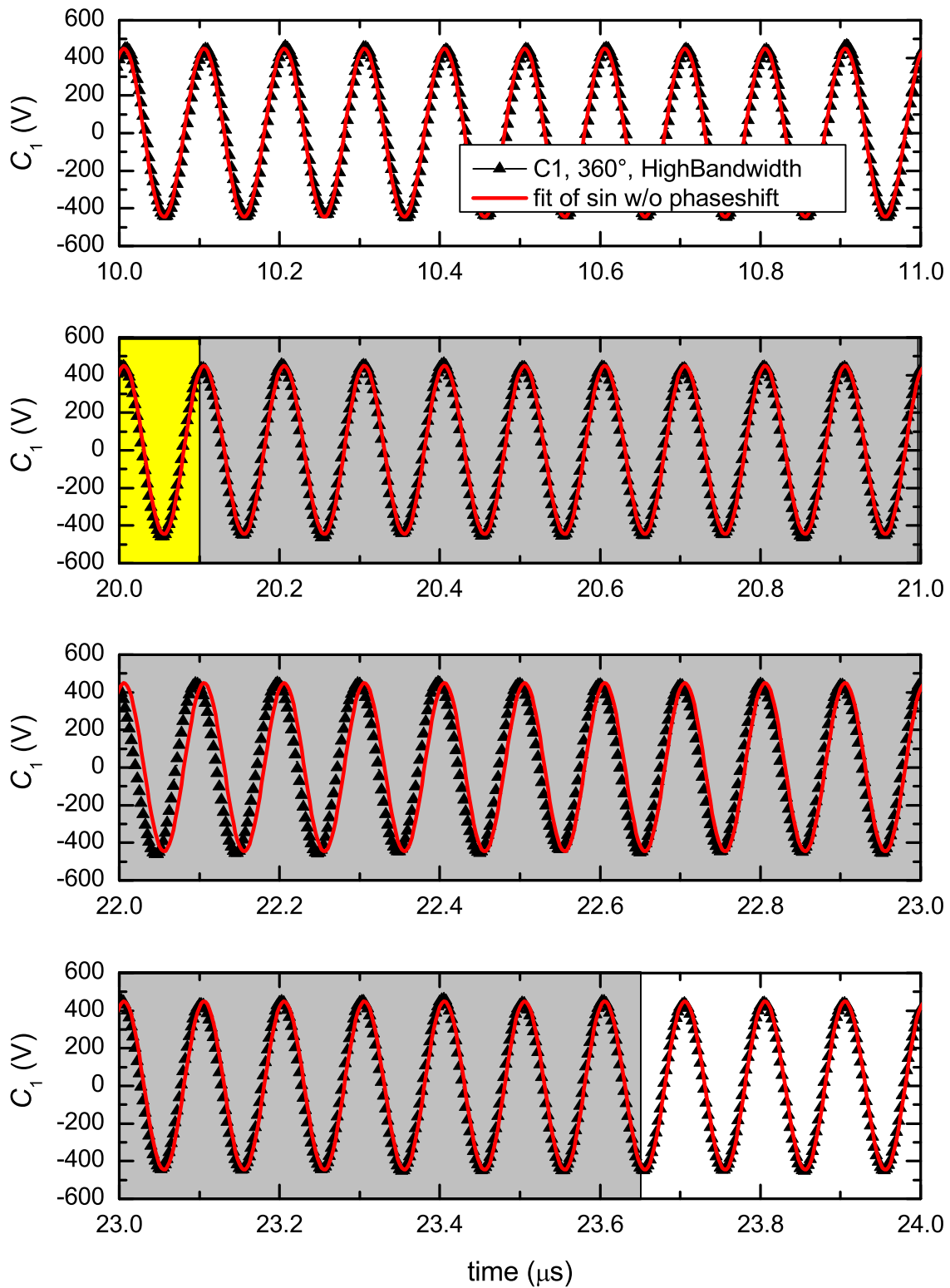
Figure B.3: Timetrace of SMF output for a phase shift of 360° in 'High-Bandwidth' mode (black) compared to a fit of the signal before triggering the phase shift (red). The gray shaded area marks the region in time in which phase adjustment is in progress. The yellow area indicates the time in which the trigger already is fired, but the phase adjustment process has not started. <u>Note</u>: The yellow shaded area starts at 20μs.

B.3   Moment variance of the probe signal

As stated in the main text, the moments of the probe signal $nCM(t)$ and their variances $\sigma_{nCM,\text{signal}}$ can be calculated analytically. This is done in the following for the first moment and the second and third central moment of the probe signal. The probe signal can be described as

$$S = \frac{3}{4}A \cdot \sin\left(\omega t - \varphi\right) + \frac{1}{4}A \cdot \sin\left(\omega t + \varphi\right), \qquad \varphi = 90° \quad , \tag{B.1}$$

and its variance is defined as

$$\sigma^2_{nCM,\text{signal}} := \frac{1}{2\pi} \int_0^{2\pi} (S(\omega t) - \overline{S(\omega t)})^n d(\omega t) \quad . \tag{B.2}$$

$$\tag{B.3}$$

B.3.1   First moment

$$FM = <S> \tag{B.4}$$

$$= -\frac{1}{2}A \cdot \cos\left(\omega t\right) \tag{B.5}$$

$$\sigma^2_{FM,\text{signal}} = \frac{1}{8}A^2 \tag{B.6}$$

B.3.2   Second central moment

$$SCM = <(S - <S>)^2> \tag{B.7}$$

$$= \frac{3}{4}\left(A \cdot \sin\left(\omega t\right) - \frac{1}{2}A \cdot \sin\left(\omega t\right)\right)^2 + \tag{B.8}$$

$$\frac{1}{4}\left(A \cdot (-1)\sin\left(\omega t\right) - \frac{1}{2}A \cdot \sin\left(\omega t\right)\right)^2$$

$$= \frac{3}{4}A^2 \cdot \sin^2\left(\omega t\right)$$

$$\sigma^2_{SCM,\text{signal}} = \frac{9}{128}A^4 \tag{B.9}$$

B.3.3   Third central moment

$$TCM = <(S - <S>)^3> \tag{B.10}$$

$$= -\frac{3}{4}A^3 \cdot \sin^3\left(\omega t\right) \tag{B.11}$$

$$\sigma^2_{TCM,\text{signal}} = \frac{45}{256}A^6 \tag{B.12}$$

B.4   Power sweeps
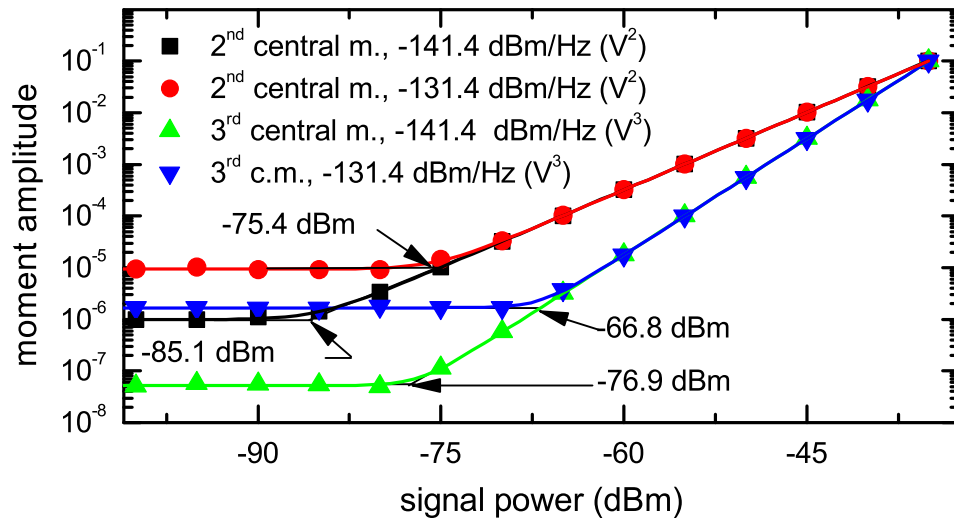
Figure B.4: Simulation of power sweep at constant noise powers to confirm Fig. 4.34.
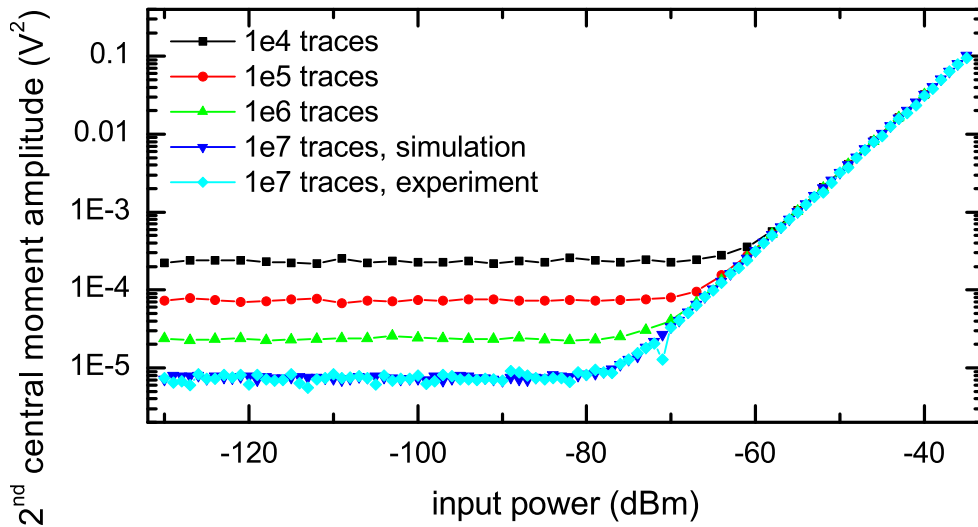

Figure B.5: Power sweep for different ensemble sizes to determine resolution limit of the second central moment.
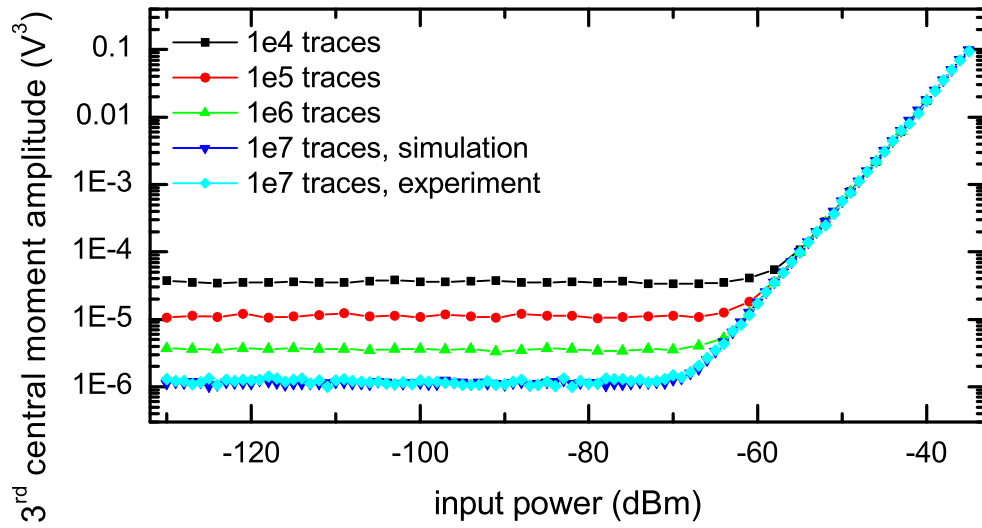
Figure B.6: Power sweep for different ensemble sizes to determine resolution limit of the third central moment.

Bibliography

[1] D. F. Walls & G. J. Milburn. *Quantum Optics* (Springer, Berlin, 2008).

[2] S. Haroche & J.-M. Raimond. *Exploring the Quantum - Atoms, Cavities and Photons* (Oxford University Press Inc., New York, 2006).

[3] H. Mabuchi & A. C. Doherty. Cavity Quantum Electrodynamics: Coherence in Context. *Science* **298**, 1372 (2002).

[4] N. Sangouard, J.-D. Bancal, N. Gisin, W. Rosenfeld, P. Sekatski, M. Weber & H. Weinfurter. Loophole-free Bell test with one atom and less than one photon on average. *Phys. Rev. A* **84**, 052122 (2011).

[5] A. Ourjoumtsev, A. Kubanek, M. Koch, C. Sames, P. W. H. Pinkse, G. Rempe & K. Murr. Observation of squeezed light from one atom excited with two photons. *Nature* **474**, 623 (2011).

[6] H. P. Specht, C. Nolleke, A. Reiserer, M. Uphoff, E. Figueroa, S. Ritter & G. Rempe. A single-atom quantum memory. *Nature* **473**, 190 (2011).

[7] J. M. Raimond, M. Brune & S. Haroche. Manipulating quantum entanglement with atoms and photons in a cavity. *Rev. Mod. Phys.* **73**, 565 (2001).

[8] A. Boca, R. Miller, K. M. Birnbaum, A. D. Boozer, J. McKeever & H. J. Kimble. Observation of the Vacuum Rabi Spectrum for One Trapped Atom. *Phys. Rev. Lett.* **93**, 233603 (2004).

[9] H. Walther, B. T. H. Varcoe, B.-G. Englert & T. Becker. Cavity quantum electrodynamics. *Rep. Prog. Phys.* **69**, 1325 (2006).

[10] A. Wallraff, D. I. Schuster, A. Blais, L. Frunzio, R.-S. Huang, J. Majer, S. Kumar, S. M. Girvin & R. J. Schoelkopf. Strong coupling of a single photon to a superconducting qubit using circuit quantum electrodynamics. *Nature* **431**, 162 (2004).

[11] A. Blais, R.-S. Huang, A. Wallraff, S. M. Girvin & R. J. Schoelkopf. Cavity quantum electrodynamics for superconducting electrical circuits: An architecture for quantum computation. *Phys. Rev. A* **69**, 062320 (2004).

[12] M. Mariantoni, H. Wang, T. Yamamoto, M. Neeley, R. C. Bialczak, Y. Chen, M. Lenander, E. Lucero, A. D. O'Connell, D. Sank, M. Weides, J. Wenner, Y. Yin, J. Zhao, A. N. Korotkov, A. N. Cleland & J. M. Martinis. Implementing the Quantum von Neumann Architecture with Superconducting Circuits. *Science* **334**, 61 (2011).

[13] J. M. Fink, L. Steffen, P. Studer, L. S. Bishop, M. Baur, R. Bianchetti, D. Bozyigit, C. Lang, S. Filipp, P. J. Leek & A. Wallraff. Quantum-To-Classical Transition in Cavity Quantum Electrodynamics. *Phys. Rev. Lett.* **105**, 163601 (2010).

[14] O. Astafiev, K. Inomata, A. O. Niskanen, T. Yamamoto, Y. A. Pashkin, Y. Nakamura & J. S. Tsai. Single artificial-atom lasing. *Nature* **449**, 588 (2007).

[15] F. Deppe, M. Mariantoni, E. P. Menzel, A. Marx, S. Saito, K. Kakuyanagi, H. Tanaka, T. Meno, K. Semba, H. Takayanagi, E. Solano & R. Gross. Two-photon probe of the Jaynes-Cummings model and controlled symmetry breaking in circuit QED. *Nature Phys.* **4**, 686 (2008).

[16] D. I. Schuster. *Circuit Quantum Electrodynamics.* Ph.D. thesis, Yale University (2007).

[17] T. Niemczyk, F. Deppe, H. Huebl, E. P. Menzel, F. Hocke, M. J. Schwarz, J. J. Garcia-Ripoll, D. Zueco, T. Hümmer, E. Solano, A. Marx & R. Gross. Circuit quantum electrodynamics in the ultrastrong-coupling regime. *Nature Phys.* **6**, 772 (2010).

[18] J. Casanova, G. Romero, I. Lizuain, J. J. García-Ripoll & E. Solano. Deep Strong Coupling Regime of the Jaynes-Cummings Model. *Phys. Rev. Lett.* **105**, 263603 (2010).

[19] M. Hofheinz, E. M. Weig, M. Ansmann, R. C. Bialczak, E. Lucero, M. Neeley, A. D. O'Connell, H. Wang, J. M. Martinis & A. N. Cleland. Generation of Fock states in a superconducting quantum circuit. *Nature* **454**, 310 (2008).

[20] M. A. Castellanos-Beltran, K. D. Irwin, G. C. Hilton, L. R. Vale & K. W. Lehnert. Amplification and squeezing of quantum noise with a tunable Josephson metamaterial. *Nature Phys.* **4**, 928 (2008).

[21] C. Eichler, D. Bozyigit, C. Lang, M. Baur, L. Steffen, J. M. Fink, S. Filipp & A. Wallraff. Observation of Two-Mode Squeezing in the Microwave Frequency Domain. *Phys. Rev. Lett.* **107**, 113601 (2011).

[22] F. Mallet, M. A. Castellanos-Beltran, H. S. Ku, S. Glancy, E. Knill, K. D. Irwin, G. C. Hilton, L. R. Vale & K. W. Lehnert. Quantum State Tomography of an Itinerant Squeezed Microwave Field. *Phys. Rev. Lett.* **106**, 220502 (2011).

[23] J. Clarke & F. K. Wilhelm. Superconducting quantum bits. *Nature* **453**, 1031 (2008).

[24] M. Hofheinz, H. Wang, M. Ansmann, R. C. Bialczak, E. Lucero, M. Neeley, A. D. O'Connell, D. Sank, J. Wenner, J. M. Martinis & A. N. Cleland. Synthesizing arbitrary quantum states in a superconducting resonator. *Nature* **459**, 546 (2009).

[25] E. P. Menzel, F. Deppe, M. Mariantoni, M. Á. Araque Caballero , A. Baust, T. Niemczyk, E. Hoffmann, A. Marx, E. Solano & R. Gross. Dual-Path State Reconstruction Scheme for Propagating Quantum Microwaves and Detector Noise Tomography. *Phys. Rev. Lett.* **105**, 100401 (2010).

[26] C. Eichler, D. Bozyigit, C. Lang, L. Steffen, J. Fink & A. Wallraff. Experimental State Tomography of Itinerant Single Microwave Photons. *Phys. Rev. Lett.* **106**, 220503 (2011).

[27] U. Leonhardt. *Measuring the Quantum State of Light* (Cambridge University Press, Cambridge, 1997).

[28] M. P. da Silva, D. Bozyigit, A. Wallraff & A. Blais. Schemes for the observation of photon correlation functions in circuit QED with linear detectors. *Phys. Rev. A* **82**, 043804 (2010).

[29] C. W. Gardiner & M. J. Collett. Input and output in damped systems: Quantum stochastic differential equations and the master equation. *Phys. Rev. A* **31**, 3761 (1985).

[30] B. Yurke. Squeezed-state generation using a Josephson parametric amplifier. *J. Opt. Soc. Am. B* **4**, 1551 (1987).

[31] S. L. Braunstein & P. van Loock. Quantum information with continuous variables. *Rev. Mod. Phys.* **77**, 513 (2005).

[32] B. Yurke. Wideband photon counting and homodyne detection. *Phys. Rev. A* **32**, 311 (1985).

[33] A. I. Lvovsky, H. Hansen, T. Aichele, O. Benson, J. Mlynek & S. Schiller. Quantum State Reconstruction of the Single-Photon Fock State. *Phys. Rev. Lett.* **87**, 050402 (2001).

[34] C. M. Caves. Quantum limits on noise in linear amplifiers. *Phys. Rev. D* **26**, 1817 (1982).

[35] E. P. Menzel. private communication.

[36] S. Sabah & R. Lorenz. Design and Calibration of IQ-mixers (1998). URL `http://accelconf.web.cern.ch/AccelConf/e98/PAPERS/WEP09A.PDF`.

[37] E. Wigner. On the Quantum Correction For Thermodynamic Equilibrium. *Phys. Rev.* **40**, 749 (1932).

[38] V. Buzek, G. Adam & G. Drobný. Quantum state reconstruction and detection of quantum coherences on different observation levels. *Phys. Rev. A* **54**, 804 (1996).

[39] A. J. Jerri. The Shannon sampling theorem - Its various extensions and applications: A tutorial review. *Proc. of the IEEE* **65**, 1565 (1977).

[40] J. B. Hagen. *Radio-Frequency Electronics - Circuits and Applications* (Cambridge University Press, Cambridge, 2009).

[41] wikipedia. http://en.wikipedia.org/wiki/Streaming_SIMD_Extensions (2011).

[42] P. Summer. *Simulation of the dual-path detector for propagating quantum microwaves.* Bachelor thesis, TU München (2011).

[43] wikipedia. http://en.wikipedia.org/wiki/FPGA (2011).

[44] P. Z. Peebles. *Probability, Random Variables, and Random Signal Principles* (McGrow Hill Inc., New York, 1987).

[45] C. Rauscher. *Grundlagen der Spektrumanalyse* (Rohde & Schwarz, München, 2008).

[46] D. M. Pozar. *Microwave Engineering* (John Wiley & Sons Inc., New York, 2005).

[47] M. Hiebel. *Grundlagen der vektoriellen Netzwerkanalyse* (Rohde & Schwarz GmbH&Co.KG, München, 2006).

Acknowledgments